SURFACE WAVE END - FIRE ANTENNA

Thesis for the Degree of Ph. D.
MICHIGAN STATE UNIVERSITY
OK KYUN KIM
1973

This is to certify that the

thesis entitled

SURFACE WAVE END-FIRE ANTENNA

presented by

Ok Kyun Kim

has been accepted towards fulfillment
of the requirements for

Ph. D. degree in EE

Major professor

Date July 20, 1973

O-7639

ABSTRACT

SURFACE WAVE END-FIRE ANTENNA

By

Ok Kyun Kim

This thesis presents the theoretical and experimental studies on a slow surface wave end-fire antenna. This antenna is composed of a flat corrugated conducting surface mounted on a finite conducting ground plane and a corrugated rectangular horn. The surface wave is launched by the corrugated rectangular horn and guided over the corrugated flat surface mounted on a finite ground plane. The radiation of this surface wave yields an end-fire beam of electromagnetic wave.

The advances in supersonic aircraft and space technology in recent years have created the needs for flush mounted scannable end-fire antennas. One of the effective schemes for designing this type of antenna is to employ a slow surface wave along a reactive impedance surface such as a corrugated surface. Existing studies on such a structure have been restricted to the ideal model of infinite extent. A few experimental studies on this antenna exist and they are mainly concerned with the wave propagating properties.

Rigorous theoretical analysis on the finite corrugated structure is not known to exist. In this study, approximate theoretical analyses on the launching device, the wave propagation and the radiation of the

surface wave have been made and an extensive experimental investigation was conducted to verify the approximate theory. Finally, a scheme of scanning the end-fire beam was studies experimentally.

SURFACE WAVE END-FIRE ANTENNA

By

Ok Kyun Kim

A THESIS

Submitted to
Michigan State University
in partial fulfillment of the requirements
for the degree of

DOCTOR OF PHILOSOPHY

Department of Electrical Engineering

1973

ACKNOWLEDGEMENTS

The author wishes to express his appreciation to his major professor, Dr. K. M. Chen, for his guidance and encouragement throughout the course of this work. He also wishes to thank the other members of his guidance committee, Dr. D. P. Nyquist, Dr. J. Asmussen, Dr. B. Ho and Dr. J. S. Frame for their time and help in this work.

Finally, the author wishes to thank his wife, Young Moo, and children for their support and encouragement during this work.

TABLE OF CONTENTS

LIST OF FIGURES

CHAPTER I

INTRODUCTION

Advances in super-sonic aircraft and space technology in recent years have created needs for flush mounted scannable end-fire antennas for communication between aircrafts or between aircraft and ground stations. One of the effective schemes for designing this antenna is to employ a slow surface wave along a periodic structure such as a corrugated surface. Existing studies on such a structure have been restricted to the ideal model of infinite extent. In this study, the electromagnetic radiation properties of a plane corrugated surface structure of finite dimension mounted on a finite ground plane are investigated theoretically and experimentally.

1.1 Review of Previous Work

The subject of surface waves on plane and hollow surface wave structures has received considerable attention of researchers, since the appearance of the classical papers on the wave propagation above the plane interface of a nonconducting and a conducting medium by Sommerfeld (1) and Zenneck (2). In early years, the investigations on surface waves were mostly confined to the mathematical treatments of their propagation characteristics (3-10).

The first theoretical study on wave propagation on corrugated structure was reported by Brillouin (11). In his work, the fields above

the corrugation were expanded in Fourier series based on the theorem of Floquet and the fields in the slots were assumed to be those of the TEM standing waves and TM waves. The approximate field amplitudes of the space harmonics were then derived by introducing a special analytic function.

Walkinshaw (12) and Shersby-Harvie (13) applied similar techniques to a circular corrugated waveguide to find the phase velocity of the surface wave by matching the average magnetic field in the presence of space harmonics. Rotman (14) also obtained slightly improved expressions for the phase velocities of the waves on the plane and circular corrugated structures and showed the agreement of his approximate expressions with experiment.

Hurd (15) was perhaps the first to derive the exact solution to a flat corrugated surface of infinite extent using a method based on the calculus of residues which was first applied to a similar problem by Whitehead (16) and Feodora Berz (17). The method yielded highly accurate results for the amplitudes and phase velocities of the fields propagating along a corrugated surface with vanishingly thin slot walls. The results showed that the amplitude of the fundamental harmonic becomes very large compared to those of higher order harmonics, when the slot depth is less than 0.15 wavelength and the number of corrugations per wavelength is greater than 20. The phase velocity was also found to be very close to the case of infinite number of corrugations.

Since then, the method of residue calculus has been applied to numerous problems dealing with corrugated structures and impedance strips in waveguides (18-24).

Although the subject of surface waves had received much attention, the practical applications of the surface wave had been limited to the linear accelerator and the traveling wave tube, until Goubau (25) suggested the possibility of using surface waves in a microwave transmission line. The subsequent experimental verification of the Goubau theory by Barlow and Karbowiak (8) heightened its applications to the microwave transmission line and the radiating structures. Furthermore, recent demands for high gain flush mounted antennas have caused a considerable amount of investigation on the raidation properties and excitation methods of the surface waves.

Most of the work on the excitation problems (26-33) were concerned with the ideal exciting source on the surface of infinite extent. Cullen (34) investigated theoretically the excitation efficiency of a line source over a plane corrugated structure. Subsequently, Fernando and Barlow (35) experimentally investigated the launching efficiency and confirmed Cullen's results. Nevertheless, the problem of surface wave excitation by a practical radiator over a finite corrugated structure has not been rigorously studied. The radiation mechanism of a surface wave has also caused some controversies because of its non-radiating property. It has been accepted, however, that the radiation of a surface wave is set up when the propagation of the wave is disturbed by a sudden discontinuity or it encounters the departure from the straight plane in the direction of propagation (34,36).

In calculating the radiation field from a surface wave structure, there are two distinctive methods. One is the aperture integration method through the Kirchhoff's vector integral or the Kirchhoff-Huygens' integral formula, and the other is the feed and terminal pattern method

based on the view point of the discontinuity. The aperture integration method is the simpler one, if the aperture fields can be accurately prescribed. This method has been extensively applied to the dielectric rod antennas (37-44). The feed and terminal pattern method (44-55) includes several analytical approaches such as the spectral representations of source field, the direct solution to the wave equation with the introduction of an auxiliary function and the integral equation approach with Wiener-Hopf technique. This feed and terminal pattern method is very rigorous in the analytical sense, but its application is limited to the ideal cases because of the mathematical complexity.

Concerning the application of slow surface wave structures to realize end-fire antennas, most analyses have been carried out on ideal models which are far from practical cases. Furthermore, there are very few experimental investigations to supplement the usefulness of the surface waves for the end-fire radiation. For this reason, one of the simple and practical surface wave antennas will be studied theoretically and experimentally to understand the nature of the surface wave propagation on a finite guiding surface. With this understanding, the development of a flush mounted scannable end-fire antenna can be faciliated.

1.2 Method of Investigation

The problem to be studied is the electromagnetic radiation characteristics of a flat corrugated surface on a finite ground plane functioning as an end-fire antenna. It is assumed that a corrugated surface of finite dimension supports the TM surface waves and these surface waves, in turn, result in an end-fire radiation.

In chapter 2, the fields in a corrugated rectangular waveguide are

derived as a preliminary study of the surface wave excitation over the open corrugated guiding surface, and a critical examination on the dispersion relation is made to find the optimum dimensions for the guide as a surface wave excitor.

In chapter 3, the possible fields on the corrugated plane surface are derived approximately from the fields in the corrugated rectangular waveguide obtained in chapter 2. Throughout the study, it is assumed that the hybrid waves in the guide transform completely into TM surface waves on the open guiding surface, i.e. a 100 percent launching efficiency. This assumption is tested in the theoretical calculation of the radiation patterns and in the experiment. In the field analysis, the possible modification of the field distribution over the finite open guiding surface is examined. With the surface wave fields determined on the corrugated surface, the induced current on the finite ground plane is calculated by means of a classical successive approximation method.

In chapter 4, the radiation patterns from the antenna structure are calculated by the aperture integration method using the previously determined aperture fields and the induced current on the ground plane.

Chapter 5 describes the design and the extensive experiment for the corrugated structure functioning as an end-fire antenna. In order to check the existence of the surface waves, the normal electric component is measured along the direction perpendicular to the guiding surface and the attenuation constant is then determined from the field distribution. The surface field distributions for the tangential electric and magnetic fields on the guiding surface and on the ground plane are

measured. From the measured field distributions, three dimensional field distribution patterns are constructed. In addition to the field probing, the phase velocity is carefully measured and compared with the theoretical values.

For the radiation characteristics, the E and H plane radiation patterns of a single radiator are measured over a wide range of frequencies and compared with the theoretical patterns. In order to produce a true end-fire beam which has the maximum beam intensity in the direction along the ground plane, a composite radiating system is designed by placing two corrugated surfaces on a wedge shape ground plane which simulates a portion of the sircraft wing. The radiation patterns of the composite radiator are measured for the cases with different wedge angles, and the scannability of the beam is investigated by adjusting the input power level of each radiator.

Finally, with the measurement of the input impedance of the antenna, the usefulness of the corrugated structures as a scannable flush mounted end-fire antenna is assessed, and the improved design parameters are also suggested.

CHAPTER II

SURFACE WAVE EXCITATION

For the application of the surface waves to realize a scannable end-fire radiation, it is necessary to excite a pure surface wave on the wave-guiding structure by effectively transforming the exciting feed modes to the dominant TM surface wave mode. Therefore, a highly efficient launching device is required.

Ehrlick and Newkirk (56) conducted a series of experiments and demonstrated that the feed radiation could be reduced to a reasonable degree, if the flat corrugated conducting surface was excited by a flared rectangular waveguide horn. He was able to observe that the far-field was the vector sum of feed and the guiding surface radiations by controlling the flared horn aperture dimension. However, any useful relation for the optimum dimension was not possible to establish, because of the unknown field and phase distributions on the horn aperture.

Based on the results obtained by a Stanford research group, Elliot (57) proposed a modified version of the above mentioned horn feed device. He reasoned qualitatively that if the excitation of slow surface waves is enhanced in the rectangular waveguide with one of its broad walls corrugated and extended to a desired length beyond the feed aperture to form a slow surface wave guiding plane, then the disturbance due to the transition from the hybrid mode in the corrugated rectangular waveguide to the TM slow surface wave mode on the extended single corru-

gated surface may not be so great that the feed radiation may be suppressed sufficiently.

In order to find the optimum design parameters for such corrugated rectangular waveguide excitor, a theoretical analysis of the fields and the dispersion relation in the rectangular waveguide with a corrugated wall as shown in Figure 2.1 will be carried out in this chapter.

2.1 General Properties of Periodically-Loaded Waveguides

The periodically loaded waveguide may be classified into two basic types according to their periodic boundary conditions along the axial direction: (1) The structures which are continuously periodical such as the waveguides filled with a dielectric material whose dielectric constant varies continuously in a periodic manner along the guide axis. (2) The structures which are discretely periodical such as the waveguide with identical obstacles placed at the regular intervals along the axis.

The iris-loaded rectangular waveguide or the corrugated waveguide shown in Figure 2.2 belongs to the second class. The surface y=0 forms the boundary surface of region I and II, and its surface impedance obeys a periodic function along the z direction with the period of D. The basic theorem describing the nature of wave propagation in the periodic structures is the theorem of Floquet. The theorem states that for a given mode of propagation at a given frequency, the fields at one cross-section differ from those one period away only by a complex constant.

In the mathematical notation, it may be written as

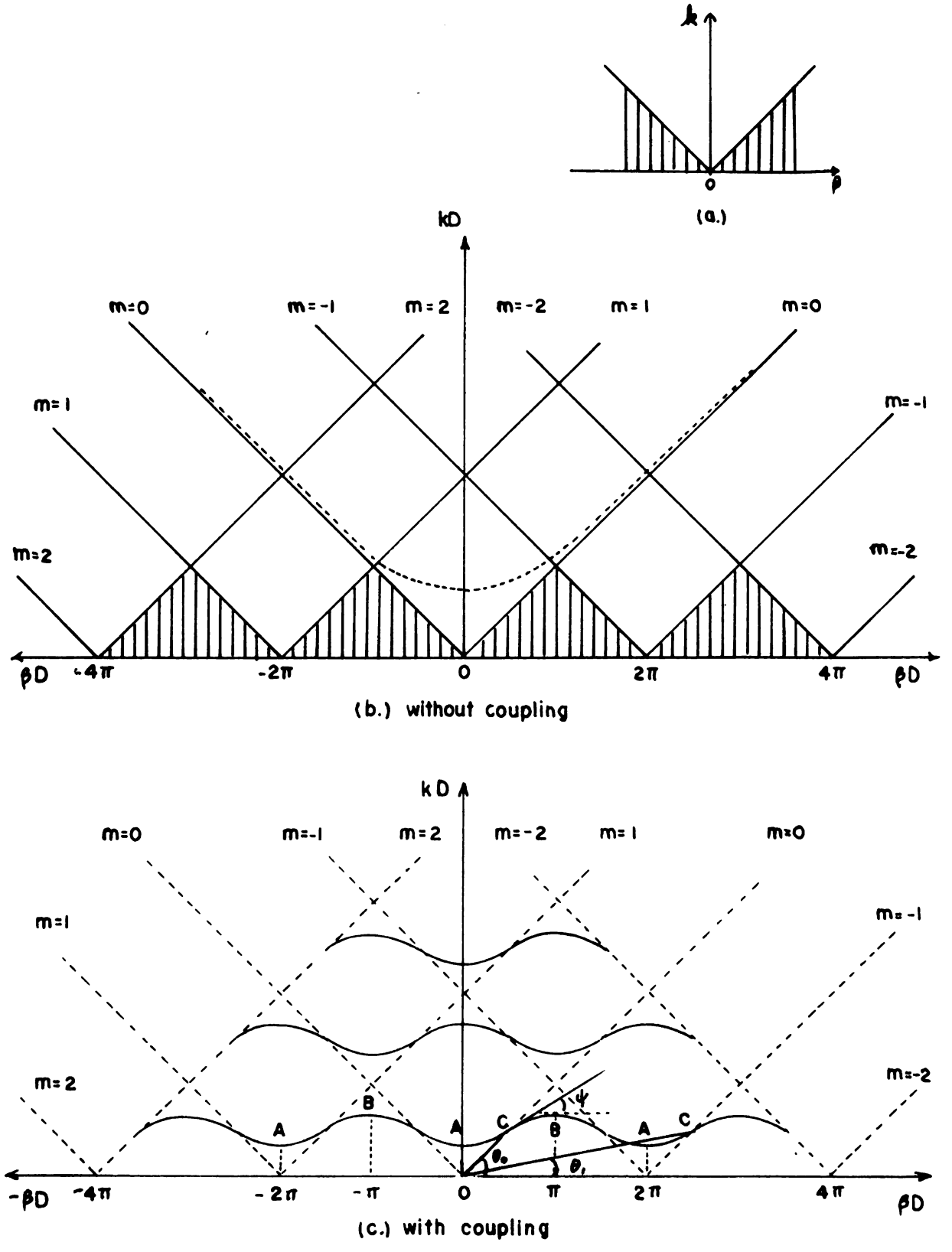

Figure 2.1 General Dispersion Curves for Periodic Structures

$$F(x,y,z,t) = f(x,y,z)\ e^{-\gamma z + j\omega t} \tag{2.1}$$

where $f(x,y,z)$ is an arbitrary function with a period D in z direction, and γ is a propagation constant. Since $f(x,y,z)$ is periodic in z, it may be expressed in terms of a Fourier series in a form,

$$f(x,y,z) = \sum_{p=-\infty}^{\infty} g_p(x,y)\ e^{-j\frac{2\Pi p}{D}z} \tag{2.2}$$

Substituting equation (2.2) into equation (2.1) yields

$$F(x,y,z,t) = \sum_{p=-\infty}^{\infty} g_p(x,y)\ e^{-\gamma_p z}\ e^{j\omega t} \tag{2.3}$$

where the p^{th} term in the series is called the p^{th} space harmonic and related by the usual orthogonality relation,

$$g_p(x,y) = \frac{1}{D}\int_{z_1}^{z_1+D} f(x,y,z)\ e^{j\frac{2\Pi p}{D}z}\,dz \tag{2.4}$$

The propagation constant γ_p is given by

$$\gamma_p = \gamma + j\frac{2\Pi p}{D} \qquad p = 0, \pm 1, \pm 2, \ldots \tag{2.5a}$$

and is in general complex with a form of

$$\gamma_p = \alpha_0 + j\beta_0 + j\frac{2\Pi p}{D} \tag{2.5b}$$

where the harmonic with p=0 is called the fundamental. If there is no loss in the structure, namely $\alpha_0 = 0$, the constant becomes a purely propagating mode,

$$\gamma_p = j\beta_p = j\left(\beta_0 + \frac{2\pi p}{D}\right) \qquad p = 0, \pm 1, \pm 2, \ldots \qquad (2.6)$$

where β_p is the phase constant of the p^{th} harmonic. However, if Floquet's mode is a purely attenuating one, i.e. $\beta_0 = 0$ then γ_p becomes complex. For this case, each harmonic propagates with the phase constant $\frac{2\pi p}{D}$ and the same attenuating rate. When both α_0 and β_0 are non-zero, each space harmonic has a complex propagation constant. This type of mode exists in the waveguide with losses and in some of the lossless guides such as helical wavequides (58) and a corrugated guide with reflection symmetry (23).

One of the most important properties in wave phenomena is the dispersion relation. It is the relation showing the dependence of β_0 on the k, which is the locus of points for $K_p = 0$, K_p being defined by the propagation constant in the transverse plane, $K_p = \sqrt{\gamma_p^2 + k^2}$. The plot is commonly referred to as the k - β diagram or the Brillouin diagram. The diagram shows the boundary separating the fast and the slow waves. For the lossless system with $\gamma_p = j\beta_p$, this boundary consists of two straight lines of slope ±1 intersecting at the origin as shown in Figure 2.1a. The shaded area where $\beta_0 < k$ is called the slow wave region and the unshaded area where $\beta_0 > k$ is called the fast wave region. In the fast wave region, K_p is purely real and the p^{th} harmonic propagates transversely, while in the slow wave region K_p is purely imaginary and the p^{th} harmonic is bound to the guiding surface. Thus, in the slow wave region, the amplitude of the field attenuates in the direction away from the surface.

When many space harmonics are considered and they are not interfering with each other, the dispersion curves may be drawn with the lines

of slope ±1 intersecting the βD axis at βD = 2pΠ as shown in Figure 2.1b, where the dotted line is a dispersion curve of the dominant mode in a uniform wave guide. Here the shaded area represents the region where all space harmonics are slow waves, and the outside of these areas are the regions of the fast wave for some space harmonics. In the real situation, the harmonics are coupled together and the dispersion curves exhibit the pass band and the stop band as shown in Figure 2.2c. This coupling phenomenon was first introduced by Pierce (59) in the study of a tape helix.

There are several important properties about the periodic structures: (1) With reference to Figure 2.1c, the dispersion curve is an even and periodic function of β_0. (2) The normalized phase velocity V_p/c is defined by $V_p/c = k/\beta_p = \tan \theta_m$. In the pass band, the fundamental harmonic has the highest phase velocity. The group velocity V_g/c is expressed by $V_g/c = dk/d\beta_p = \tan \psi$. For the propagation in + z direction, all of the space harmonics must have a positive group velocity and they are called the forward waves. On some parts of the curve, V_p and V_g are of opposite signs, and the corresponding waves are called the backward waves. In Figure 2.1c, the group velocities at the points A and B are zero, indicating that no energy propagates in the guide. The point at which $V_p = 0$ is said to belong to 0-mode and the point B at which $V_p = \Pi/D$ to Π-mode. (3) The complete field solution consists of an infinite number of space harmonics. But only a finite number of them are significant in the practical problem, since the magnitude of the harmonics drops off sharply with the increasing order and also with the decreasing period in the pass band. (4) All the harmonics are the Fourier components of one mode. Each harmonic does not satisfy

the boundary condition by itself but as a whole they do. Therefore, they cannot be called the modal fields which propagates or stores energy independently as in the uniform waveguide, while the space harmonics propagate as a whole. Thus, in the approximate field representation, care should be taken.

2.2 Expansion of Fields in the Corrugated Rectangular Waveguide

A conceptually simple and efficient device for the surface wave excitation may be a corrugated rectangular waveguide in which the waves are slow and similar to the waves on the open guiding surface. If one of the walls of such a waveguide is extended to form an open slow surface wave guiding plane, the field disturbance at the aperture may be reduced provided the waves in the closed waveguide can be transformed to another type of slow surface wave mode on the open guiding surface with less radiation at the aperture by controlling the aperture geometry.

The waveguide to be studied here is a rectangular waveguide with one of its H-plane walls being transversely corrugated. The waveguide is assumed to be perfectly matched in both axial directions and the number of corrugations per wavelength is large enough that the teeth of the corrugations may be considered to be sufficiently thin. The waveguide is assumed to be excited by a TE_{10} mode in a uniform rectangular waveguide connected in tandem. Figure 2.2 shows the geometry of the corrugated rectangular waveguide.

In the corrugated waveguide, each corrugation acts as a discontinuity on the incident wave and excites the higher order modes. Since these higher order modes may not be greatly attenuated at the positions of the next adjacent corrugation, the characteristics of the propagation constant over the entire corrugated surface in the guide may greatly

differ from those of the uniform waveguide. The wave in such corrugated waveguide is characterized as a hybrid wave, i.e. the combination of the TE and TM modes. In such waveguide, two types of propagation can occur; one is the fast hybrid wave which is characterized by a low intensity at the corrugated wall and the other is the slow hybrid wave with a strong axial electric field at the corrugated wall.

In the waveguides with the anisotropic boundary walls such as the corrugated waveguide or the dielectric filled waveguide, a solution of Maxwell's equations cannot be obtained by the usual decomposition of the fields into the transverse electric (TE) and transverse magnetic (TM) modes as in the conventional waveguides with the metallic walls. The TE and TM modes are coupled to form a hybrid mode designated by the EH modes. The hybrid modes do not possess the familiar orthogonality as in the uniform waveguide but a special orthogonality relation (60). Generally, the transverse electric and magnetic fields are not orthogonal in such guide. The angle between them and the ratio of their magnitudes are a function of frequency as well as the position in the transverse plane. However, in the corrugated rectangular waveguide, the transverse electric and magnetic field components are perpendicular regardless of the frequency and the position of the cross sectional plane.

The exact solution for the fields in the corrugated rectangular waveguide has not been known to exist because of the complex boundary conditions and an infinite number of space harmonics. Thus, the field analysis will be attempted on the idealized model of infinitely thin corrugation as shown in Figure 2.2b, and the results will be modified to be applicable to the practical finite geometry.

In a homogeneous, isotropic and lossless medium with permitivity

ε and permeability μ, the generalized Maxwell's equations for harmonic time variation with an assumed time dependence of the form $e^{j\omega t}$ may be expressed as

$$\begin{aligned} \nabla \times \vec{E} &= -j\omega\mu\vec{H} - \vec{K} \\ \nabla \times \vec{H} &= j\omega\varepsilon\vec{E} + \vec{J} \\ \nabla \cdot \vec{E} &= \frac{\rho}{\varepsilon} \\ \nabla \cdot \vec{H} &= \frac{\rho_m}{\mu} \end{aligned} \tag{2.7}$$

where $\vec{E}$, $\vec{H}$ = electric and magnetic field vectors

$\vec{J}$, $\vec{K}$ = electric current and fictitious magnetic current

ρ, ρ_m = electric charge and fictitious magnetic charge

ω = angular frequency

The classical method for solving (2.7) is the Hertz potential approach by introducing electric vector function $\vec{\Pi}_e$ and magnetic vector function $\vec{\Pi}_h$ satisfying the inhomogeneous partial differential equations

$$\begin{aligned} \nabla^2 \vec{\Pi}_e + k^2 \vec{\Pi}_e &= -\mu\vec{J} \\ \nabla^2 \vec{\Pi}_h + k^2 \vec{\Pi}_h &= -\varepsilon\vec{K} \end{aligned} \tag{2.8}$$

where $k^2 = \omega^2\mu\varepsilon$. The general solution of equation (2.8) can be constructed as the sum of a complementary solution and a particular solution. In general, the sources $\vec{J}$ and $\vec{K}$ are independent. Then, the E and H fields may be expressed as

$$\begin{aligned} \vec{E} &= -j\omega\mu \nabla \times \vec{\Pi}_h + [\nabla \times \nabla \times \vec{\Pi}_e - \mu\vec{J}] \\ \vec{H} &= j\omega\varepsilon \nabla \times \vec{\Pi}_e + [\nabla \times \nabla \times \vec{\Pi}_h - \varepsilon\vec{K}] \end{aligned} \tag{2.9}$$

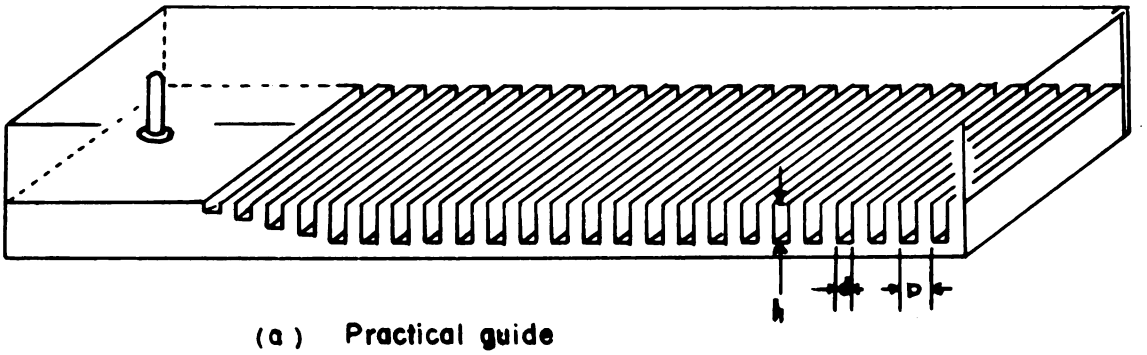

(a) Practical guide

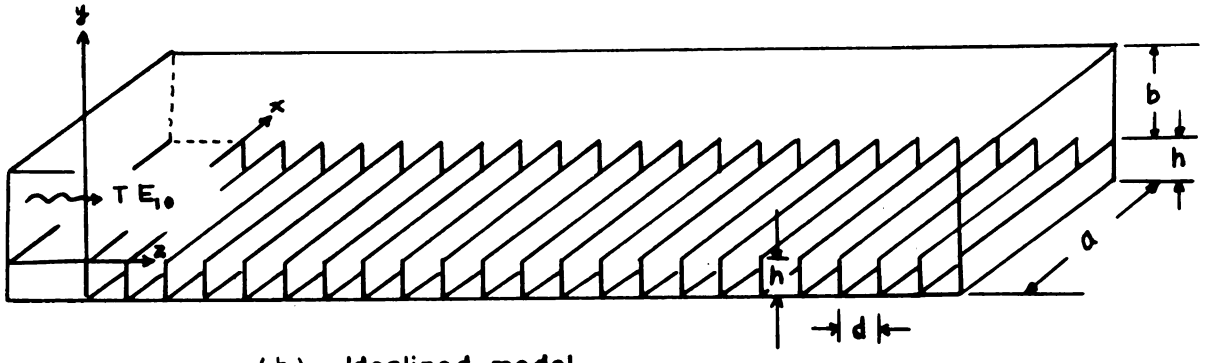

(b) Idealized model

Figure 2.2 Corrugated Rectangular Waveguide

Fields Above Corrugation for y > 0:

In representing the fields above the corrugation, it is natural to follow Floquet's theorem for its periodic nature. This permits one to express the fields as the summation of an infinite number of space harmonics with the period of D. The fields for y > 0 may be derived from a magnetic type Hertz potential in the form of hybrid mode by means of the following relations given in equation (2.9) with $\bar{J}$, $\bar{K}$, $\vec{\Pi}_e = 0$.

$$\vec{E} = -j\omega\mu \nabla \times \vec{\Pi}_h$$
$$\vec{H} = \nabla \times \nabla \times \vec{\Pi}_h \tag{2.10}$$

Here, $\vec{\Pi}_h$ is the solution of a homogeneous partial differential equation,

$$\nabla^2 \vec{\Pi}_h + k^2 \vec{\Pi}_h = 0 \tag{2.11}$$

Since the incident wave is assumed to be a TE_{10} mode, one may assume that $E_x = 0$ on the corrugated surface y = 0. For this type of field, the correct magnetic Hertz vector function $\vec{\Pi}_h$ may be written in the form of

$$\vec{\Pi}_h = \hat{x}\, \phi(x,y)\, e^{\pm j\beta_p z} \tag{2.12}$$

The transverse potential function $\phi(x,y)$ in equation (2.12) satisfies the two-dimensional scalar Helmholtz equation,

$$\nabla_t^2 \phi(x,y) + k_c^2 \phi(x,y) = 0 \tag{2.13}$$

where $k_c^2 = k^2 + \gamma^2$ with $\gamma = j\beta_p$ for lossless case, and ∇_t^2 is the transverse part of ∇ operator. By applying the proper boundary conditions ($\frac{\partial \phi}{\partial y} = 0$ at y = b, $\phi = 0$ at x = a/2), the solution for the $\phi(x,y)$ in

equation (2.13) is given as follows:

For symmetric mode about x axis,

$$\vec{\Pi}_h = \hat{x} \sum_{p=-\infty}^{\infty} \sum_{m} A_p \cos\left(\frac{m\Pi x}{a}\right) \cosh \mu(y-b)\, e^{-j\beta_p z}$$

$$m = 1,3,5, \ldots \tag{2.14}$$

$$\vec{\Pi}_h = \hat{x} \sum_{p=-\infty}^{\infty} \sum_{m} B_p \sin\left(\frac{m\Pi x}{a}\right) \cosh \mu(y-b)\, e^{-j\beta_p z}$$

$$m = 0,2,4,6, \ldots$$

For asymmetric mode about x axis,

$$\vec{\Pi}_h = \hat{x} \sum_{p=-\infty}^{\infty} \sum_{m} C_p \cos\left(\frac{m\Pi x}{a}\right) \sinh \mu(y-b)\, e^{-j\beta_p z}$$

$$m = 1,3,5, \ldots \tag{2.15}$$

$$\vec{\Pi}_h = \hat{x} \sum_{p=-\infty}^{\infty} \sum_{m} D_p \sin\left(\frac{m\Pi x}{a}\right) \sinh \mu(y-b)\, e^{-j\beta_p z}$$

$$m = 0,2,4,6, \ldots$$

The eigenvalue μ in equations (2.14) and (2.15) may be real or imaginary. If μ is imaginary, the wave is associated with a slow wave and for real μ, the wave is identified as a fast wave. Since the slow wave solution is desired for the problem, the value of μ will be taken as imaginary and it is related to the transverse wave number γ_{yp} in the direction away from the corrugated surface as

$$\mu = j\alpha_p$$

$$\alpha_p = \sqrt{\beta_p^2 + \left(\frac{m\Pi}{a}\right)^2 - k^2} \tag{2.16}$$

where α_p is termed as the attenuation constant of the hybrid wave in the transverse plane. Thus, for the slow wave hybrid mode solution, the correct Hertz vector function may be expressed as follows:

For symmetric mode about x axis,

$$\vec{\Pi}_h = \hat{x} \sum_{p=-\infty}^{\infty} \sum_{m} A_p \cos\left(\frac{m\pi x}{a}\right) \cosh \alpha_p (y-b)\, e^{-j\beta_p z}$$

$$m = 1,3,5, \ldots \qquad (2.17)$$

$$\vec{\Pi}_h = \hat{x} \sum_{p=-\infty}^{\infty} \sum_{m} B_p \sin\left(\frac{m\pi x}{a}\right) \cosh \alpha_p (y-b)\, e^{-j\beta_p z}$$

$$m = 0,2,4,6, \ldots$$

For asymmetric mode about x axis,

$$\vec{\Pi}_h = \hat{x} \sum_{p=-\infty}^{\infty} \sum_{m} C_p \sin\left(\frac{m\pi x}{a}\right) \sinh \alpha_p (y-b)\, e^{-j\beta_p z}$$

$$m = 1,3,5, \ldots \qquad (2.18)$$

$$\vec{\Pi}_h = \hat{x} \sum_{p=-\infty}^{\infty} \sum_{m} D_p \sin\left(\frac{m\pi x}{a}\right) \sinh \alpha_p (y-b)\, e^{-j\beta_p z}$$

$$m = 0,2,4,6, \ldots$$

Then, the fields in the region above the corrugated wall, $0 < y < b$ $-a/2 < x < +a/2$, in the guide can be completely expressed by the Hertz potential in equation (2.17) or (2.18) with relation given in equation (2.10). In the expressions for the magnetic Hertz potential, the symmetric mode assumes the TE mode excitation and the asymmetric mode assumes the TM mode excitation in the guide. Since the guide is assumed to be

excited by TE_{10} mode, the fields in the region above the corrugation are given only by the symmetric Hertz potential as follows: The fields will be expressed separately in odd m mode and even m mode for the + z direction only.

For odd m modes: m = 1,3,5, ...

$$
\begin{aligned}
E_y &= j \sum_{p=-\infty}^{\infty} \sum_{m} A_p \beta_p \cos\left(\frac{m\pi x}{a}\right) \cosh \alpha_p (y-b)\, e^{-j\beta_p z} \\
E_z &= \sum_{p=-\infty}^{\infty} \sum_{m} A_p \alpha_p \cos\left(\frac{m\pi x}{a}\right) \sinh \alpha_p (y-b)\, e^{-j\beta_p z} \\
H_x &= \frac{1}{j\omega\mu} \sum_{p=-\infty}^{\infty} \sum_{m} A_p K_m^2 \cos\left(\frac{m\pi x}{a}\right) \cosh \alpha_p (y-b)\, e^{-j\beta_p z} \\
H_y &= -\frac{1}{j\omega\mu} \sum_{p=-\infty}^{\infty} \sum_{m} A_p \alpha_p \frac{m\pi}{a} \sin\left(\frac{m\pi x}{a}\right) \sinh \alpha_p (y-b)\, e^{-j\beta_p z} \\
H_z &= \frac{1}{\omega\mu} \sum_{p=-\infty}^{\infty} \sum_{m} A_p \beta_p \frac{m\pi}{a} \sin \frac{m\pi x}{a} \cosh \alpha_p (y-b)\, e^{-j\beta_p z}
\end{aligned}
\tag{2.19}
$$

For even m modes: m = 0,2,4,6, ...

$$
\begin{aligned}
E_y &= j \sum_{p=-\infty}^{\infty} \sum_{m} B_p \beta_p \sin\left(\frac{m\pi x}{a}\right) \cosh \alpha_p (y-b)\, e^{-j\beta_p z} \\
E_z &= \sum_{p=-\infty}^{\infty} \sum_{m} B_p \alpha_p \sin\left(\frac{m\pi x}{a}\right) \sinh \alpha_p (y-b)\, e^{-j\beta_p z} \\
H_x &= \sum_{p=-\infty}^{\infty} \sum_{m} B_p K_m^2 \sin\left(\frac{m\pi x}{a}\right) \cosh \alpha_p (y-b)\, e^{-j\beta_p z}
\end{aligned}
$$

$$H_y = \frac{1}{j\omega\mu} \sum_{p=-\infty}^{\infty} \sum_m B_p \alpha_p \frac{m\Pi}{a} \cos(\frac{m\Pi x}{a}) \sinh \alpha_p (y-b) \, e^{-j\beta_p z}$$

$$H_z = \frac{-1}{j\omega\mu} \sum_{p=-\infty}^{\infty} \sum_m B_p \beta_p \frac{m\Pi}{a} \cos(\frac{m\Pi x}{a}) \cosh \alpha_p (y-b) \, e^{-j\beta_p z} \qquad (2.20)$$

where

$$K_m^2 = k^2 - (\frac{m\Pi}{a})^2$$

$$\alpha_p^2 = \beta_p^2 - K_m^2 \qquad (2.21)$$

$$\beta_p = \beta_0 + \frac{2\Pi p}{D} \qquad p = 0, \pm 1, \pm 2, \ldots$$

In equations (2.19) and (2.20), the coefficients A_p and B_p are still unknown. These must be determined by correctly matching the fields above the corrugated wall and the fields in the slot along the interface $y = 0$ to complete the field representation in the corrugated waveguide.

It may be easily shown that the form of the field representation in equations (2.19) and (2.20) is correct one by setting $\alpha_p = 0$, $p = 0$ and $m = 1$,

$$E_y = -\omega\mu A_0 \beta_0 \cos(\frac{\Pi x}{a}) \, e^{-j\beta_0 z}$$

$$H_x = A_0 \beta_0^2 \cos(\frac{\Pi x}{a}) \, e^{-j\beta_0 z} \qquad (2.22)$$

$$H_z = j A_0 \beta_0 \frac{\Pi}{a} \sin(\frac{\Pi x}{a}) \, e^{-j\beta_0 z}$$

$$H_y = E_z = 0$$

These expressions are the fields of the TE_{10} mode in the uniform rectangular waveguide. The fields are actually the excitation field (incident fields) for the corrugated waveguide. It should be noted that the

slow hybrid waves are not excited at the point of launch for the frequency below the dominant cutoff of the uniform guide. This property will be examined in the k-β diagram for the corrugated guide in the later section.

Fields in the Slots for $y < 0$:

The corrugated walls of the rectangular waveguide may be considered as being made of series of the short circuited rectangular waveguide for an approximate analysis. Hence, each cell is considered as a short circuited rectangular waveguide of width a, height d and length h. In such a short circuited waveguide, the dominant fields are the standing waves of all modes that are not below the cutoff. Therefore, it is appropriate to write all the possible modes in the infinitely long waveguide and to generate the standing waves by the possible propagating modes in such a way that the continuity of the fields along the slot mouth is satisfied. In view of the fields above the corrugation, the fields in the slot will be expressed by the combination of TE and TM modes. Such fields can be directly written by the combination of the TE and TM modes and setting $E_x = 0$, since those modes are separable. Also, they may be directly derived from the magnetic type Hertz potential in the form of $\vec{\Pi}_h = \hat{x}\,\phi(x,z)\,e^{\gamma_n y}$. The proper expression for the Hertz potential may be obtained by solving equation (2.13) with the boundary conditions at the walls ($\frac{\partial \phi}{\partial z} = 0$ at $z = 0, d$, $\phi = 0$ at $x = \pm a/2$). The proper Hertz potential is expressed by

$$\vec{\Pi}_n = \hat{x} \sum_{n=0}^{\infty} \sum_{m} B_{mn} \cos\left(\frac{m\pi x}{a}\right) \cos\left(\frac{n\pi z}{d}\right) e^{\gamma_n y}$$

$$m = 1,3,5,7, \ldots \qquad (2.23)$$

$$\vec{\Pi}_n = \hat{x} \sum_{n=0}^{\infty} \sum_{m} A_{mn} \sin\left(\frac{m\Pi x}{a}\right) \cos\left(\frac{n\Pi z}{d}\right) e^{\gamma_n y}$$

$$m = 0,2,4,6, \ldots$$

The fields in the infinitely deep slot may then be expressed by the Hertz potential given in equation (2.23) and the relation given in equation (2.10) as follows:

For odd m mode: $m = 1,3,5, \ldots$

$$E_y = \sum_{n=0}^{\infty} \sum_{m} B_{mn} \left(\frac{n\Pi}{a}\right) \cos\left(\frac{m\Pi x}{a}\right) \sin\left(\frac{n\Pi z}{d}\right) e^{\gamma_n y}$$

$$E_z = \sum_{n=0}^{\infty} \sum_{m} B_{mn} \gamma_n \cos\left(\frac{m\Pi x}{a}\right) \cos\left(\frac{n\Pi z}{d}\right) e^{\gamma_n y}$$

$$H_x = \frac{1}{j\omega\mu} \sum_{n=0}^{\infty} \sum_{m} B_{mn} K_n^2 \cos\left(\frac{m\Pi x}{a}\right) \cos\left(\frac{n\Pi z}{d}\right) e^{\gamma_n y} \qquad (2.24)$$

$$H_y = \frac{-1}{j\omega\mu} \sum_{n=0}^{\infty} \sum_{m} B_{mn} \gamma_n \left(\frac{m\Pi}{a}\right) \sin\left(\frac{m\Pi x}{a}\right) \cos\left(\frac{n\Pi z}{d}\right) e^{\gamma_n y}$$

$$H_z = \frac{1}{j\omega\mu} \sum_{n=0}^{\infty} \sum_{m} B_{mn} \left(\frac{m\Pi}{a}\right)\left(\frac{n\Pi}{d}\right) \sin\left(\frac{m\Pi x}{a}\right) \sin\left(\frac{n\Pi z}{d}\right) e^{\gamma_n y}$$

For even m mode: $m = 0,2,4, \ldots$

$$E_y = \sum_{n=0}^{\infty} \sum_{m} A_{mn} \left(\frac{n\Pi}{d}\right) \sin\left(\frac{m\Pi x}{a}\right) \sin\left(\frac{n\Pi z}{d}\right) e^{\gamma_n y}$$

$$E_z = \sum_{n=0}^{\infty} \sum_{m} A_{mn} \gamma_n \sin\left(\frac{m\Pi x}{a}\right) \cos\left(\frac{n\Pi z}{d}\right) e^{\gamma_n y}$$

$$H_x = \frac{1}{j\omega\mu} \sum_{n=0}^{\infty} \sum_{m} A_{mn} K_m^2 \sin\left(\frac{m\Pi x}{a}\right) \cos\left(\frac{n\Pi z}{d}\right) e^{\gamma_n y} \qquad (2.25)$$

$$H_y = \frac{1}{j\omega\mu} \sum_{n=0}^{\infty} \sum_{m} A_{mn} \gamma_n \left(\frac{m\pi}{a}\right) \cos\left(\frac{m\pi x}{a}\right) \cos\left(\frac{n\pi z}{d}\right) e^{\gamma_n y}$$

$$H_z = \frac{-1}{j\omega\mu} \sum_{n=0}^{\infty} \sum_{n} A_{mn} \left(\frac{m\pi}{a}\right)\left(\frac{n\pi}{d}\right) \cos\left(\frac{m\pi x}{a}\right) \sin\left(\frac{n\pi z}{d}\right) e^{\gamma_n y}$$

where

$$K_m^2 = k^2 - \left(\frac{m\pi}{a}\right)^2$$

$$\gamma_n = \sqrt{\left(\frac{m\pi}{a}\right)^2 + \left(\frac{n\pi}{d}\right)^2 - k^2} \qquad (2.26)$$

The propagation constant γ_n becomes real for the higher order modes since the slot gap (d) is much smaller than the waveguide width (a) and the wavelength (λ_0). Consequently, the higher order modes of the TE waves ($n > 0$) and the all modes of TM waves in the slot guide are the attenuating waves in the direction of propagation (y direction). Therefore, these higher order modes may be substantially attenuated as they travel down in a short distance toward the bottom of the shorted wall and give little reflected waves from the bottom of the slot. Hence, only the dominant mode TE_{10} will give the major reflected wave resulting in a standing wave in the slot. Depending on the guide dimension and the excitation method, the TE_{m0} modes will give some contributions to the standing waves in the slot.

When the excitation of the slow wave is of the main interest, the depth of the slot is generally made very shallow, $h \ll \lambda/4$, to keep the wall surface slightly inductive. For such structure, the attenuating higher order modes may give some contribution to the standing waves in the slot. Therefore, the slot fields may be expressed by the superposition of the standing waves of all modes, and for the approximate analysis

the higher order modes may be neglected. Finally the fields in the slot are given as follows:

Fields in a single slot:

For odd m mode: m = 1,3,5, ...

$$E_y = \sum_{n=0}^{\infty} \sum_{m} B_{mn} \left(\frac{n\pi}{d}\right) \cosh \gamma_n (y+h) \cos\left(\frac{m\pi x}{a}\right) \sin\left(\frac{n\pi z}{d}\right)$$

$$E_z = \sum_{n=0}^{\infty} \sum_{m} B_{mn} \gamma_n \sinh \gamma_n (y+h) \cos\left(\frac{m\pi x}{a}\right) \cos\left(\frac{n\pi z}{d}\right)$$

(2.27)

$$H_x = \frac{1}{j\omega\mu} \sum_{n=0}^{\infty} \sum_{m} B_{mn} K_m^2 \cosh \gamma_n (y+h) \cos\left(\frac{m\pi x}{a}\right) \cos\left(\frac{n\pi z}{d}\right)$$

$$H_y = \frac{-1}{j\omega\mu} \sum_{n=0}^{\infty} \sum_{m} B_{mn} \gamma_n \left(\frac{m\pi}{a}\right) \sin \gamma_n (y+h) \sin\left(\frac{m\pi x}{a}\right) \cos\left(\frac{n\pi z}{d}\right)$$

$$H_z = \frac{1}{j\omega\mu} \sum_{n=0}^{\infty} \sum_{m} B_{mn} \left(\frac{m\pi}{a}\right) \left(\frac{n\pi}{d}\right) \cosh \gamma_n (y+h) \sin\left(\frac{m\pi x}{a}\right) \sin\left(\frac{n\pi z}{d}\right)$$

For even m mode: m = 0,2,4, ...

$$E_y = \sum_{n=0}^{\infty} \sum_{m} A_{mn} \left(\frac{n\pi}{d}\right) \cosh \gamma_n (y+h) \sin\left(\frac{m\pi x}{a}\right) \sin\left(\frac{n\pi z}{d}\right)$$

$$E_z = \sum_{n=0}^{\infty} \sum_{m} A_{mn} \gamma_n \sinh \gamma_n (y+h) \sin\left(\frac{m\pi x}{a}\right) \cos\left(\frac{n\pi z}{d}\right)$$

(2.28)

$$H_x = \frac{1}{j\omega\mu} \sum_{n=0}^{\infty} \sum_{m} A_{mn} K_m^2 \cosh \gamma_n (y+h) \sin\left(\frac{m\pi x}{a}\right) \cos\left(\frac{n\pi z}{d}\right)$$

$$H_y = \frac{1}{j\omega\mu} \sum_{n=0}^{\infty} \sum_{m} A_{mn} \gamma_n \left(\frac{m\pi}{a}\right) \sinh \gamma_n (y+h) \cos\left(\frac{m\pi x}{a}\right) \sin\left(\frac{n\pi z}{d}\right)$$

$$H_z = \frac{-1}{j\omega\mu} \sum_{n=0}^{\infty} \sum_{m} A_{mn} \left(\frac{m\pi}{a}\right)\left(\frac{n\pi}{d}\right) \cosh \gamma_n (y+h) \cos\left(\frac{m\pi x}{a}\right) \sin\left(\frac{n\pi z}{d}\right)$$

Equations (2.27) and (2.28) are the field expressions for the single cell at the origin of the coordinate system. In order to express the fields in any slot in the guide, the phase change from slot to slot should be taken into account. To do this, the coefficients A_{mn} and B_{mn} should be modified to give the correct phase change with a new z^{ν} coordinate, which is related to the original z through,

$$z^{\nu} = z - \nu d$$

where z^{ν} is measured from the left hand wall of the νth slot. The new coefficients are given by

$$B_{mn}^{\nu} = B_{mn} e^{-j\nu\beta_0 d}$$
$$A_{mn}^{\nu} = A_{mn} e^{-j\nu\beta_0 d} \qquad (2.30)$$

Up to this point, the field representations for the region above the corrugated surface and in the slot have been derived with the unknown coefficients, A_p, B_p, A_{mn}, B_{mn}, to be determined. These coefficients may be obtained by the application of the continuity of the tangential magnetic and electric fields across the slot interface. It is noted that since only TE_{10} mode was assumed as the incident wave to the corrugated guide, the fields with the odd m mode are sufficient to specify the fields in the guide.

Before applying the continuity of the tangential electric and magnetic components at the interface of the slot for the unknown coefficients and the phase velocity in the guide, the tangential fields of odd m mode are rewritten here for convenience.

For $y > 0$:

$$E_z = \sum_{p=-\infty}^{\infty} \sum_{m} A_p \alpha_p \sin \alpha_p(y-b) \cos\left(\frac{m\pi x}{a}\right) e^{-j\beta_p z}$$

$$H_x = \frac{1}{j\omega\mu} \sum_{p=-\infty}^{\infty} \sum_{m} A_p K_m^2 \cosh \alpha_p(y-b) \cos\left(\frac{m\pi x}{a}\right) e^{-j\beta_p z} \tag{2.31}$$

$$H_z = \frac{1}{\omega\mu} \sum_{p=-\infty}^{\infty} \sum_{m} A_p \beta_p \frac{m\pi}{a} \cosh \alpha_p(y-b) \sin\left(\frac{m\pi x}{a}\right) e^{-j\beta_p z}$$

For $y < 0$:

$$E_z = \sum_{n=0}^{\infty} \sum_{m} B_{mn}^{\nu} \gamma_n \sinh \gamma_n(y+h) \cos\left(\frac{m\pi x}{a}\right) \cos\left(\frac{n\pi z}{d}\right)^{\nu}$$

(2.32)

$$H_x = \frac{1}{j\omega\mu} \sum_{n=0}^{\infty} \sum_{m} B_{mn}^{\nu} K_m^2 \cosh \gamma_n(y+h) \cos\left(\frac{m\pi x}{a}\right) \cos\left(\frac{n\pi z}{d}\right)^{\nu}$$

$$H_z = \frac{1}{j\omega\mu} \sum_{n=0}^{\infty} \sum_{m} B_{mn}^{\nu} \left(\frac{m\pi}{a}\right)\left(\frac{n\pi}{d}\right) \cosh \gamma_n(y+h) \sin\left(\frac{m\pi x}{a}\right) \sin\left(\frac{n\pi z}{d}\right)^{\nu}$$

The application of the continuity of the E_z and H_x components at the interface of the ν^{th} slot gives,

$$-\sum_{p=-\infty}^{\infty} A_p \alpha_p \sin \alpha_p b \, e^{-j\beta_p z^{\nu}} = \sum_{n=0}^{\infty} B_{mn} \gamma_n \sinh \gamma_n h \cos\left(\frac{n\pi z}{d}\right)^{\nu}$$

$$\sum_{p=-\infty}^{\infty} A_p \cosh \alpha_p b \, e^{-j\beta_p z^{\nu}} = \sum_{n=0}^{\infty} B_{mn} \cosh \gamma_n h \cos\left(\frac{m\Pi z^{\nu}}{d}\right) \tag{2.33}$$

with $0 \leq z^{\nu} \leq d$, and $\beta_p \nu d = \beta_0 \nu d + 2\Pi p \nu$. Solving for B_{mn} in equation (2.33) by means of the orthogonality of the $\cos(\frac{n\Pi z^{\nu}}{d})$ function and the $\sin(\frac{n\Pi z^{\nu}}{d})$ function over the interval of $z^{\nu}(0,d)$ yields the new set of equations for all n.

$$\frac{d}{2} \frac{\delta_n \gamma_n \sinh(\gamma_n h)}{(-1)^n e^{-j\beta_0 d} - 1} B_{mn} = - \sum_{p=-\infty}^{\infty} \frac{jA_p \alpha_p \beta_p \sinh(\alpha_p b)}{\alpha_p^2 - \gamma_n^2} \tag{2.34}$$

$$\frac{d}{2} \frac{\delta_n \cosh(\gamma_n h)}{(-1)^n e^{-j\beta_0 d} - 1} B_{mn} = \sum_{p=-\infty}^{\infty} \frac{jA_p \beta_p \cosh(\alpha_p b)}{\alpha_p^2 - \gamma_n^2} \tag{2.35}$$

where

$$\delta_n = \begin{cases} 2 & \text{for } n = 0 \\ 1 & \text{for } n > 0 \end{cases}$$

Multiplying equation (2.35) by γ_n and adding to equation (2.34), and also subtracting from equation (2.35), one obtains a simplified set of simultaneous equations,

$$\frac{\delta_n \, d\gamma_n \, e^{\gamma_n h}}{(-1)^n e^{-j\beta_0 d} - 1} B_{mn} = \sum_{p=-\infty}^{\infty} jA_p \beta_p \left[\frac{e^{\alpha_p b}}{\alpha_p + \gamma_n} + \frac{e^{-\alpha_p b}}{\alpha_p - \gamma_n} \right] \tag{2.36}$$

$$\frac{\delta_n \, d\gamma_n \, e^{-\gamma_n h}}{(-1)^n e^{-j\beta_0 d} - 1} B_{mn} = \sum_{p=-\infty}^{\infty} jA_p \beta_p \frac{e^{\alpha_p b}}{\alpha_p - \gamma_n} - \frac{e^{-\alpha_p b}}{\alpha_p - \gamma_n} \tag{2.37}$$

The set of equations (2.36) and (2.37) may be further simplified for the approximate solution, if the TE_{10} mode is assumed to be dominant for making the standing waves in the slot and for the higher order modes

the slot depth is considered to be infinite. Then, the factor $e^{-\gamma_n h}$ may be neglected for $n > 0$. Then, the set of equations may be rewritten as

$$\frac{d\, K_m\, e^{-jK_m h}\, B_{mo}}{e^{-j\beta_0 d} - 1} = \sum_{p=-\infty}^{\infty} A_p \beta_p \left[\frac{e^{\alpha_p b}}{\alpha_p - jK_m} - \frac{e^{-\alpha_p b}}{\alpha_p + jK_m} \right] \quad \text{for } n=0 \tag{2.38}$$

$$0 = \sum_{p=-\infty}^{\infty} A_p \beta_p \left[\frac{e^{\alpha_p b}}{\alpha_p - K_m} - \frac{e^{-\alpha_p b}}{\alpha_p + K_m} \right] \quad \text{for } n > 0 \tag{2.39}$$

The sets of equations (2.36), (2.37) and (2.38), (2.39) are the infinite sets of simultaneous equations. The set of equations may be solved exactly for the mode coefficients A_p, B_{mn}, and the phase constant β_p by applying the modified residue calculus (22).

In this study, since the exact mode amplitudes in the guide are not too critical for the determination of the radiation field, the exact evaluation of them will be deferred and only an approximate analysis will be presented.

For the first order approximation on the fields and the phase velocities in the guide, one may assume that the fields in the slot consist of only the standing wave of the dominant TE_{10} mode and the higher order modes have little contribution because of the geometry of narrow slots. Also since the TE_{10} mode excitation is assumed, one may take $m = 1$ for the approximate field representation in the region above the corrugation. The fields for $y > 0$ may be expressed as

$$E_y = j \sum_{p=-\infty}^{\infty} A_p \beta_p \cos\left(\frac{\Pi x}{a}\right) \cosh \alpha_p (y-b)\, e^{-j\beta_p z}$$

$$E_z = \sum_{p=-\infty}^{\infty} A_p \alpha_p \cos(\frac{\Pi x}{a}) \sinh \alpha_p(y-b)\, e^{-j\beta_p z}$$

$$H_x = \frac{1}{j\omega\mu} \sum_{p=-\infty}^{\infty} A_p K_1^2 \cos(\frac{\Pi x}{a}) \cosh \alpha_p(y-b)\, e^{-j\beta_p z} \qquad (2.40)$$

$$H_y = \frac{-1}{j\omega\mu} \sum_{p=-\infty}^{\infty} A_p \alpha_p \frac{\Pi}{a} \sin(\frac{\Pi x}{a}) \sinh \alpha_p(y-b)\, e^{-j\beta_p z}$$

$$H_z = \frac{1}{\omega\mu} \sum_{p=-\infty}^{\infty} A_p \beta_p \frac{\Pi}{a} \sin(\frac{\Pi x}{a}) \cosh \alpha_p(y-b)\, e^{-j\beta_p z}$$

where

$$K_1^2 = k^2 - (\frac{\Pi}{a})^2$$

$$\alpha_p^2 = \beta_p^2 - K_1^2$$

$$\beta_p = \beta_0 + \frac{2\Pi p}{D} \qquad p = 0, \pm 1, \pm 2, \ldots$$

For the corrugation of a finite thickness, the fields in the slot may be approximately represented in the quasi-static sense. Then, the fields in the slot for $y < 0$ may be written as,

For $y < 0$:

$$E_z = -B_{10} K_1 \sin K_1(y+h) \cos(\frac{\pi x}{a})\, e^{-j\nu\beta_0 D}$$

$$\text{for } \nu D < z < \nu D + d$$

$$= 0 \qquad \text{for } \nu D + d < z < (\nu+1)D \qquad (2.41)$$

$$H_x = \frac{1}{j\omega\mu} B_{10} K_1^2 \cos K_1(y+h) \cos(\frac{\Pi x}{a})\, e^{-j\nu\beta_0 D}$$

$$\text{for } \nu D < z < \nu D + d$$

$$= 0 \qquad \text{for } \nu D + d < z < (\nu+1)D$$

$$H_y = \frac{1}{j\omega\mu} B_{10} K_1 \frac{\Pi}{a} \sin K_1(y+h) \sin\left(\frac{\Pi x}{a}\right) e^{-j\nu\beta_0 D}$$

$$\text{for } \nu D < z < \nu D + d$$

$$= 0 \qquad \text{for } \nu D + d < z < (\nu+1)D$$

In equation (2.40), the amplitude of the individual harmonics may be determined from the orthogonality relation given in equation (2.4). The coefficient A_p is given by

$$A_p = \frac{1}{D} \frac{1}{\alpha_p \sinh(\alpha_p b)} \int_0^d B_{10} K_1 \sin(K_1 h) e^{j\beta_p z} dz$$

$$= \frac{d}{D} \frac{B_{10} K_1 \sin(K_1 h)}{\alpha_p \sinh(\alpha_p b)} \frac{\sin \frac{\beta_p d}{2}}{\frac{\beta_p d}{2}} e^{j\frac{\beta_p d}{2}} \qquad (2.42)$$

This completes the analysis for the first order field in the corrugated rectangular waveguide.

The phase constant β_p in the guide may be determined by solving the characteristic equation. The characteristic equation can be obtained by equating the tangential magnetic field across the slot mouth. Note that the fields cannot be matched over all values of z because of the approximation made for the field expansions but only at the center of the slot, $z = \nu D + \frac{d}{2}$. Matching the fields at the center of the slot yields the following characteristic equation.

$$\frac{\cot(K_1 h)}{K_1} = \frac{d}{D} \sum_{p=-\infty}^{\infty} \frac{\coth(\alpha_p b)}{\alpha_p} \frac{\sin\left(\frac{\beta_p d}{2}\right)}{\frac{\beta_p d}{2}} \qquad (2.43)$$

In equation (2.43), if β_p approaches k and $d \ll \lambda_0$, the zeroth term in the series may be predominant. Since the factor $\sin\left(\frac{\beta_p d}{2}\right) / \frac{\beta_p d}{2} \approx 1$,

it leads to the zeroth order dispersion relation as,

$$\frac{\cot(K_1 h)}{K_1} = \frac{d}{D} \frac{\cosh(\alpha_0 b)}{\alpha_0} \tag{2.44}$$

This zeroth order dispersion relation may also be derived by relating the surface impedances looking in the (+ y) direction and in the (- y) direction at y = 0 based on the transverse resonance condition,

$$\overleftarrow{z}_1 + \overrightarrow{z}_2 = 0 \tag{2.45}$$

In equation (2.45), $\overleftarrow{z}_1$ is the surface impedance looking in the (+ y) direction, which is given by

$$\overleftarrow{z}_1 = \left.\frac{E_z}{H_x}\right|_{y=0} = j\omega\mu \frac{\alpha_0}{K_1^2} \tanh \alpha_0 b \tag{2.46}$$

$\overrightarrow{z}_2$ is the surface impedance looking in the (- y) direction, which is given by

$$\overrightarrow{z}_2 = - \left.\frac{E_z}{H_x}\right|_{y=0} = \frac{d}{D} j\omega\mu \frac{1}{K_1} \tan K_1 h \tag{2.47}$$

In writing the expression for $\overrightarrow{z}_2$, the average impedance concept is used since the fields for y < 0 were defined only over the slot width (d) while the fields for y > 0 were defined across the slot and the corrugation tooth over one whole period (D). Equating $\overleftarrow{z}_1$ and $-\overrightarrow{z}_2$ yields the same dispersion relation as given in equation (2.44)

$$\frac{\cot(K_1 h)}{K_1} = \frac{d}{D} \frac{\coth(\alpha_0 b)}{\alpha_0} \tag{2.48}$$

In the corrugated waveguide, there exists two types of waves i.e.

the slow hybrid waves for the real α_0 and the fast hybrid waves for the imaginary values of α_0. In general, both waves propagate together in the guide. For the fast hybrid waves, the dispersion relations are given by the following equations.

For the first order approximation:

$$\cot(K_1 h) = -\frac{d}{D} \sum_{p=-\infty}^{\infty} \frac{K_1}{\alpha_p} \cot(\alpha_p b) \frac{\sin(\frac{\beta_p d}{2})}{\frac{\beta_p d}{2}} \tag{2.49}$$

For the zeroth order term in the series

$$\cot(K_1 h) = -\frac{d}{D} \frac{K_1}{\alpha_0} \cot(\alpha_0 b) \tag{2.50}$$

In order to study the behaviors of the hybrid fast wave and the hybrid slow waves in the guide, the characteristic equations for the zeroth order are rewritten here in the modified forms for the computational convenience.

$$\frac{h}{b} \frac{\cot\left[\frac{h}{a} \pi \sqrt{4(\frac{a}{\lambda_0})^2 - 1}\right]}{\frac{h}{a} \pi \sqrt{4(\frac{a}{\lambda_0})^2 - 1}} = \frac{d}{D} \frac{\coth(\alpha_0 b)}{\alpha_0 b} \quad \text{for slow wave} \tag{2.51}$$

$$= -\frac{d}{D} \frac{\cot(\alpha_0 b)}{\alpha_0 b} \quad \text{for fast wave} \tag{2.52}$$

The phase constants β_0 of the fundamental harmonic for the hybrid slow (β_{0s}) and fast waves (B_{of}) in the rectangular corrugated waveguide may be found by solving the attenuation constants α_0 in each set of equation (2.51) and substituting them into the expression for the phase constant

$$\beta_{os} = \sqrt{\alpha_0^2 + k^2 - (\frac{\Pi}{a})^2} \qquad \beta_{of} = \sqrt{-\alpha_0^2 + k^2 - \frac{\Pi}{a}} \qquad (2.53)$$

The phase constant β for the dominant TE_{10} mode in the uniform rectangular waveguide is given by

$$\beta = \sqrt{k^2 - (\frac{\Pi}{a})^2} \qquad (2.54)$$

The roots of the characteristic equations (2.51) and (2.52) were computed as a function of a/λ_0 with the predetermined guide dimension a/b = 2.25, h/a = 0.121, b/h = 3.664. Figure 2.3 is the plot of the roots for the slow and fast waves. For the fast wave, there are many roots satisfying equation (2.52) but only the correct roots satisfying the basic dispersion relation discussed in section 2.1 were plotted in the figure. Figure 2.4 is a normalized k - β diagram for the corrugated guide computed with the roots in Figure 2.3. It is seen in the diagram in the range of $0 < a/\lambda_0 < 2.121$, the dominant mode in the guide is a slow wave with the low frequency cutoff determined by the waveguide dimension for TE_{10} mode and the high frequency cutoff at $K_1 h = \Pi/2$. The phase velocity of the slow wave is not necessarily slower than the speed of light, but it is slower than the phase velocity of TE_{10} mode. In fact, the slow wave line intercepts the k = β line at $a/\lambda_0 = 1.05$. This suggests that if the waveguide width (a) is chosen in the range between $K_1 h = \Pi/2$ ($a/\lambda_0 = 4.152$) and the point where the slow wave line intercepts the k = β line, the phase velocity of the dominant wave in the guide will be slower than the speed of light. Hence, the choice of the guide dimension (a) in this range may maximize the efficiency of the surface wave excitation at the aperture. The fast wave starts just above

the slow wave cutoff condition at $K_1 h = \Pi/2$. It crosses the TE_{10} dispersion curve at $K_1 h = \Pi$ and then becomes a hybrid slow wave again. Between $K_1 h = \Pi/2$ and $K_1 h = 3\Pi/2$, the slow wave may not be predominant but mixed with the fast hybrid waves which are not shown in the figure. It should note that since the dispersion curve can be drawn with the predetermined guide dimensions only, for a different choice of the dimensions, it may differ from the one shown in Figure 2.4.

In order to see the dependence of the phase velocity of the surface wave in the corrugated guide upon the guide dimension, the ratio β_0/k was calculated as a function of the guide dimension from equation (2.51) and (2.53). Figure 2.5 is the curve for the β_0/k for the different values of (b) with the fixed value of a. The figure shows that the guide is the similar frequency sensitivity on the β_0/k as the ratio for the open corrugated surface. The spread of the ratio β_0/k variation over the frequencies decreases as the guide width (a) increases. One interesting fact is that the height of the guide can be minimized for the usable slow phase velocity: for instance, for β_0/k = 1.05 at 9 Ghz, the guide dimension is a = 3.93" (3 λ_0) and b = 0.7" (0.535 λ_0) which produces the β_0/k = 1.03 at 7 Ghz and 1.08 at 11 Ghz. This variation of the ratio is almost identical to that for the open infinitely wide corrugated structure over the same frequencies. The case for the open corrugated surface will be discussed in the next section in detail.

As the summary of the results from the approximate field analysis of the corrugated waveguide, the corrugated rectangular waveguide may support predominantly slow hybrid surface waves by adjusting the guide dimension so that the surface wave excitation efficiency may be maximized.

The guide dimension of a = $2\sim3\lambda_0$, b = $0.5\sim0.6\lambda_0$ may be the smallest possible guide for the slow surface wave of β_0/k = 1.05 at 9 Ghz to excite an open corrugated surface with the same ratio of β_0/k.

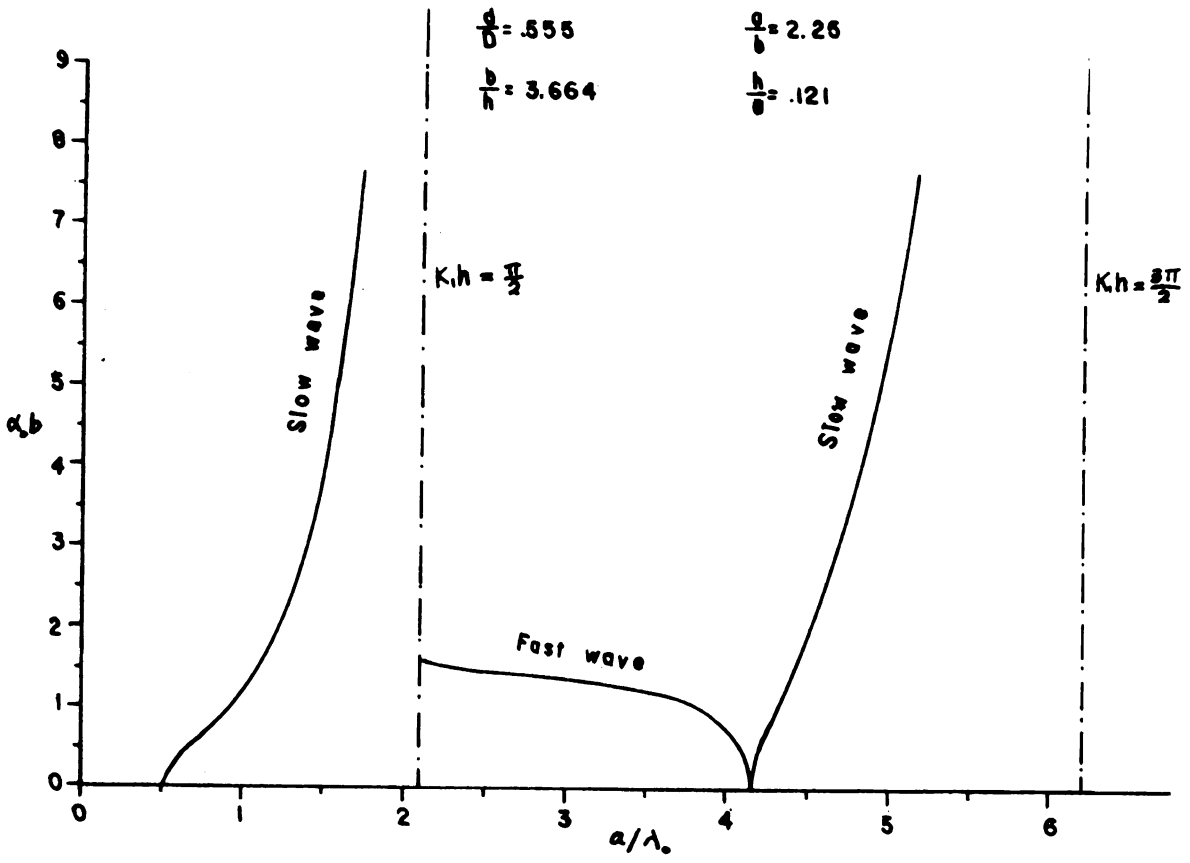

Figure 2.3 Normalized Attenuation Constant in a Corrugated Rectangular Waveguide

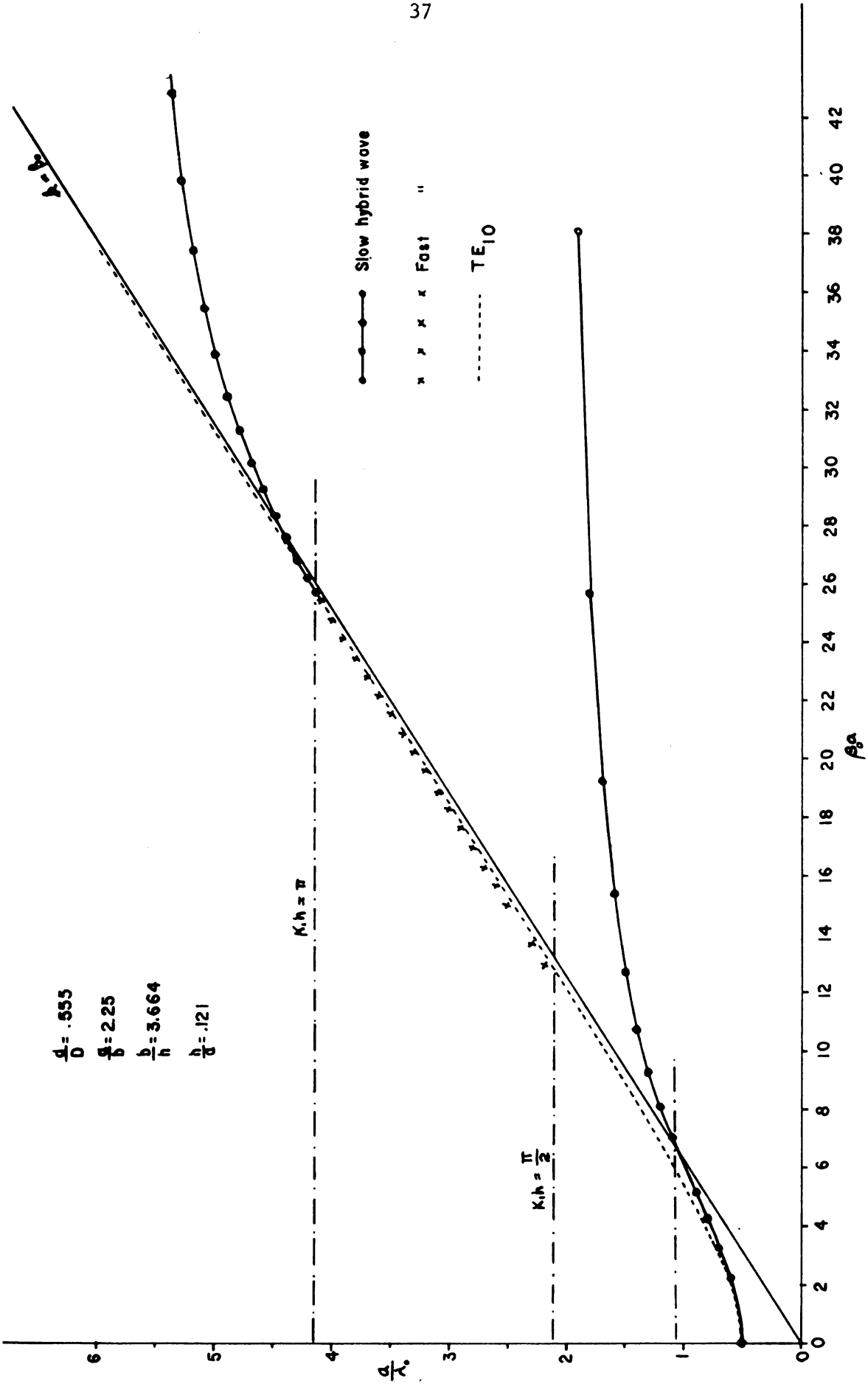

Figure 2.4 Normalized k- diagram for a Corrugated Rectangular Waveguide

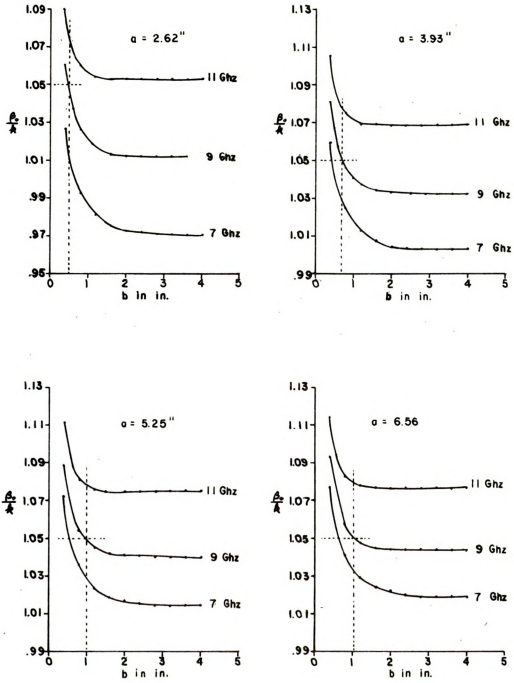

Figure 2.5 $\frac{\beta_0}{k}$ Ratio versus Corrugated Guide Dimensions

CHAPTER III

FLAT CORRUGATED CONDUCTING SURFACE

The theoretical treatments of the electromagnetic wave propagation above the infinitely wide and transversely corrugated structure are found in several papers by Cutler (61), Brillouin (11), Whitehead (16), Feodora Berz (17) and Hurd (15). These papers assume the existence of a pure TM surface wave on the reactive surface of infinite size without the prior knowledge of the excitation mechanism of such a wave.

For the application of such a reactive surface to a practical radiating system, its transverse dimension has to be reduced to a finite width. Because of this finiteness in the transverse dimension, it poses a great difficulty in the theoretical treatment on the fields and hampers a clear understanding of the wave guiding and radiating properties of the slow surface waves. Thus, in this chapter, an approximate field analysis will be presented and its validity will be verified experimentally in the subsequent chapters. The structure to be investigated consists of three regions: (1) a constant reactive surface, (2) a tapered reactive surface, and (3) a finite ground plane as shown in Figure 3.1.

3.1 Fields on the Uniform Corrugated Surface

It is known that a reactive surface can support an inhomogeneous

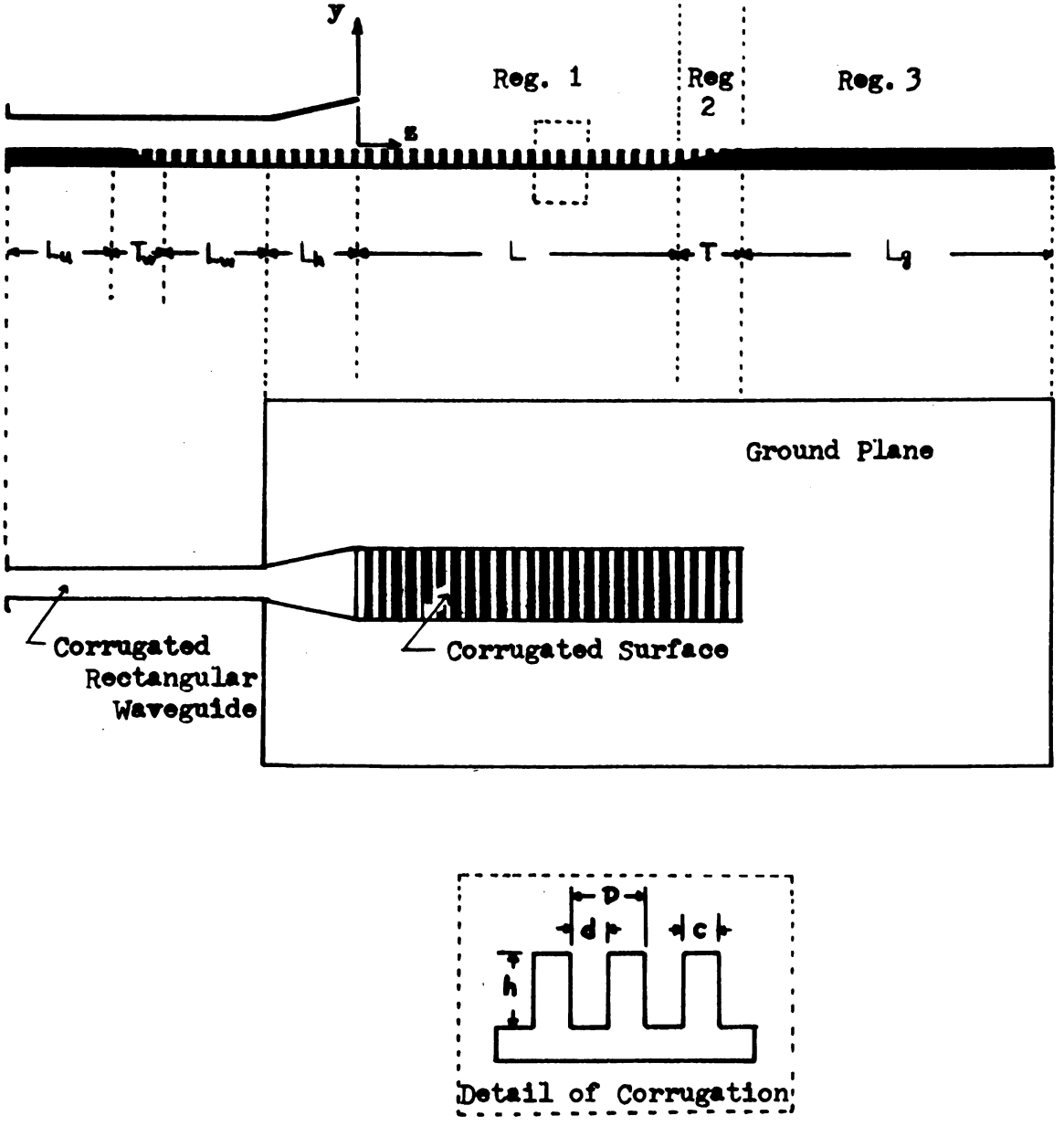

Figure 3.1 Surface Wave Guiding Structure

plane wave which decays exponentially in the direction transverse to the direction of propagation. This inhomogeneous plane wave is termed a slow surface wave, or often called a Zenneck wave (36). If such a slow surface wave can be guided on a reactive surface, it will result in an end-fire radiation. However, theoretically only a reactive surface of transversely infinite extent can support a pure TM surface wave (34), while a desired practical structure of finite size may support a modified slow wave rather than a pure surface wave mode. The exact nature of waves on such a finite reactive surface is not known because of the mathematical difficulty imposed by the unusual boundary conditions. Therefore, an approximate approach will be employed to treat the finite slow surface wave guiding structure, and also it will be assumed that such a finite structure may support a pure surface wave provided that the transverse dimension is of several wavelengths and that a completely efficient slow wave excitation can be realized.

One of the simplest and conceptually efficient surface wave excitors may be realized by extending the corrugated bottom wall of the corrugated rectangular waveguide discussed in Chapter II to a desired length beyond the trancated waveguide aperture. If the dimensions of the rectangular waveguide are chosen so that the dominant wave in the corrugated waveguide is a slow hybrid wave whose phase velocity is close to the required phase velocity for the wave on the open corrugated plane, the waveguide may efficiently produce slow waves on the guiding structure. In order to make a smooth transition from a hybrid surface wave in the rectangular waveguide to a TM surface wave on the open corrugated surface, the top and side walls of the rectangular guide are

gradually flared out to form a type of horn feed. If this transition is sufficiently smooth and long, one may expect the dominant wave in the horn to remain to be the slow hybrid mode mentioned in section 2.2 with a negligible reflection at the horn aperture. Thus, the fields over the flat corrugated surface may be deduced from the waves inside the corrugated rectangular guide with some appropriate modifications. With this approximate approach and the assumption of the TE_{10} mode excitation at the start of the corrugated rectangular waveguide, the field expressions on the open surface can be deduced from equation (2.40). If the top wall of the guide, b, is allowed to increase indefinitely, the field expressions over the open corrugated surface may be written as follows:

For $y > 0$

$$E_y = j \sum_{p=-\infty}^{\infty} A'_p \beta_p \cos\left(\frac{\Pi x}{a}\right) e^{-\alpha_p y} e^{-j\beta_p z}$$

$$E_z = - \sum_{p=-\infty}^{\infty} A'_p \alpha_p \cos\left(\frac{\Pi x}{a}\right) e^{-\alpha_p y} e^{-j\beta_p z}$$

$$H_x = \frac{1}{j\omega\mu} \sum_{p=-\infty}^{\infty} A'_p K_1^2 \cos\left(\frac{\Pi x}{a}\right) e^{-\alpha_p y} e^{-j\beta_p z} \qquad (3.1)$$

$$H_y = \frac{1}{j\omega\mu} \sum_{p=-\infty}^{\infty} A'_p \alpha_p \frac{\Pi}{a} \sin\left(\frac{\Pi x}{a}\right) e^{-\alpha_p y} e^{-j\beta_p z}$$

$$H_z = \frac{1}{j\omega\mu} \sum_{p=-\infty}^{\infty} A'_p \beta_p \frac{\Pi}{a} \sin\left(\frac{\Pi x}{a}\right) e^{-\alpha_p y} e^{-j\beta_p z}$$

where

$$A_p' = \lim_{b\to\infty} A_p \frac{e^{\alpha_0 b}}{2}$$

$$K_1^2 = k^2 - \left(\frac{\Pi}{a}\right)^2$$

$$\alpha_p^2 = \beta_p^2 - K_1^2$$

$$\beta_p = \beta_0 + \frac{2\Pi p}{D} \qquad p = 0, \pm 1, \pm 2, \ldots$$

With the assumption that the fields for $y < 0$ remain the same as those expressed in equation (2.41), the first order value of the coefficient, A_p', in equation (3.1) can be determined by the usual Fourier analysis as,

$$A_p' = \frac{d}{D} \frac{B_{10} K_1 \sin(K_1 h)}{\alpha_p} e^{j\frac{\beta_p d}{2}} \frac{\sin(\frac{\beta_p d}{2})}{\frac{\beta_p d}{2}} \tag{3.2}$$

By equating the tangential magnetic fields for $y > 0$ and $y < 0$ at the center of the slot, $z = \nu D + d/2$, over the slot mouth, a characteristic equation is obtained as

$$K_1 \cot(K_1 h) = \frac{d}{D} \sum_{p=-\infty}^{\infty} \frac{1}{\alpha_p} \frac{\sin(\frac{\beta_p d}{2})}{\frac{\beta_p d}{2}} \tag{3.3}$$

For $d \ll \lambda_0$, the factor $\sin(\frac{\beta_p d}{2}) / \frac{\beta_p d}{2}$ approaches unity for small p and zero for large p. Thus, the characteristic equation may be rewritten as

$$K_1 \cot(K_1 h) = \frac{d}{D} \sum_{p=-\infty}^{\infty} \frac{1}{\alpha_p} \tag{3.4}$$

Next, if the width of the waveguide, a, is increased to infinity, the field expressions (3.1) become the well known fields of an infinitely wide and long flat corrugated surface, i.e.,

$$\begin{aligned} E_y &= j \sum_{p=-\infty}^{\infty} A'_p \beta_p \, e^{-\alpha_p y} \, e^{-j\beta_p z} \\ E_z &= -\sum_{p=-\infty}^{\infty} A'_p \alpha_p \, e^{-\alpha_p y} \, e^{-j\beta_p z} \\ H_x &= \frac{1}{j\omega\mu} \sum_{p=-\infty}^{\infty} A'_p k^2 \, e^{-\alpha_p y} \, e^{-j\beta_p z} \\ H_y &= H_z = 0 \end{aligned} \tag{3.5}$$

The characteristic equation for this case becomes

$$k \cot(kh) = \frac{d}{D} \sum_{p=-\infty}^{\infty} \frac{1}{\alpha_p} \tag{3.6}$$

The field expressions and the characteristic equation expressed in equations (3.1) to (3.6) are still too complicated in the numerical calculation because the series involves infinite space harmonics. For a finite structure of practical use, it may be reasonable to consider only the fundamental harmonic, since the magnitude of the spectrum drops off rapidly as the order of the harmonics increases. The approximate field expressions on the flat corrugated surface with a finite transverse dimension can then be written from equation (3.1) as

$$E_y = -\frac{\omega\mu\beta_0}{K_1^2} H_0 \cos(\frac{\pi x}{a}) e^{-\alpha_0 y} e^{-j\beta_0 z}$$

$$E_z = -j\frac{\omega\mu\alpha_0}{K_1^2} H_0 \cos(\frac{\pi x}{a}) e^{-\alpha_0 y} e^{-j\beta_0 z}$$

$$H_x = H_0 \cos(\frac{\pi x}{a}) e^{-\alpha_0 y} e^{-j\beta_0 z} \qquad (3.7)$$

$$H_y = \frac{\alpha_0 \frac{\pi}{a}}{K_1^2} H_0 \sin(\frac{\pi x}{a}) e^{-\alpha_0 y} e^{-j\beta_0 z}$$

$$H_z = \frac{j\beta_0 \frac{\pi}{a}}{K_1^2} H_0 \sin(\frac{\pi x}{a}) e^{-\alpha_0 y} e^{-j\beta_0 z}$$

where

$$H_o = \frac{K_1^2}{j\omega\mu} A_0'$$

The characteristic equation is also simplified to

$$\cot(K_1 h) = \frac{d}{D} \frac{K_1}{\alpha_0} \qquad (3.8)$$

For the infinitely wide corrugated surface, the zero order expressions for the field are

$$H_z = H_y = 0$$

$$H_x = H_0 e^{-\alpha_0 y} e^{-j\beta_0 z}$$

$$E_z = -\frac{j\alpha_0}{\omega\varepsilon} H_0 e^{-\alpha_0 y} e^{-j\beta_0 z} \qquad (3.9)$$

$$E_y = -\frac{\beta_0}{\omega\varepsilon} H_0 e^{-\alpha_0 y} e^{-j\beta_0 z}$$

with the characteristic equation given as

$$\cot(kh) = \frac{d}{D}\frac{k}{\alpha_0} = \frac{d}{D}\frac{1}{\sqrt{\left(\frac{\beta_0}{k}\right)^2 - 1}} \tag{3.10}$$

Up to this point, the fields on the open corrugated surface have been approximated from the fields inside the corrugated rectangular waveguide assuming the perfect field transition from the hybrid surface wave to the TM surface wave at the exciting aperture. The fields on the infinitely wide corrugated surface with infinitely thin corrugations ($D \approx d$) can be derived exactly from the solution of a wave equation with the proper boundary conditions. On the surface which is excited by a magnetic field H_x parallel to the edge of corrugation and an electric field E_y normal to the surface, the fields may be described by a TM wave. For such a TM wave, Maxwell's equations reduced to

$$E_y = \frac{-j}{\omega\epsilon}\frac{\partial H_x}{\partial z}$$

$$E_z = \frac{j}{\omega\epsilon}\frac{\partial H_x}{\partial y} \tag{3.11}$$

$$\frac{\partial^2 H_x}{\partial y^2} + \frac{\partial^2 H_x}{\partial z^2} + k^2 H_x = 0$$

Because of the periodic nature of the structure, the fields over the corrugation can be expressed as the sum of an infinite number of space harmonics based on the theorem of Floquet. The solution to the wave equation (3.11) may be expressed as

$$H_x = \sum_{p=-\infty}^{\infty} A_p \, e^{-\alpha_p y - j\beta_p z}$$

$$E_y = \frac{-1}{\omega\varepsilon} \sum_{p=-\infty}^{\infty} A_p \beta_p \, e^{-\alpha_p y - j\beta_p z} \tag{3.12}$$

$$E_z = \frac{-j}{\omega\varepsilon} \sum_{p=-\infty}^{\infty} A_p \alpha_p \, e^{-\alpha_p y - j\beta_p z}$$

$$\alpha_p = + \sqrt{\beta_p^2 - k^2} \tag{3.13}$$

$$\beta_p = \beta_0 + \frac{2\pi p}{D} \qquad p = 0, \pm 1, \pm 2, \ldots$$

where the sign of α_p is taken to be positive for the slow surface waves.

If the width of the corrugation gap, d = D, is much smaller than the free space wavelength, the only propagating mode in the ν^{th} slot may be the TEM mode and the higher order modes may be attenuated as they reach the bottom of the slot. The fields in the ν^{th} slot may be represented by the superposition of all modes which satisfy the boundary conditions at the bottom and the sides of the slot. That is,

$$H_x = \sum_{n=0}^{\infty} B_n^{\nu} \cosh \gamma_n(y+h) \cos\left(\frac{n\pi z}{D}\right)^{\nu}$$

$$E_y = \frac{j}{\omega\varepsilon} \sum_{n=0}^{\infty} B_n^{\nu} \frac{n\pi}{d} \cosh \gamma_n(y+h) \sin\left(\frac{n\pi z}{D}\right)^{\nu} \tag{3.14}$$

$$E_z = \frac{j}{\omega\varepsilon} \sum_{n=0}^{\infty} B_n^{\nu} \gamma_n \sinh \gamma_n(y+h) \cos\left(\frac{n\pi z}{D}\right)^{\nu}$$

where

$$\gamma_n = \sqrt{(\frac{n\pi}{D})^2 - k^2}$$

and z^ν is measured from the left side wall of the ν^{th} slot and it is related to z through

$$z_\nu = z - \nu D$$

The coefficient B_n^ν is realted to B_n by

$$B_n^\nu = B_n \, e^{-j\nu\beta_0 D}$$

to give the correct phase change from slot to slot.

The unknowns, A_p, B_n, and β_p in equation (3.12) and (3.14) are determined by the application of the continuity of the tangential magnetic and electric fields at the interface of the ν^{th} slot (y=0) as follows:

$$\sum_{p=-\infty}^{\infty} A_p \, e^{-j\beta_p z} = \sum_{n=0}^{\infty} B_n^\nu \cosh(\gamma_n h) \cos(\frac{n\pi z^\nu}{D})$$

$$-\sum_{p=-\infty}^{\infty} A_p \alpha_p \, e^{-j\beta_p z} = \sum_{n=0}^{\infty} B_n^\nu \gamma_n \sinh(\gamma_n h) \cos(\frac{n\pi z^\nu}{D}) \qquad (3.15)$$

$$\text{for } 0 \leq z^\nu \leq D$$

By applying the orthogonality of the function $\cos(\frac{n\pi z^\nu}{D})$ over $0 \leq z^\nu \leq D$ and with some algebraic manipulations, the set of equations (3.15) is reduced to an infinite set of simultaneous equations as

$$\frac{d}{2}\,\frac{\varepsilon_n B_n \gamma_n e^{\gamma_n h}}{(-1)^n e^{-j\beta_0 d} - 1} = -\sum_{p=-\infty}^{\infty} \frac{jA_p\beta_p}{\alpha_p + \gamma_p}$$

$$\frac{d}{2}\,\frac{\varepsilon_n B_n \gamma_n e^{-\gamma_n h}}{(-1)^n e^{-j\beta_0 d} - 1} = \sum_{p=-\infty}^{\infty} \frac{jA_p\beta_p}{\alpha_p - \gamma_n} \qquad (3.16)$$

where

$$\varepsilon_n = 1 \quad \text{for } n > 0$$

$$2 \quad \text{for } n = 0$$

This infinite set of simultaneous equations can be solved for A_p and β_p exactly with the use of the residue calculus. Hurd (15) was the first one who solved this set of equations. According to his results, the mode amplitudes and the phase constants of the higher order modes are very small for the case of $D \ll \lambda_0$ and $h \ll \lambda_0$. For $h < 0.2$, the α_0 may be approximated from the exact solution (24) to

$$\alpha_0 = k \tan[k(h - \frac{a}{\pi} \ln 2)] \qquad (3.17)$$

Thus, the simple first order approximation based on the transverse resonant condition applied to the dominant mode may be justified if $d \ll \lambda$. Then, for the first order approximation, one may represent the fields above the corrugation with the fundamental harmonic:

For $y > 0$

$$H_{x_1} = H_0 e^{-\alpha_0 y - j\beta_0 z}$$

$$E_{z_1} = \frac{-j\alpha_0}{\omega\varepsilon} H_0 e^{-\alpha_0 y - j\beta_0 z}$$

$$E_{y_1} = \frac{-\beta_0}{\omega\varepsilon} H_o e^{-\alpha_0 y - j\beta_0 z} \tag{3.18}$$

In the slot, only the TEM mode is reflected from the base of the slot, producing a standing wave at the mouth of the slot, while all the higher order modes are attenuating waves. Thus, the fields in the slot are expressed as,

$$\begin{aligned} H_{x_2} &= B_0 \cos k(y+h) \\ E_{z_2} &= \frac{-j}{\omega\varepsilon} B_0 k \sin k(y+h) \end{aligned} \tag{3.19}$$

The transverse resonance condition at the interface y=0 is,

$$\overleftarrow{Z}_s + \overrightarrow{Z}_s = 0 \tag{3.20}$$

where $\overleftarrow{Z}_s$ and $\overrightarrow{Z}_s$ are the surface impedances looking up and down at the interface respectively. In this case, the surface impedances $\overrightarrow{Z}_s$ and $\overrightarrow{Z}_s$ at y=0 are given as

$$\begin{aligned} \overleftarrow{z}_s &= \frac{E_{z_1}}{H_{x_1}} = -\frac{j\alpha_0}{\omega\varepsilon} \\ \overrightarrow{z}_s &= -\frac{E_{z_2}}{H_{x_2}} = +j\frac{k}{\omega\varepsilon} \tan kh \end{aligned} \tag{3.21}$$

The substitution of equation (3.21) into equation (3.20) yields the characteristic equation for the phase constant as

$$\cot kh = \frac{k}{\alpha_0} \tag{3.22}$$

For the corrugation with the finite thickness ($D \neq d$), one may use the average surface impedance $\vec{z}_s' = j \frac{d}{D} \vec{z}_s$ to modify equation (3.22) to

$$\cot kh = \frac{d}{D} \frac{k}{\alpha_0}$$

or

$$\cot kh = \frac{d}{D} \frac{1}{\sqrt{\left(\frac{\beta_0}{k}\right)^2 - 1}} \tag{3.23}$$

Equations (3.18) and (3.23) are identical to the equations (3.9) and (3.10) which were derived approximately from the field expressions in the corrugated rectangular waveguide. Thus, the validity of the waveguide approach for the first order approximation is proved to be reasonable.

This concludes the approximate field analysis on the open corrugated surface with the perfect match at its end of the guiding surface. This approximate analysis tends to suggest the fact that a surface wave can be efficiently launched on the sufficiently wide corrugated surface, if the side and top walls of the corrugated guide are gradually flared out to make smooth transition. This analysis was carried out under four restricted assumptions; there are (1) a perfect transition from TE_{10} mode in the uniform waveguide to the hybrid mode in the corrugated waveguide, (2) a perfect transition from the hybrid slow surface wave to the pure TM slow surface wave at the horn aperture, (3) a sufficiently wide corrugated plate as the surface wave guiding surface beyond the horn aperture and (4) a perfect match at the end of the corrugated surface.

The requirements on the perfect match in the guide and at the end of the guiding surface may be realized to some extent by tapering the corrugations as shown in Figure 3.1. An exact analysis of the scattering of a surface wave by Kay (45) shows that the power reflection coefficient at the discontinuity between a reactive surface and a conducting plane can be given by

$$|R| = \frac{x^4}{(1 + x^2)\,(1 + \sqrt{1 + x^2})} \tag{3.24}$$

where $x = \frac{X_{TM}}{\eta_0} = \frac{\alpha_0}{k}$ normalized reactance.

Kane (46) also showed that the reflection coefficient at the discontinuity can be given by

$$k = \frac{x^2}{1 + x^2 + \sqrt{1 + x^2}}\, e^{-j\phi}$$

$$\phi = 2 \tan^{-1}\left[\frac{\sinh^{-1} x}{\pi}\right] \tag{3.25}$$

In an approximate analysis by Luck (61) the magnitude of the reflection coefficient was given as

$$|R| = \frac{\beta_0 - k}{\beta_0} \tag{3.26}$$

All these expressions for the reflection coefficient are based on the assumption that the corrugated plane has an infinite transverse dimension. Nevertheless, these expressions give some indication for a corrugated surface with finite transverse dimension. In the experiment, the theoretical prediction was found to be close to the measured

value.

As for the assumption of the perfect mode conversions from the incident TE_{10} to the hybrid wave in the corrugated guide and then to the non-radiating TM surface wave at the horn aperture, it may be accomplished by a gradual flare of the guide aperture to some degrees. However, this gradual flare may assure a good match at the aperture but not a perfect mode conversion, becasue an aperture of finite size can not excite a pure surface wave (34). Therefore, in the practical situation, the feed radiation cannot be ignored in a strict sense. It has been known that any analytical treatment on such an aperture problem is not possible mathematically, unless one of the aperture dimensions is of infinite extent. For example, if the side walls of the corrugated guide are extended infinitely to form a parallel plate guide excitor, the problem may be solved exactly by means of the Wiener-Hopf technique (36). Still this infinite geometry is far from the reality. Therefore, the effect of the feed radiation can only be taken approximately by a simple method such as an integration of the reasonably assumed aperture fields.

The adoption of a sufficiently wide corrugated surface is simply an intuitive effort to closely simulate the infinitely wide surface so that a pure surface wave with a uniform amplitude can be guided. In the experiment, it was found that the transverse field distribution remained close to the cosine function distribution of $\cos(\pi x/a)$ and that only a very small current was induced on the ground plane outside the corrugated surface. This signifies that the surface wave is almost totally trapped on the corrugated surface and the discontinuities along the two longitudinal boundaries may give little effect on

the radiation pattern, if the width of the corrugated surface is of several wavelengths.

3.2 Fields on the Tapered Corrugated Surface

It has been the accepted fact that a surface wave radiates at the discontinuities along the guiding surface. When the reactive surface is tapered as shown in Figure 3.1, the surface wave incident from the left along the constant reactive surface gives off a part of energy along the tapered surface and the rest of energy at the discontinuity between the tapered section and the ground plane.

Felsen (52) showed that when the constant reactive surface is terminated by an infinitely long tapered reactive surface, the radiation pattern consists of two components, one from the surface wave and the other from the continuous spectrum. The contribution due to the continuous spectrum was shown to be much smaller than that due to the surface wave. His study also verifies the existence of a surface wave on the continuously varying reactive surface. However, it is not theoretically possible to determine the fields over the varying reactive surface of finite size.

Hence, the fields on a short tapered reactive surface (less than one wavelength) may be found based on the approximate method. Recognizing that the phase constant and the attenuation constant of the surface wave are functions of the surface impedance, the fields over the tapered section may be assumed to be the following type.

$$H'_{x_1} = H_0 \, e^{-\alpha(z)y - j\beta(z)z}$$

$$E'_{z_1} = \frac{j}{\omega\varepsilon} \frac{\partial H_x}{\partial y} = -\frac{j\alpha(z)}{\omega\varepsilon} H_x \qquad (3.27)$$

$$E'_{y_1} = \frac{-j}{\omega\varepsilon} \frac{\partial H_x}{\partial z} = \frac{+j}{\omega\varepsilon} \left[y \frac{\partial \alpha(z)}{\partial z} + j\beta(z) + jz \frac{\partial \beta(z)}{\partial z} \right] H_x$$

Based on the transverse resonant condition, it can be shown that the surface impedances at y=0 are given by

$$\overleftarrow{z}'_s = \left. \frac{E'_{z_1}}{H'_{x_1}} \right|_{y=0} = \frac{-j\alpha(z)}{\omega\varepsilon} \tag{3.28}$$

$$\overrightarrow{z}'_s = - \left. \frac{E_{z_2}}{H_{x_2}} \right|_{y=0} = j \frac{d}{D} \frac{k}{\omega\varepsilon} \tan \left[kh \frac{L + T - z}{T} \right]$$

By equating $\overrightarrow{z}_s$ to $-\overrightarrow{z}_s$, one obtains a characteristic equation for the tapered section,

$$\alpha(z) \approx \frac{d}{D} k \tan \left[kh \frac{L + T - z}{z} \right] \tag{3.29}$$

and for the constant reactive section,

$$\alpha_0 \approx \frac{d}{D} k \tan kh \tag{3.30}$$

The $\alpha(z)$ may be expressed in terms of α_0 by dividing equation (3.29) by equation (3.30).

$$\alpha(z) = \alpha_0 \frac{\tan \left[kh \frac{L + T - z}{T} \right]}{\tanh[kh]} \tag{3.31}$$

If kh<<1, $\alpha(z)$ may be approximated by

$$\alpha(z) \approx \alpha_0 \frac{L + T - z}{T} \tag{3.32}$$

The phase constant $\beta(z)$ on the tapered section is then approximately

$$\beta(z) \approx \sqrt{k^2 + \left(\alpha_0 \frac{L + T - z}{T} \right)^2} \tag{3.33}$$

With these approximate expressions for $\alpha(z)$ and $\beta(z)$, the continuity of the fields at z = L is examined below.

$$\alpha(z)\Big|_{z=L} = \alpha_0 \qquad \beta(z)\Big|_{z=L} = \beta_0$$

hence

$$H_x'\Big|_{z=L} = H_x\Big|_{z=L} \qquad E_z'\Big|_{z=L} = E_z\Big|_{z=L} \tag{3.34}$$

Namely, the H_x and E_z components satisfy the continuity at the boundary z=L. For the E_y component,

$$\frac{\partial \alpha(z)}{\partial z}\Big|_{z=L} \approx - \frac{\alpha_0}{T} \quad \text{if } kT << 1$$

$$\frac{\partial \beta(z)}{\partial z}\Big|_{z=L} \approx \frac{1}{\beta_0} \left(- \frac{\alpha_0^2}{T} \right) \tag{3.35}$$

Hence,

$$E_y'\Big|_{z=L} = - \frac{j}{\omega\varepsilon} \left[\frac{\alpha_0}{T} y - j\beta_0 + j \frac{\alpha_0^2}{T} \frac{L}{\beta_0} \right] H_0 e^{-\alpha_0 y - j\beta_0 L} \tag{3.36a}$$

$$E_y\Big|_{z=L} = - \frac{\beta_0}{\omega\varepsilon} H_0 e^{-\alpha_0 y - j\beta_0 L} \tag{3.36b}$$

Equation (3.36) shows that the E_y component is not continuous at z=L. This is expected since a part of wave radiated at the discontinuity was neglected in deriving the field expressions. However, for the dominant term of equation (3.36a) is the second term in the vicinity of the guiding surface. Therefore, one may express the fields over the tapered section as

$$H_x' = H_0 e^{-\alpha(z)y - j\beta(z)z}$$

$$E_z' = \frac{-j\alpha_0}{\omega\varepsilon}\left(\frac{L + T - z}{T}\right) H_x' \qquad (3.37)$$

$$E_y' = \frac{-\beta_0}{\omega\varepsilon} H_x'$$

where

$$\alpha_2(z) \approx \alpha_0\left(\frac{L + T - z}{T}\right)$$

$$\beta(z) \approx \sqrt{k^2 + \left(\alpha_0 \frac{L + T - z}{T}\right)^2}$$

Since the tapered section is assumed to be short compared to the wavelength, one may further approximate $\beta(z)$ to be equal to β_0 for the radiation field calculation.

3.3 Induced Fields on the Finite Ground Plane

The induced fields on a finite ground plane due to an aperture field lying on the ground plane have not been solved rigorously because of the finite edge problems. In this section, a classical method of

successive approximation will be applied to the problem. For the first approximation, this method assumes that the aperture fields on a finite ground plane establish the same fields at any point in space as that maintained by the same aperture fields on an infinitely large ground plane. Hence, the electric current distribution on the finite ground plane is assumed to be approximately the same as the current distribution which would exist on the portion of an infinite ground plane. Thus, the problem is reduced to that of finding the fields due to a source distribution in the presence of an infinite ground plane. The fields in space for this problem can be determined by means of Huygens' principle. The geometry of the aperture and the ground plane is shown in Figure 3.2.

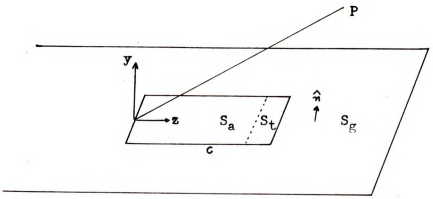

Figure 3.2 Coordinates of Flat Corrugated Surface and Ground Plane.

In determining the electromagnetic fields arising from a prescribed set of sources in an isotropic homogeneous medium, the fields at a point lying outside a surface which encloses all the sources may be expressed in terms of the field vectors over the surface based on the Kirchhoff's theory. According to the theory, the fields at a point in the space due to the prescribed $\vec{E}$ and $\vec{H}$ vectors over an aperture S on a closed surface may be expressed as

$$\vec{E}_p = \frac{1}{4\pi} \int_S \left\{ [(\hat{n} \times \vec{E}) \times \nabla G] + [(\hat{n} \cdot \vec{E}) \nabla G] - j\omega\mu [(\hat{n} \times \vec{H}) G] \right\} ds - \frac{1}{4\pi\varepsilon j\omega} \int_C \nabla G (\vec{H} \cdot d\vec{\ell}) \qquad (3.38)$$

$$\vec{H}_p = \frac{1}{4\pi} \int_S \left\{ [(\hat{n} \times \vec{H}) \times \nabla G] + [(\hat{n} \cdot \vec{H}) \nabla G] + j\omega\varepsilon [(\hat{n} \times \vec{E}) G] \right\} ds + \frac{1}{4\pi\mu j\omega} \int_C \nabla G (\vec{E} \cdot d\vec{\ell}) \qquad (3.39)$$

where $\vec{E}$, $\vec{H}$ = prescribed field vectors on the aperture

n = outward normal unit vector

G = free space Green's function $= \dfrac{e^{-jk|R-R'|}}{|R-R'|}$

S = aperture area on a closed surface

C = closed contour around the aperture

The line integrals in equation (3.38) and equation (3.39), often called Kottler's integral, are included to take into account the discontinuities of the tangential components of $\vec{E}$ and $\vec{H}$ along the aperture boundary.

For the case of the antenna aperture located on an infinitely large

ground plane, the field calculation in the space may be greatly simplified by the application of Huygens' principle. Based on the Huygens' principle, the aperture fields in the infinitely large ground plane may be replaced by the modified magnetic current of $2\vec{K}$ in the place of the aperture surface S, which produces the exactly same field in space as the original aperture fields. Therefore, the integral formulation of the fields in the space maintained by a prescribed field distribution on an infinitely large ground plane can be reduced to

$$\vec{E}_p = 2 \frac{1}{4\pi} \int_S (\hat{n} \times \vec{E}) \times \nabla G \, ds \tag{3.40}$$

$$\vec{H}_p = 2 \frac{j\omega\varepsilon}{4\pi} \int_S (\hat{n} \times \vec{E}) \, G \, ds \tag{3.41}$$

where the outward normal unit vector $\hat{n} = \hat{y}$ and the free space z-dimensional Green's function $G(R,R')$ is given by

$$G = \frac{e^{-jk\sqrt{(x-x')^2 + (y-y')^2 + (z-z')^2}}}{\sqrt{(x-x')^2 + (y+y') + (z-z')^2}} \tag{3.42}$$

where the source coordinates are designated by the prime. The components of the electric field $\vec{E}$ on the antenna aperture are given from equation (3.7) and (3.37) as follows:

For the constant reactive surface,

$$E_{z_a} = -j \frac{\omega\mu\alpha_0}{K_1^2} H_0 \cos \frac{\pi x'}{a} e^{-j\beta_0 z'} \tag{3.43}$$

$$E_{y_a} = -\frac{\omega\mu\beta_0}{K_1^2} H_0 \cos\frac{\pi x'}{a} e^{-j\beta_0 z} \tag{3.43}$$

For the tapered reactive surface

$$E_{z_t} \approx -\frac{j\omega\mu\alpha_0}{K_1^2} H_0 \left(\frac{L + T - z'}{T}\right) \cos\left(\frac{\pi x'}{a}\right) e^{-j\beta_0 z'}$$

$$E_{y_t} \approx -\frac{\omega\mu\beta_0}{K_1^2} H_0 \cos\left(\frac{\pi x'}{a}\right) e^{-j\beta_0 z'} \tag{3.44}$$

The induced magnetic field $\vec{H}_g$ on the ground plane y=0 is determined from equation (3.41) as

$$\vec{H}_g = \hat{x}\frac{j\omega\varepsilon}{2\pi}\left\{\int_{S_a} E_{z_a} G(R|R')ds_a' + \int_{S_t} E_{z_t} G(R|R')ds_t'\right\}$$

$$= \hat{x}\frac{k^2\alpha_0 H_0}{K_1^2}\left\{\int_{-\frac{w}{2}}^{\frac{w}{2}}\int_0^L \cos\left(\frac{\pi x'}{a}\right)\frac{e^{-jk\sqrt{(x-x')^2+(z-z')^2}}e^{-j\beta_0 z'}}{\sqrt{(x-x')^2+(z-z')^2}}dz'dx'\right.$$

$$\left. + \int_{-\frac{w}{2}}^{\frac{w}{2}}\int_L^{L+T}\left(\frac{L+T-z'}{T}\right)\cos\left(\frac{\pi x'}{a}\right)\frac{e^{-jk\sqrt{(x-x')^2+(z-z')^2}}e^{-j\beta_0 z'}}{\sqrt{(x-x')^2+(z-z')^2}}dz'dx'\right\} \tag{3.45}$$

The integral expression in equation (3.45) cannot be integrated in a closed form and the integration has to be carried out numerically. From the numerically calculated results, the calculation of the radiation fields result in an extremely complex computing problem. To side step such a computing difficulty and to obtain more physical insights on the

radiation fields, we will proceed the analysis with a less accurate but sufficiently correct induced field distribution on the ground plane. In the determination of the induced fields on the ground plane as a function of z, we will use the fields on the constant and tapered corrugated surfaces of infinite width to faciliate the closed form integration. Then, the actual fields on the ground plane are created from the fields calculated above multiplied by an appropriate function of x such as $\cos(\frac{\pi x}{a})$ or a unit step function of width W.

The aperture fields to be used for the determination of the induced fields on the ground plane are as follows:

On the constant corrugated surface,

$$E_{z_a} = -\frac{j\alpha_0}{\omega\varepsilon} H_0 e^{-j\beta_0 z'}$$

$$E_{y_a} = -\frac{\beta_0}{\omega\varepsilon} H_0 e^{-j\beta_0 z'} \qquad (3.46)$$

On the tapered corrugated surface,

$$E_{z_t} \approx -\frac{j\alpha_0}{\omega\varepsilon} \left(\frac{L + T - z'}{T}\right) H_0 e^{-j\beta_0 z'}$$

$$E_{y_t} \approx \frac{-\beta_0}{\omega\varepsilon} H_0 e^{-j\beta_0 z'} \qquad (3.47)$$

The induced magnetic field $\vec{H}_g$ on the ground plane can then be calculated as

$$\vec{H}_g = \hat{x}\ \frac{H_0\alpha_0}{2\pi}\left\{\int_{-\infty}^{\infty}\int_{0}^{L}\frac{e^{-jk\sqrt{(x-x')^2+(z-z')^2}}}{\sqrt{(x-x')^2+(z-z')^2}}\cdot e^{-j\beta_0 z'}\,dz'dx'\right.$$

$$\left.+\int_{\infty}^{\infty}\int_{L}^{L+T}\frac{(L+T-z')}{T}\,\frac{e^{-jk\sqrt{(x-x')^2+(z-z')^2}}}{\sqrt{(x-x')^2+(z-z')^2}}\cdot e^{-j\beta_0 z'}\,dz'dx'\right\}$$

$$= \hat{x}\left(\frac{-jH_0\alpha_0}{2}\right)\left\{\int_{0}^{T} H_0^2\,[k(z-z')]\,e^{-j\beta_0 z'}\,dz'\right.$$

$$\left.+\int_{L}^{L+T}\left(\frac{L+T-z'}{T}\right)H_0^2\,[k(z-z')]\,e^{-j\beta_0 z'}\,dz'\right\} \qquad (3.48)$$

In arriving at equation (3.48), the integral relationship for the second kind of Hanekl function of zeroth order, $H_0^2[k(z-z')]$,

$$\int_{\infty}^{\infty}\frac{e^{-jk\sqrt{(x-x')^2+(z-z')^2}}}{\sqrt{(x-x')^2+(z-z')^2}}\,dx' = -j\pi H_0^2\,[x(z-z')] \qquad (3.49)$$

was used. Equation (3.48) can be further simplified after introducing a new variable $u = k(z-z')$ as,

$$\vec{H}_g = \hat{x}\,\frac{-jH_0\alpha_0}{2}\,e^{-j\beta_0 z}\left\{\int_{kz}^{k(z-L)} H_0^2(u)\,e^{j\frac{\beta_0}{k}u}\,du + \right.$$

$$\left. + \frac{L+T-z}{T}\int_{k(z-L)}^{k(z-L-T)} H_0^2(u)\,e^{j\frac{\beta_0}{k}u}\,du\right. \qquad (3.50)$$

$$+ \frac{1}{kT} \int_{k(z-L)}^{k(z-L-T)} uH_0^2(u)\, e^{j\frac{\beta_0}{k}u}\, du \Bigg\} \tag{3.50}$$

In equation (3.50), the first term is due to the uniform corrugated surface field and the second and the third terms are due to the surface field on the tapered section. These integrals cannot be integrated in the closed forms, but if the argument of the Hankel function is greater than 3, the function may be expanded in an asymptotic form, which makes the integration possible in the closed forms. Fortunately, except for the limit points of the second and third integrals, the argument of the Hankel function is larger than 3. Thus, one may express the Hankel function with its asymptotic approximation as

$$H_0^2(u) \approx \sqrt{\frac{2}{\pi u}}\; e^{-ju + j\frac{\pi}{4}} \tag{3.51}$$

With equation (3.51), the induced field $\vec{H}_g$ in equation (3.50) can be rewritten as

$$\vec{H}_g = \hat{x}\left(-j\frac{H_0\alpha_0}{2k}\right) e^{-j\beta_0 z} \left[I_1 + \frac{L+T-z}{T}\, I_2 + \frac{1}{kd}\, I_3\right] \tag{3.52}$$

where

$$I_1 = \sqrt{\frac{2}{\pi}}\, e^{j\frac{\pi}{4}} \int_{kz}^{k(z-L)} \frac{e^{j\left(\frac{\beta}{k}-1\right)u}}{\sqrt{u}}\, du \tag{3.53}$$

$$I_2 = \sqrt{\frac{2}{\pi}}\, e^{j\frac{\pi}{4}} \int_{k(z-L)}^{k(z-L-T)} \frac{e^{j\left(\frac{\beta}{k}-1\right)u}}{\sqrt{u}}\, du \tag{3.54}$$

$$I_3 = \sqrt{\frac{2}{\pi}}\, e^{j\frac{\pi}{4}} \int_{k(z-L)}^{k(z-L-T)} \sqrt{u}\; e^{j(\frac{\beta}{k}-1)u}\, du \qquad (3.55)$$

These three integrals, I_1, I_2, I_3, can be integrated in closed forms in terms of Fresnel integrals with the introduction of a new variable,

$$\sqrt{\frac{\pi}{2}}\, v = \sqrt{(\frac{\beta_0}{k}-1)u}$$

The results of the integration are given by

$$I_1 = \frac{2e^{j\frac{\pi}{4}}}{\sqrt{\frac{\beta_0}{k}-1}} \Big[C(v) + j\, S(v) \Big]_{v_0}^{v_1}$$

$$I_2 = \frac{2e^{j\frac{\pi}{4}}}{\sqrt{\frac{\beta_0}{k}-1}} \Big[C(v) + j\, S(v) \Big]_{v_1}^{v_0} \qquad (3.56)$$

$$I_3 = \frac{1}{j(\frac{\beta_0}{k})-1} \left\{ \Big[\sqrt{\frac{2}{\pi}}\, e^{j\frac{\pi}{4}} \sqrt{u}\; e^{j(\frac{\beta_0}{k}-1)u} \Big]_{k(z-L)}^{k(z-L-T)} \right.$$

$$\left. - \frac{e^{j\frac{\pi}{4}}}{\sqrt{\frac{\beta_0}{k}-1}} \Big[C(v) + j\, S(v) \Big]_{v_1}^{v_2} \right\}$$

where

$$v_0 = \sqrt{\frac{2}{\pi}(\frac{\beta_0}{k}-1)kz}$$

$$v_1 = \sqrt{\frac{2}{\pi}(\frac{\beta_0}{k}-1)k(z-L)}$$

$$v_2 = \sqrt{\frac{2}{\pi}\left(\frac{\beta_0}{k} - 1\right)k(z-L-T)}$$

$$C(v) = \int_0^v \cos\left(\frac{\pi}{2} t^2\right)dt = \sum_{n=0}^{\infty} \frac{(-1)^n \left(\frac{\pi}{2}\right)^{2n}}{(2n)!\,(4n+1)} v^{4n+1}$$

$$S(v) = \int_0^v \sin\left(\frac{\pi}{2} t^2\right)dt = \sum_{n=0}^{\infty} \frac{(-1)^n \left(\frac{\pi}{2}\right)^{2n+1}}{(2n+1)!\,(4n+3)} v^{4n+3}$$

The induced magnetic field on the ground plane is then expressed by

$$\vec{H}_g = \hat{x}\, j\, H_0 \sqrt{\frac{\beta_0}{k} + 1}\; e^{j\frac{\pi}{4}}\; e^{-j\beta_0 z} \{\mathrm{Re}(I) + j\, \mathrm{Im}(I)\} \qquad (3.51)$$

where

$$\mathrm{Re}(I) = [C(v_0) - C(v_1)] + \frac{L+T-z}{T}[C(v_2) - C(v_1)]$$

$$- \frac{1}{2kT\left(\frac{\beta_0}{k} - 1\right)}[S(v_2) - S(v_1)]$$

$$+ \frac{1}{kT\sqrt{2\pi}\sqrt{\frac{\beta_0}{k} - 1}}\left(\sqrt{k_0(z-L-T)}\,\sin\left[\left(\frac{\beta_0}{k} - 1\right)k(z-L-T)\right]\right.$$

$$\left. - \sqrt{k(z-L)}\,\sin\left[\left(\frac{\beta_0}{k} - 1\right)k(z-L)\right]\right)$$

$$\mathrm{Im}(I) = [S(v_0) - S(v_1)] + \frac{L+T-z}{T}[S(v_2) - S(v_1)]$$

$$+ \frac{1}{2kT\left(\frac{\beta}{k} - 1\right)}[C(v_2) - C(v_1)]$$

$$- \frac{1}{2kT\sqrt{2\pi}\sqrt{\frac{\beta_0}{k}-1}} \left(\sqrt{k(z-L-T)}\cos\left[\left(\frac{\beta_0}{k}-1\right)k(z-L-T)\right] \right.$$

$$\left. - \sqrt{k(z-L)}\cos\left[\left(\frac{\beta_0}{k}-1\right)k(z-L)\right] \right)$$

In the computation of the induced field $\vec{H}_g$ on the ground plane, the direct numerical integration on equation (3.48) and the closed form computation in the asymptotic expansion of equation (3.57) were carried out for several different values of $\frac{\beta_0}{k}$ ratio for comparison. It turns out that the results from the approximate closed form deviate only slightly from those of the numerical integration. Figure 3.3 shows the distribution of the induced magnetic field computed based on the approximate closed form of equation (3.57). Figure 3.4 shows the results computed based on the numerical integration of equation (3.48). Comparing these two sets of results, the expression for $\vec{H}_g$ in the approximate closed form of equation (3.57) seems adequate for the radiation field calculation.

In order to see the contribution to $\vec{H}_g$ from the tapered section, the components of $\vec{H}_g$ which are maintained by the uniform corrugated surface and the tapered section were computed and compared in Figure 3.5. It is observed that the contribution from the tapered section is, indeed, quite small.

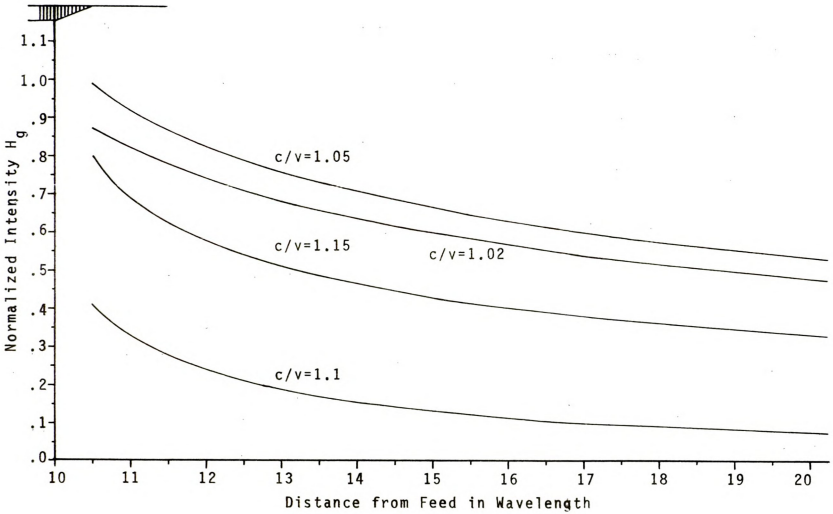

Figure 3.3 Induced H-Field Distribution on the Ground Plane by Large Argument Approximation

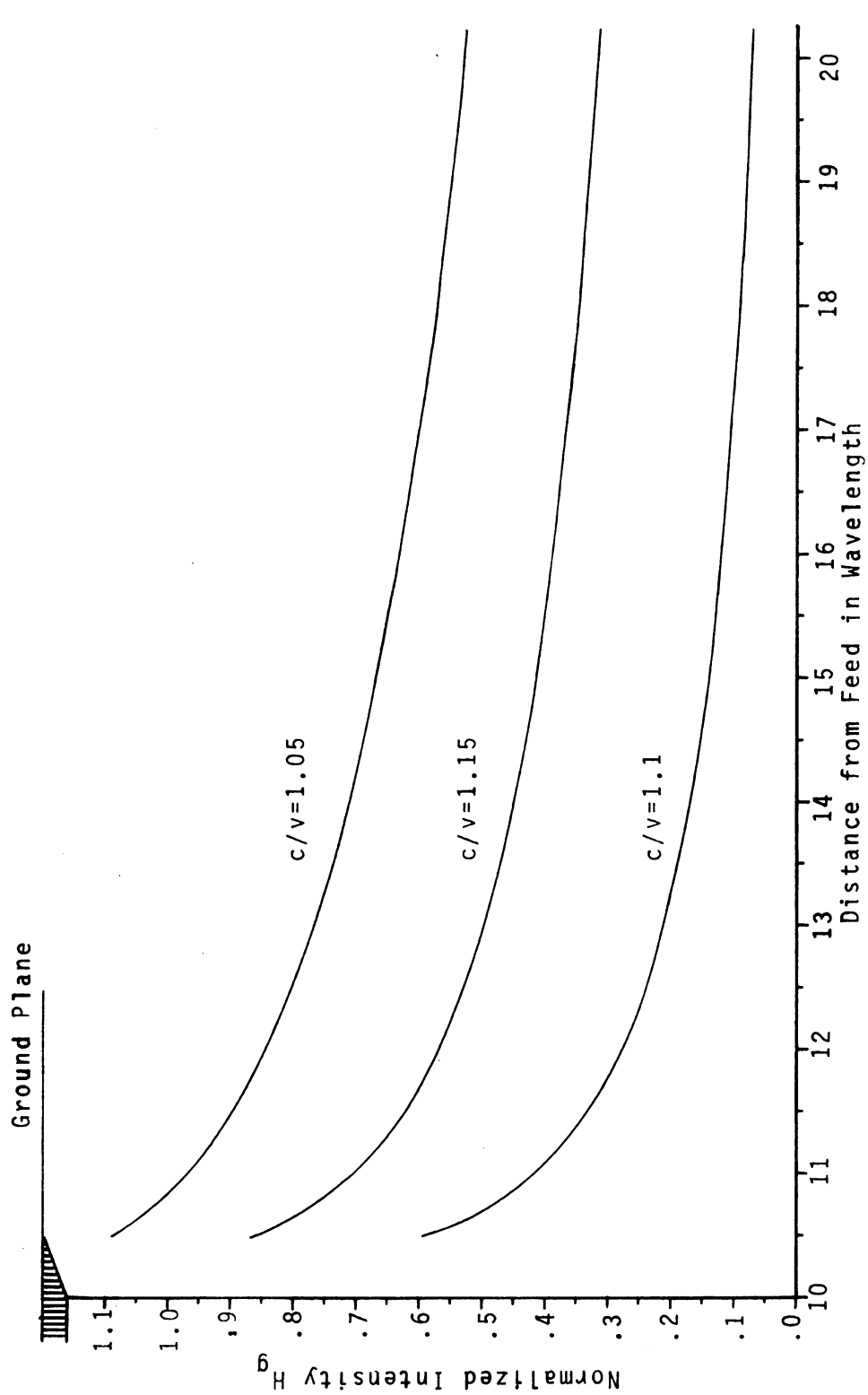

Figure 3.4 Induced H-Field Distribution on the Ground Plane by Numerical Integration

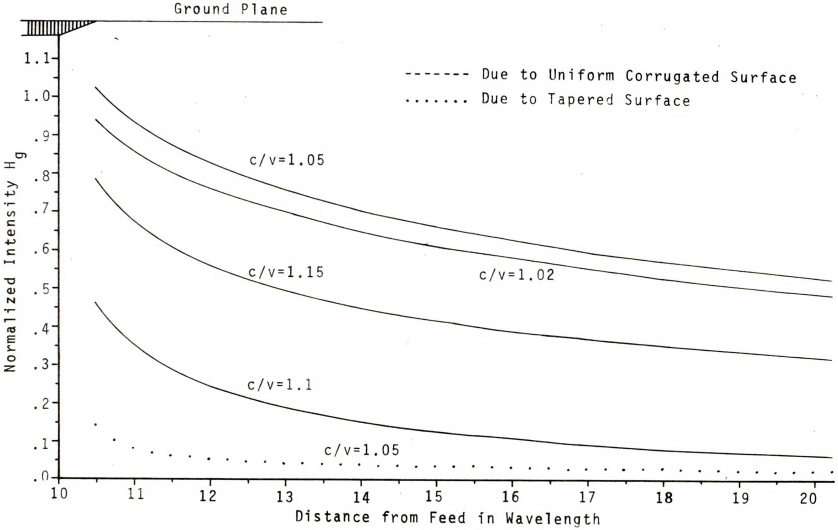

Figure 3.5 Induced H-Field Distribution on the Ground Plane Due to Constant Reactive Surface

CHAPTER IV

RADIATION FIELDS

The surface wave is a bounded wave propagating parallel to the guiding surface. Because of this boundness to the surface, it radiates only when it encounters the discontinuity on the guiding surface or when the surface is curved in the direction of propagation but not necessarily in the transverse direction. Because of this non-radiating nature, the ambiguity in the radiation field calculation has caused some controversy (43,62,63), but there are two well established distinctive methods, the feed and terminal approach and the aperture integration approach. These two approaches lead to an identical result within the approximations made in the course of calculation. In this study, the aperture integration method through Kirchhoff's vector integral formula will be employed.

4.1 Review of Radiation Field Calculation

In the calculation of the radiation patterns of slow surface wave structures, there has been some controversy because of its unusual non-radiating property. But two distinctive methods have been well established for the different structures of geometry and excitation. One is the feed and terminal pattern approach by solving the wave equation directly based on the view point of the discontinuity, and another is the aperture field integration method through the Kirchhoff's vector

integral or Kirchhoff-Huygens' integral formula.

The feed and terminal pattern method involves the direct approaches to the solution of the wave equation and is generally limited to the idealized structures such as a feed on the infinite or semi-infinite guiding structure. In this method, there are several approaches in solving the wave equation which give excellent analytical results on the radiation pattern as well as the surface wave excitation efficiency and the input impedance.

One of these approaches is the plane wave spectrum expansion method originated by Sommerfeld. In this approach, the exciting aperture fields are expanded in the longitudial spectral representation in terms of modes along the interface, with propagation normal to this interface or in the transverse spectral representation of modes, in the perpendicular cross section, with propagation along the interface. An excellent discussion on the subject is found in a paper by Booker and Clemmow (50). This method has been applied to the surface wave structures in several illuminating papers by Cullen (34), Tai (26), Whitmer (27) and Friedman and Williams (29).

The second interesting technique is also a direct approach to the solution of Maxwell's equations with the introduction of an auxiliary function. Since the surface wave structure must satisfy the mixed boundary conditions, the wave equation is not separable. To overcome this difficulty, an auxiliary function which is a linear combination of the magnetic or electric field and its derivative is chosen in such a way that it satisfies the wave equation and homogeneous boundary conditions. This technique was first demonstrated by Karp

and Karal (49). The well known Karp-Karal lemma on the surface wave radiation is based on this analysis.

In contrast to the above two techniques assuming the aperture field distribution, the third technique uses the wave mode incident to the exciting aperture through the connecting transmission line. Similar, to the mode matching technique, the formulation results in the integral equations, which can then be solved by Wiener-Hopf technique (71), leading to a reliable formulation on the input impedance as well as the excitation efficiency. This approach is mathematically rigorous but the applicable geometries are restricted to a few idealized structures, such as a parallel plate waveguide with a dielectric slab studied by Angulo and Chang (30), an infinitely wide corrugated structure excited by a parallel plate waveguide treated by Barlow and Brown (36) and a reactive impedance half plane problem investigated by Kane (46) by modifying Kay's discontinuity problem on the reactive impedance surface (45).

The aperture integration method has its own merits for being able to calculate the radiation from an aperture of arbitrary shape, while the feed and terminal pattern method is generally applicable only to the infinite or semi-infinite structures. Because of the non-radiating nature of the surface wave, the application of the aperture integration method has once raised some questions. But it can be proved that this method gives correct solutions as long as the aperture field distribution is correctly specified over the aperture. The validity of the aperture integral method applied to a surface wave radiation is examined in Appendix A. The early application of this method can be found in the papers by Mueller and Tyrrell (37) and Halliday and Kiely (38). Later,

this method was refined by Watson and Horton (39) and Horton et.al. (40) in the study of the dielectric rod antenna. Brown and Spector (41) also applied the terminal radiation concept to the aperture integration method.

In this study the radiation pattern of the antenna system will be calculated based on the aperture integration method. For the calculation of the radiation field, only the transverse aperture fields are important and the Kirchhoff's vector integral formula (3.38) and (3.39) reduce to

$$\vec{E}_p = \frac{1}{4\pi} \int_{S'} \left\{ (\hat{n} \times \vec{E}) \times \nabla' G - j\omega\mu (\hat{n} \times \vec{H}) G \right\} ds'$$

$$\vec{H}_p = \frac{1}{4\pi} \int_{S'} \left\{ (\hat{n} \times \vec{H}) \times \nabla' G + j\omega\varepsilon (\hat{n} \times \vec{E}) G \right\} ds' \qquad (4.1)$$

where G is the free space three dimensional Green's function defined by $G = e^{-jkR}/R$ and the primes in equation (4.1) indicate the operation on the source coordinates.

The formula in equation (4.1) may be further simplified by the usual far-field approximation with the coordinate system shown in Figure 4.1.

$$R \approx r - \hat{r} \cdot \vec{r}'$$

$$\hat{R} = \frac{\vec{R}}{R} \approx \hat{r} \qquad (4.2)$$

$$\nabla' G = -\nabla G \approx jk \frac{e^{-jk(r - \hat{r} \cdot \vec{r}')}}{r} \hat{r}$$

With these approximations, the electric field (E_p) in the far-zone can be expressed as

$$\vec{E}_p = \frac{e^{-jkr}}{4\pi r} \int \left\{ jk(\hat{n} \times \vec{E}) \times \hat{r} - j\omega\mu (\hat{n} \times \vec{H}) \right\} e^{jk\hat{r}\cdot\vec{r}'} ds' \tag{4.3}$$

where the surface of integration S' includes the guiding surface, the ground plane and the feed aperture if the feed radiation cannot be neglected.

4.2 Radiation Fields of a Single Corrugated Structure

The radiation fields maintained by a single corrugated surface wave structure on a finite ground plane will be calculated by the Kirchhoff's vector integral formula (4.3) with the assumption of negligible feed radiation. The geometry of the single corrugated surface antenna system is shown in Figure 4.1.

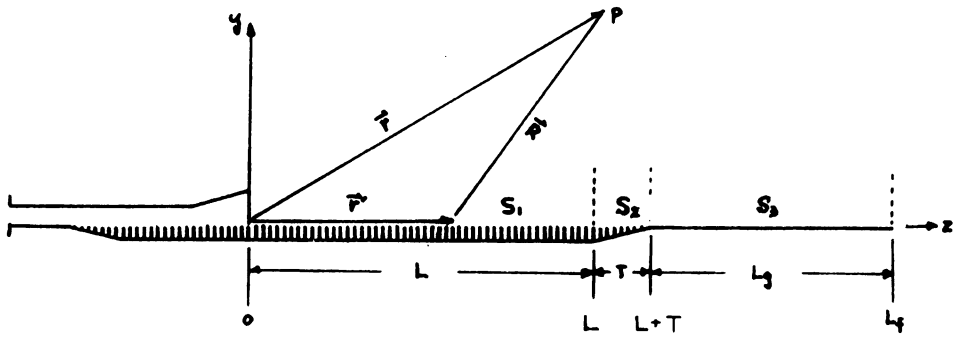

Figure 4.1 Coordinates of Corrugated Antenna for Radiation Fields

In application of equation (4.3), the surfaces to be integrated are S_1, S_2 and S_3. The tangential fields on these surfaces are given from equation (3.7), (3.37) and (3.57) as follows:

On S_1;

$$E_{z_1} = \frac{-j\omega\mu\alpha_0}{K_1^2} H_0 \cos(\frac{\pi x}{w}) e^{-j\beta_0 z}$$

$$H_{x_1} = H_0 \cos(\frac{\pi x}{w}) e^{-j\beta_0 z} \qquad (4.4a)$$

$$H_{z_1} = \frac{j\beta_0 \frac{\pi}{a}}{K_1^2} H_0 \sin(\frac{\pi x}{w}) e^{-j\beta_0 z}$$

On S_2;

$$E_{z_2} \approx \frac{-j\omega\mu\alpha_0}{K_1^2} H_0(\frac{L+T-z}{T}) \cos(\frac{\pi x}{w}) e^{-j\beta_0 z}$$

$$H_{x_2} \approx H_0 \cos(\frac{\pi x}{w}) e^{-j\beta_0 z} \qquad (4.4b)$$

$$H_{z_2} \approx 0$$

On S_3;

$$H_{x_g} = jH_0 \sqrt{\frac{\beta_0}{k} + 1} \quad f(x) e^{j\frac{\pi}{4}} e^{-j\beta_0 z} \{Re(I) + j\ Im(I)\} \qquad (4.4c)$$

where Re(I) and Im(I) are defined in equation (3.57). The function f(x) is an approximate transverse distribution function such as $\cos(\frac{\pi x}{w})$ or a step function with a width of W.

With these aperture fields and using the coordinate system shown in Figure 4.1, the far-zone electric field in spherical coordinates can be expressed as follows:

For θ component;

$$E_\theta = -\frac{e^{-jkr}}{4\pi r}\left\{jk \sin\phi \int_{S_1+S_2} E_z\, e^{jk(x'\sin\theta\cos\phi + z'\cos\theta)}dx'dz' + j\omega\mu \int_{S_1+S_2+S_3} (H_x\sin\theta + H_z\cos\theta\cos\phi)e^{-jk(x'\sin\theta\cos\phi + z'\cos\theta)}dx'dz'\right\} \quad (4.5)$$

For φ component;

$$E_\phi = -\frac{e^{-jkr}}{4\pi r}\left\{jk\cos\theta\cos\phi \int_{S_1+S_2} E_z\, e^{jk(x'\sin\theta\cos\phi + z'\cos\theta)}dx'dz' - j\omega\mu\sin\phi \int_{S_1} H_z e^{jk(x'\sin\theta\cos\phi + z'\cos\theta)}dx'dz'\right\} \quad (4.6)$$

where E_z, H_x and H_z are the tangential aperture fields given in equation (4.4).

In plotting the radiation fields, only the principal plane radiation patterns are considered here. The E-plane pattern ($\phi=\frac{\pi}{2}$, in y-z plane) and the H-plane pattern ($\phi=0$, in x-z plane) will be calculated separately in the following sections.

4.2.1 E-Plane Radiation Pattern

With $\phi = \frac{\pi}{2}$ in equation (4.5), the E-plane radiation field, $E_\theta(\phi = \frac{\pi}{2})$ is expressed by

$$E_\theta(\phi = \frac{\pi}{2}) = - \frac{e^{-jkr}}{4\pi r} \left\{ jk \int_{S_1+S_2} E_z e^{jkz'\cos\theta} dz' \right.$$

$$\left. + j\omega\mu \sin\theta \int_{S_1+S_2+S_3} H_x e^{jkz'\cos\theta} dz' \right\} \qquad (4.7)$$

Substituting E_z and H_x given by equation (4.4) in equation (4.7) and integrating over x dimension for $-\frac{w}{2}$ to $\frac{w}{2}$ yields

$$E_\theta(\phi= \frac{\pi}{2}) = - \frac{e^{-jkr}}{4\pi r} \left\{ E_1(\theta) + E_2(\theta) + E_3(\theta) \right\} \qquad (4.8)$$

where $E_1(\theta)$, $E_2(\theta)$ and $E_3(\theta)$ are the radiation pattern functions produced by the uniformly corrugated surface, the tapered surface and the ground plane respectively. Each pattern function is expressed as follows:

$$E_1(\theta) = \frac{2wkH_0}{\pi\omega\epsilon} \left(\frac{k^2\alpha_0}{K_1^2} + jk \sin\theta \right) \int_0^L e^{-jk(\frac{\beta_0}{k} - \cos\theta)z'} dz'$$

$$= \frac{2WkH_0}{\pi\omega\varepsilon}\left(\frac{k^2\alpha_0}{K_1^2} + jk\sin\theta\right) L \frac{\sin[\frac{kL}{2}(\frac{\beta_0}{k} - \cos\theta)]}{\frac{kL}{2}(\frac{\beta_0}{k} - \cos\theta)} \tag{4.8a}$$

$$E_2(\theta) = \frac{2WkH_0}{\pi\omega\varepsilon}\int_L^{L+T}\left(\frac{k^2\alpha}{K_1^2}\frac{L+T-z'}{T} + jk\sin\theta\right)e^{-j(\frac{\beta_0}{k} - \cos\theta)z'}dz'$$

$$= \frac{2WkH_0}{\pi\omega\varepsilon}\left\{\frac{k^2 L}{K_1^2}\cdot\frac{e^{-jk(\frac{\beta_0}{k} - \cos\theta)}}{kL(\frac{\beta_0}{k} - \cos\theta)}\left[-1+\frac{\sin[\frac{kT}{2}(\frac{\beta_0}{k} - \cos\theta)}{\frac{kT}{2}(\frac{\beta_0}{k} - \cos\theta)}\right.\right.$$

$$\left.\left.e^{-j\frac{kT}{2}(\frac{\beta_0}{k} - \cos\theta)}\right] + jkT\sin\theta\frac{\sin[\frac{kT}{2}(\frac{\beta_0}{k} - \cos\theta)}{\frac{kT}{2}(\frac{\beta_0}{k} - \cos\theta)}\right\} \tag{4.8b}$$

$$E_3(\theta) = j\,W\,\omega\mu\sin\theta\int_{L+T}^{L_f} H_g\, e^{jk\cos\theta\, z'}\, dz'$$

$$= -\frac{WkH_0}{\omega\varepsilon}\sin\theta\sqrt{\frac{\beta_0}{k} + 1}\; e^{j\frac{\pi}{4}}\, k\{I\} \tag{4.8c}$$

where

$$\{I\} = (I_1 - jI_2) + (I_3 - jI_4) + (I_5 + jI_6) - I_7 + I_8 \tag{4.9}$$

Each I_n(n=1,2, ...6) cannot be integrated in a closed form. Thus, they are given in the integral forms as follows:

$$I_1 - jI_2 = \int_{L+T}^{L_f} \left\{C(v_1)-C(v_0) + j[S(v_1)-S(v_0)]\right\} e^{-jk(\frac{\beta_0}{k} -\cos\theta)z'} dz' \tag{4.9a}$$

$$I_3 - jI_4 = \int_{L+T}^{L_f} \frac{L+T-z'}{T} \left\{C(v_2)-C(v_1)+j[S(v_2)-S(v_1)]\right\} e^{-jk(\frac{\beta_0}{k} -\cos\theta)z'} dz' \tag{4.9b}$$

$$I_5+jI_6 = \frac{1}{2kT(\frac{\beta_0}{k} -1)} \int_{L+T}^{L_f} \left\{C(v_2)-C(v_1)+j[S(v_2)-S(v_1)]\right\} e^{-jk(\frac{\beta_0}{k} -\cos\theta)z'} dz' \tag{4.9c}$$

$$I_7 = \frac{e^{-jk(L+T)(\frac{\beta_0}{k} -\cos\theta)}}{k^2T\sqrt{2\pi}\sqrt{\frac{\beta_0}{k} -1}\ (1-\cos\theta)} \left\{- \sqrt{k(L_f-L-T)}\ e^{-j(1-\cos\theta)k(L_f-L-T)} \right.$$

$$\left. + \frac{\sqrt{2\pi}}{2\sqrt{1-\cos\theta}} [C(v_3) - jS(v_3)]\right\}$$

$$I_8 = \frac{-e^{-jkL(\frac{\beta_0}{k} -\cos\theta)}}{k^2T\sqrt{2\pi}\sqrt{\frac{\beta_0}{k} -1}\ (1-\cos\theta)} \left\{\sqrt{k(L_f-L)}\ e^{-j(1-\cos\theta)k(L_f-L)} \right.$$

$$\left. - \sqrt{kT}\ e^{-j(1-\cos\theta)kT} - \frac{\sqrt{2\pi}}{2\sqrt{1-\cos\theta}} [C(v_5)-C(v_4)-j(S(v_5)-S(v_4))]\right\} \tag{4.9d}$$

where C(v) and S(v) are the cosine and the sine integrals respectively. Their arguments, v's are defined as

$$v_0 = \sqrt{\frac{2}{\pi}\left(\frac{\beta_0}{k} - 1\right)kz'}$$

$$v_1 = \sqrt{\frac{2}{\pi}\left(\frac{\beta_0}{k} - 1\right)k(z'-L)}$$

$$v_2 = \sqrt{\frac{2}{\pi}\left(\frac{\beta_0}{k} - 1\right)k(z'-L-T)}$$

$$v_3 = \sqrt{\frac{2}{\pi}(1-\cos\theta)k(L_f-L-T)}$$

$$v_4 = \sqrt{\frac{2}{\pi}(1-\cos\theta)kT}$$

$$v_5 = \sqrt{\frac{2}{\pi}(1-\cos\theta)k(L_f-L)}$$

For the computational convenience, the E-plane pattern function $E_\theta(\phi=\frac{\pi}{2})$ is rearranged as follows:

$$E_0\left(\phi = \frac{\pi}{2}\right) = \frac{2W}{\pi}\left(\frac{kH_0}{\omega\varepsilon}\right)\{E_1(\theta) + E_2(\theta) + E_3(\theta)\} \tag{4.10}$$

$$E_1(\theta) = \left[\cos A \cdot \sqrt{\left(\frac{\beta_0}{k}\right)^2 - 1} + \sin A \sin\theta\right] kL \frac{\sin A}{A}$$

$$+ j\left[-\sin A \cdot \sqrt{\left(\frac{\beta_0}{k}\right)^2 - 1} + \cos A \sin\theta\right] kL \frac{\sin A}{A} \tag{4.10a}$$

$$E_2(\theta) = \frac{kL}{2A}\sqrt{\left(\frac{\beta_0}{k}\right)^2 - 1}\left[\sin(2A+B)\frac{\sin B}{B} - \sin 2A\right]$$

$$+ kd \sin\theta \sin(2A+B)\frac{\sin B}{B}$$

$$+ j\left\{\frac{kL}{2A}\sqrt{\left(\frac{\beta_0}{k}\right)^2 - 1}\left[\cos(2A+B)\frac{\sin B}{B} - \cos 2A\right]\right.$$

$$\left. + kd \sin\theta \cos(2A+B)\frac{\sin B}{B}\right\} \tag{4.10b}$$

$$E_3(\theta) = -\sqrt{\frac{\beta_0}{k} + 1}\ \sin\theta$$

$$\cdot \{\cos\tfrac{\pi}{4}[k(I_1+I_3+I_5) + k(\mathrm{Re}\ I_8 - \mathrm{Re}\ I_7)]$$

$$+ \sin\tfrac{\pi}{4}[k(I_2+I_4-I_6) - k(\mathrm{Im}\ I_8 - \mathrm{Im}\ I_7)]$$

$$+ j \sin\tfrac{\pi}{4}[k(I_1+I_3+I_5) + k(\mathrm{Re}\ I_8 - \mathrm{Re}\ I_7)]$$

$$- j \cos\tfrac{\pi}{4}[k(I_2+I_4-I_6) - k(\mathrm{Im}\ I_8 - \mathrm{Im}\ I_7)]\} \qquad (4.10c)$$

where

$$\mathrm{Re}I_7 = \frac{1}{k^2 T\sqrt{2\pi}\sqrt{\frac{\beta_0}{k} - 1}\ (1-\cos\theta)}$$

$$\cdot \left\{ \cos C\left[-\sqrt{k(L_f-L-T)}\cos D + \frac{\sqrt{2\pi}\ C(v_3)}{2\sqrt{1-\cos\theta}}\right]\right.$$

$$\left. + \sin C\left[\sqrt{k(L_f-L-T)}\sin D - \frac{\sqrt{2\pi}\ S(v_3)}{2\sqrt{1-\cos\theta}}\right]\right\} \qquad (4.10d)$$

$$\mathrm{Im}I_7 = \frac{1}{k^2 T\sqrt{2\pi}\sqrt{\frac{\beta_0}{k} - 1}\ (1-\cos\theta)}$$

$$\cdot \left\{ -\sin C\left[-\sqrt{k(L_f-L-T)}\cos D + \frac{\sqrt{2\pi}\ C(v_3)}{2\sqrt{1-\cos\theta}}\right]\right.$$

$$\left. + \cos C\left[\sqrt{k(L_f-L-T)}\sin D - \frac{\sqrt{2\pi}\ S(v_3)}{2\sqrt{1-\cos\theta}}\right]\right\} \qquad (4.10e)$$

$$\mathrm{Re}I_8 = \frac{1}{k^2 T\sqrt{2\pi}\sqrt{\frac{\beta_0}{k} - 1}\ (1-\cos\theta)}$$

$$\cdot\left\{-\cos G\left[\sqrt{k(L_f-L)}\cos E - \sqrt{kT}\cos F - \right.\right.$$

$$\left. - \frac{\sqrt{2\pi}}{2\sqrt{1-\cos\theta}}\left(C(v_5) - C(v_4)\right)\right]$$

$$+ \sin G\left[\sqrt{k(L_f-L)}\sin E - \sqrt{kT}\sin F\right.$$

$$\left.\left. - \frac{\sqrt{2\pi}}{2\sqrt{1-\cos\theta}}\left(S(v_5) - S(v_4)\right)\right]\right\} \qquad (4.10f)$$

$$\mathrm{Im}I_8 = \frac{1}{k^2T\sqrt{2\pi}\sqrt{\frac{\beta_0}{k} - 1}\ (1-\cos\theta)}$$

$$\cdot\left\{\sin G\left[\sqrt{k(L_f-L)}\cos E - \sqrt{kT}\cos F\right.\right.$$

$$\left. - \frac{\sqrt{2\pi}}{2\sqrt{1-\cos\theta}}\left(C(v_5) - C(v_4)\right)\right]$$

$$+ \cos G\left[\sqrt{k(L_f-L)}\sin E - \sqrt{kT}\sin F\right.$$

$$\left.\left. - \frac{\sqrt{2\pi}}{2\sqrt{1-\cos\theta}}\left(S(v_5) - S(v_4)\right)\right]\right\} \qquad (4.10g)$$

where

$$A = \frac{kL}{2}\left(\frac{\beta_0}{k} - \cos\theta\right)$$

$$B = \frac{kT}{2}\left(\frac{\beta_0}{k} - \cos\theta\right)$$

$$C = k(L+T)\left(\frac{\beta_0}{k} - \cos\theta\right)$$

$$D = k(L_f-L-T)(1 - \cos\theta)$$

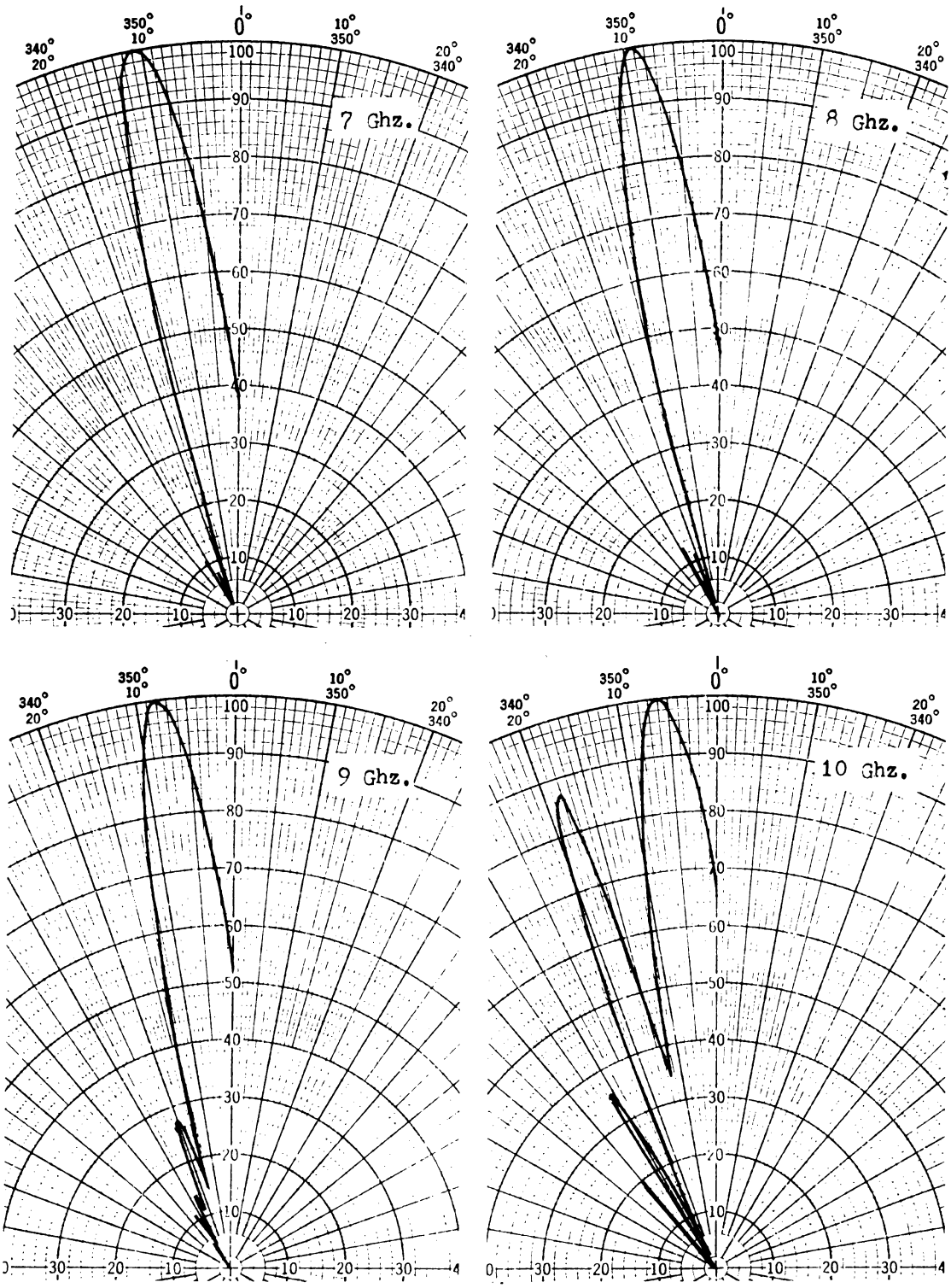

Figure 4.2 Calculated E-Plane Radiation Power Patterns (7-10 Ghz.)

$$E = k(L_f - L)(1 - \cos\theta)$$

$$F = kT(1 - \cos\theta)$$

$$G = 2A$$

In the E-plane, there is a low intensity of $E_\phi(\phi = \frac{\pi}{2})$ component which is due to the H_z component on the corrugated surface. The magnitude of H_z component is negligible compared to E_z component when the width of the corrugated surface is several wavelengths. Thus, the actual E-plane pattern corresponds to the $E_\theta(\phi = \frac{\pi}{2})$ field. The E-plane radiation patterns for various measured values of $\frac{\beta_0}{k}$ ratio have been computed for the frequencies ranging from 7 Ghz. to 10 Ghz. and they are plotted in Figure 4.2.

In all these results for the E-plane patterns, the directivity remains quite high and the side lobe levels stay very low for a wide range of frequencies. The inevitable beam tilt due to the finite ground plane is observable for all frequencies.

4.2.2 H-Plane Radiation Pattern

With $\phi = 0$ in equation (4.6), the H-plane radiation field, $E(\phi=0)$ can be obtained as

$$E_\phi(\phi=0) = -\frac{e^{-jkr}}{4\pi r}\, jk\cos\theta \int_{S_1+S_2} E_z\, e^{jk(x'\sin\theta + z'\cos\theta)} \qquad (4.11)$$

Substituting the tangential electric component E_z given in equation (4.4) in equation (4.11), the $E_\phi(\phi=0)$ becomes

$$E_\phi(\phi=0) = -\frac{e^{-jkr}}{4\pi r}\ \{H_1(\theta) + H_2(\theta)\} \tag{4.12}$$

where $H_1(\theta)$ and $H_2(\theta)$ are the H-plane radiation pattern functions produced by the uniform corrugated surface and the tapered surface respectively. Note that the induced current on the ground plane does not contribute to E_ϕ in the H-plane pattern. The pattern functions are expressed as

$$H_1(\theta) = jk\cos\theta \int_{-\frac{W}{2}}^{\frac{W}{2}} \int_0^L \frac{-j\omega\mu\alpha_0 H_0}{K_1^2} \cos\frac{\pi x'}{W}\, e^{jkx'\sin\theta} \cdot e^{-jk(\frac{\beta_0}{k} - \cos\theta)z'} dz'dx'$$

$$H_1(\theta) = \frac{2Wk^3 H_0}{\pi\omega\varepsilon K_1^2} \left\{\cos\theta \cdot \frac{\cos(\frac{kW}{2}\sin\theta)}{1 - (\frac{kW}{\pi}\sin\theta)^2} \cdot e^{-j\frac{kL}{2}(\frac{\beta_0}{k} - \cos\theta)} \cdot \frac{\alpha_0 L \sin[\frac{kL}{2}(\frac{\beta_0}{k} - \cos\theta)]}{\frac{kL}{2}(\frac{\beta_0}{k} - \cos\theta)}\right\} \tag{4.12a}$$

$$H_2(\theta) = jk\cos\theta \int_{-\frac{W}{2}}^{\frac{W}{2}} \int_L^{L+T} \frac{-j\omega\mu\alpha_0 H_0}{K_1^2} (\frac{L+T-z'}{T}) \cos(\frac{\pi x'}{W}) e^{jkx'\sin\theta} \cdot e^{-jk(\frac{\beta_0}{k} - \cos\theta)z'} dz'dx'$$

$$= \frac{2Wk^3 H_0}{\pi\omega\varepsilon K_1^2} \left\{\cos\theta \cdot \frac{\cos(\frac{kW}{2}\sin\theta)}{1 - (\frac{kW}{\pi}\sin\theta)^2} \cdot \frac{j\,Le^{-jkL(\frac{\beta_0}{k} - \cos\theta)}}{kL(\frac{\beta_0}{k} - \cos\theta)}\right.$$

$$\cdot \left[-1 + \frac{\sin \frac{kT}{2}(\frac{\beta_0}{k} - \cos\theta)}{\frac{kT}{2}(\frac{\beta_0}{k} - \cos\theta)} \; e^{-j\frac{kT}{2}(\frac{\beta_0}{k} - \cos\theta)} \right] \Bigg\} \quad (4.12b)$$

For the computational convenience, the H-plane pattern function $E_\phi(\phi=0)$ is rearranged by replacing $K_1 = \sqrt{k^2 - (\frac{\pi}{a})^2}$ with k, which is reasonable approximation for a wide corrugated surface, as follows:

$$E_\phi(\phi=0) = (\frac{2W}{\pi}) \; (\frac{kH_0}{\omega\epsilon}) \; \{H_1(\theta) + H_2(\theta)\} \quad (4.13)$$

$$H_1(\theta) = \cos\theta \; \frac{\cos u}{1-u^2} \; \frac{\sin A}{A} \; \alpha_0 L(\cos A - j \sin A) \quad (4.13a)$$

$$H_2(\theta) = \cos\theta \; \frac{\cos u}{1-u^2} \; \Bigg\{ \frac{\alpha_0 L}{2A} \left[\frac{\sin B}{B} \; \sin(2A+B) - \sin 2A \right]$$

$$+ j \frac{\alpha_0 L}{2A} \left[\frac{\sin B}{B} \cos(2A+B) - \cos 2A \right] \Bigg\} \quad (4.13b)$$

where

$$u = \frac{kW}{\pi} \sin\theta$$

The H-plane radiation patterns for various measured values of $\frac{\beta_0}{k}$ ratio have been computed for the frequencies ranging from 7 Ghz. to 10 Ghz. and they are plotted in Figure 4.3. It is noted that the half power beam width varies with the frequency and the very low side lobe levels for all frequencies have been obtained.

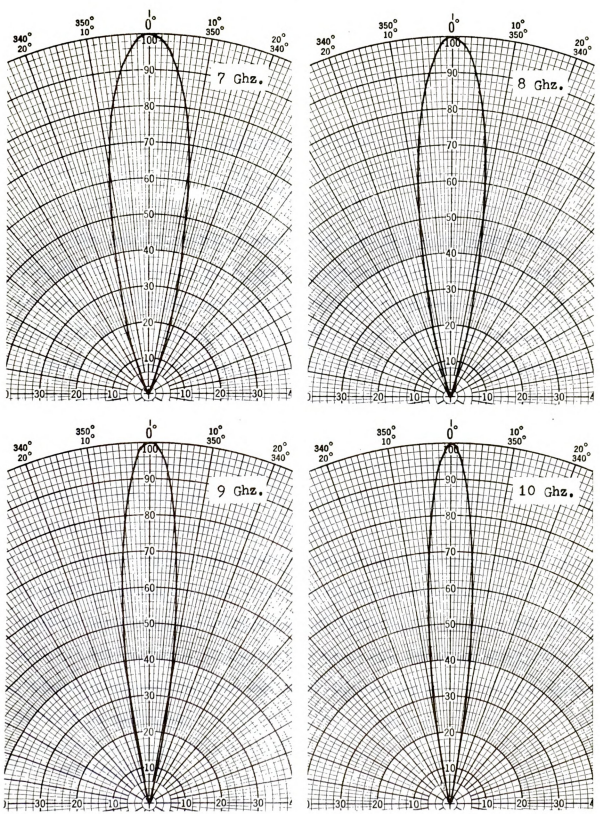

Figure 4.3 Calculated H-Plane Radiation Power Patterns (7-10 Ghz.)

CHAPTER V

EXPERIMENT

The exact theoretical analysis of the flat corrugated surface with finite dimensions as an end-fire antenna is not known to exist because of its complex geometry and boundary conditions. The characteristics of the antenna were determined by an approximate analysis retaining only the fundamental harmonic of the infinite space harmonics of the surface wave and assuming 100 percent launching efficiency. For this reason, an experimental study of the antenna becomes essential to determine the surface wave transmission and radiating properties of a practical antenna and to verify the accuracy of the approximate analysis developed in the preceding chapters.

In this chapter, an extensive experimental investigation on the waveguide excitation of the surface wave, the surface field distributions on the corrugated surface and the finite ground plane, the boundness and the phase velocity of the surface wave, the radiation properties of a single corrugated radiator and the beam scanning of a composite radiator will be described.

5.1 Antenna System

The experimental model of a surface wave antenna consists of four major parts: a rectangular waveguide for the TE_{10} mode excitation, a rectangular waveguide with corrugated bottom wall for the hybrid slow

wave, a transition horn for the hybrid slow wave to the slow surface wave, and a flat corrugated surface on a finite ground plane as shown in Figure 5.1.

In order to improve the surface wave excitation on the open corrugated conducting surface, the top and side walls of the corrugated rectangular waveguide was gradually flared out to match the aperture impedance. The corrugated bottom wall was extended to form an open corrugated guiding surface. The physical dimensions of the open corrugated guiding structure were chosen to support a slow surface wave with phase constant ratio of $\frac{\beta_0}{k} = 1.05$ at 9 Ghz. and to produce an optimum end-fire beam over an infinitely large ground plane.

The dimensions of corrugation were determined from the approximate dispersion relation for the infinitely wide corrugated surface,

$$\cot(kh) = \frac{d}{D} \sqrt{\left(\frac{\beta_0}{k}\right)^2 - 1} \qquad (5.1)$$

where k is the free space propagation constant, β_0 is the phase constant of the fundamental harmonic, h is the corrugation height, d is the corrugation gap width and D is the physical length of one corrugation cell. The accuracy of this formula in equation (5.1) increases as the number of corrugations per wave length (N) increases, since equation (5.1) is derived based on the average impedance concept. It is known that the accuracy is adequate if $N > 20$ (56).

The maximum gain condition for an end-fire radiation from travelling wave antenna is known as the Hansen-Woodyard relation. This states that for antennas producing the radiation pattern of type

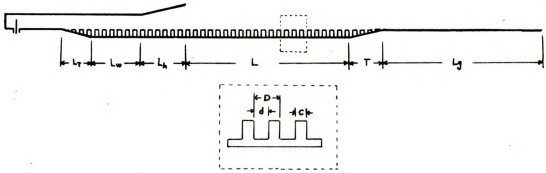

(a) Single Radiator

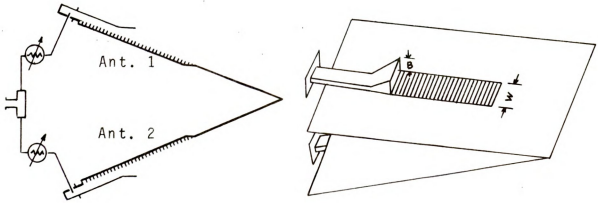

(b) Composite Radiator

Figure 5.1 Corrugated Antenna

$\sin[\frac{L}{2}(\beta_0 - k \sin\theta)] / \frac{L}{2}(\beta_0 - k \sin\theta)$, the end-fire directivity is maximum if

$$\frac{\pi}{2} \leq (\beta_0 - k) L \leq \pi \tag{5.2}$$

where L is the length of the guiding surface. In general, if the excitation efficiency of the slow wave at the aperture is low, the guiding surface should be made long to avoid the interaction between the quasi-near field of feed and the surface wave at the end of the guiding surface. Thus, the right hand side limit of equation (5.2), π, may be more appropriate for the practical antennas. This optimum condition was also proved by Kane (46) in a theoretical study of an idealized surface wave antenna.

Using the relations of equation (5.1) and equation (5.2), the actual dimensions of the corrugated structure supporting the slow surface wave of $\frac{\beta_0}{k} = 1.05$ were found to be

d = 0.025 in.	h = 0.1091 in.
c = 0.02 in.	L = 13.12 in. (10 λ_0 at 9 Ghz.)
D = 0.045 in.	W = 2.62 in. (2 λ_0 at 9 Ghz.)

For a good impedance match between the corrugated surface and the ground plane, the end part of the corrugated surface was linearly tapered up to zero height at the junction with the ground plane. Since it is not possible to determine the optimum dimensions for the tapered section, the length of the tapered section (T) was initially chosen to be T = 0.656 in. long (0.5 λ_0 at 9 Ghz.).

For the efficient slow surface wave excitation on the open corrugated surface, a part of the bottom wall of a standard rectangular waveguide, WR 90, was corrugated with the same dimensions as those of the open corrugated surface. The actual dimensions of the guide are L_w = 6.545 in. long, A = 0.9 in. wide and B = 0.4 in. high. The corrugations near the junction with the uniform rectangular waveguide were also tapered up to zero height at the junction for the smooth transition from the TE_{10} to the hybrid slow wave in the corrugated guide.

In order to achieve a good impedance match and a smooth transition from the hybrid slow wave in the corrugated guide to the TM slow surface wave on the open corrugated surface, the corrugated guide was gradually flared out to produce the same phase velocity at the aperture as that of the open corrugated surface and to have small phase variation across the aperture plane. The horn dimensions were chosen to be

L_h = 6.545 in. long

W = 2.62 in. wide

B = 2.0 in. high

With these dimensions, the maximum phase variation in E and H plane across the horn aperture is 0.0383 λ_0 at the center frequency of 9 Ghz.

The corrugated surface was mounted on a ground plane of 10 λ_0 x 10 λ_0 at 9 Ghz to form a complete single corrugated antenna.

For the beam scanning experiment, two identical corrugated antennas were constructed. The two antennas were placed on the opposite sides of the wedge shape ground plane as shown in Figure 5.1b. The wedge half angle can be varied within the range of the beam tilt angel of the single

corrugated antenna. The wedge angle determines the maximum scanning angle about the axis of the composit antenna system.

5.2 Surface Field Distribution

For the investigation of the surface field distribution on the antenna surface, the conventional square-law detector system was used with simple probes (66,67) because of the equipment availability, even though the back scattering technique with a heterodyne detection system (64,69) may give better results for the amplitude and phase measurements in the microwave frequency range.

The electric and magnetic field strengths were measured with the simple electric and magnetic probes (65,68). The probes were made of 50 ohm teflon filled mini-coaxial cable of 0.08 in. outer diameter. The outer conductor was coated with a lossy dielectric material (Eccosorb CR-117) and covered partly with a sheet of microwave absorber to reduce the scattering from the probe lead. Figure 5.2 shows the rough sketch of the probes.

For the electric field probe, the inner conductor of the coaxial line was extended out 0.18 inch long (0.158 λ_0 at 9 Ghz.) as the detecting element. The probe length should be made as short as possible to reduce the disturbance of the original field distribution on the antenna surface. However, because of very high loss in the mini coaxial line and the low sensitive detecting equipment, the probe element was made somewhat longer than it should be. To check the seriousness of the field disturbance by the rather long probe, the field amplitude distribution was measured along different heights and the reflected waves were monitored at the input of

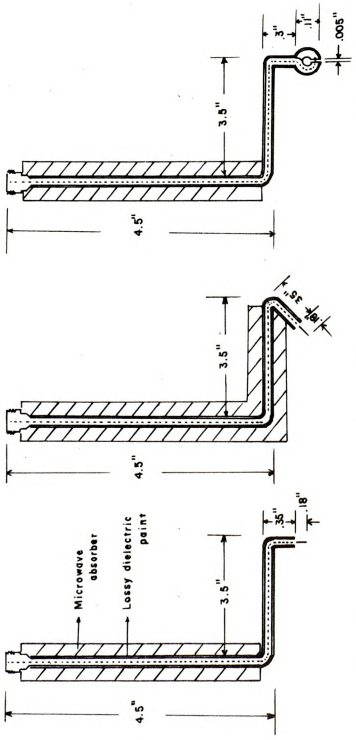

Figure 5.2 Probe Assemblies

the antenna using a 20 db directional coupler for different lengths of the probe element. It was found that the probe element of a length of 0.18 inch yields entirely satisfactory measurement accuracy.

For the measurement of the magnetic field distribution, a probe was shaped as a circular loop with the outer diameter of 0.11 inch, the inner diameter 0.03 inch and the gap spacing of 0.005 inch as shown in Figure 5.2. The gap spacing was deliberately made small to reduce the sensitivity for the E_z component which appears on the corrugated surface in addition to the H_x component. Since a single loop probe detects both the H_x and E_z components simultaneously, the measured field pattern is not the pure distribution of the magnetic field H_x but rather a mixed distribution containing a small E_z component on the corrugated surface. On the ground plane, however, the field pattern measured by the single loop probe is the true distribution of the induced magnetic field H_g. The H_x and E_z components can be detected separately by means of a double loop probe, but since the relative amplitude of the E_z field on the corrugated surface is much smaller than that of the H_x field on the surface, the single loop probe with very small gap spacing was chosen for the measurement.

As shown in Figure 5.2, each probe has a long lead which is properly shaped to reduce the induced current on its outer conductor. The probe was connected to a probe holder by a miniature coaxial connector. The probe holder was designed in such a way that the probe can be moved freely vertically and that the probe can be set at any specific height above the antenna surface. For the continuous recording, the probe holder was mounted to a d.c. motor-driven carrier, which was

then coupled to a X-Y recorder through a precision linear potentiometer. The travelling distance of the probe was accurately calibrated by the potentiometer and a filter network. The schematic diagram of the measurement system is shown in Figure 5.3. All the field probings were conducted in an anechoic chamber.

As the first test for the existence of a slow surface wave over the corrugated surface, a large reflecting plate (10 λ_0 x 10 λ_0 at 9 Ghz) was placed at the end of the ground plane to find the change in the phase velocity of the wave on the corrugated surface and the ground plane by observing the standing wave pattern. Figure 5.4 shows a typical field distribution over the surface with the reflecting plate installed at the end of the ground plane. It clearly shows that the periods of the standing waves on the two regions differ slightly. The period of the standing wave on the corrugated surface is shorter than that on the ground plane. This indicates the difference in the phase velocities of the waves on the two surfaces.

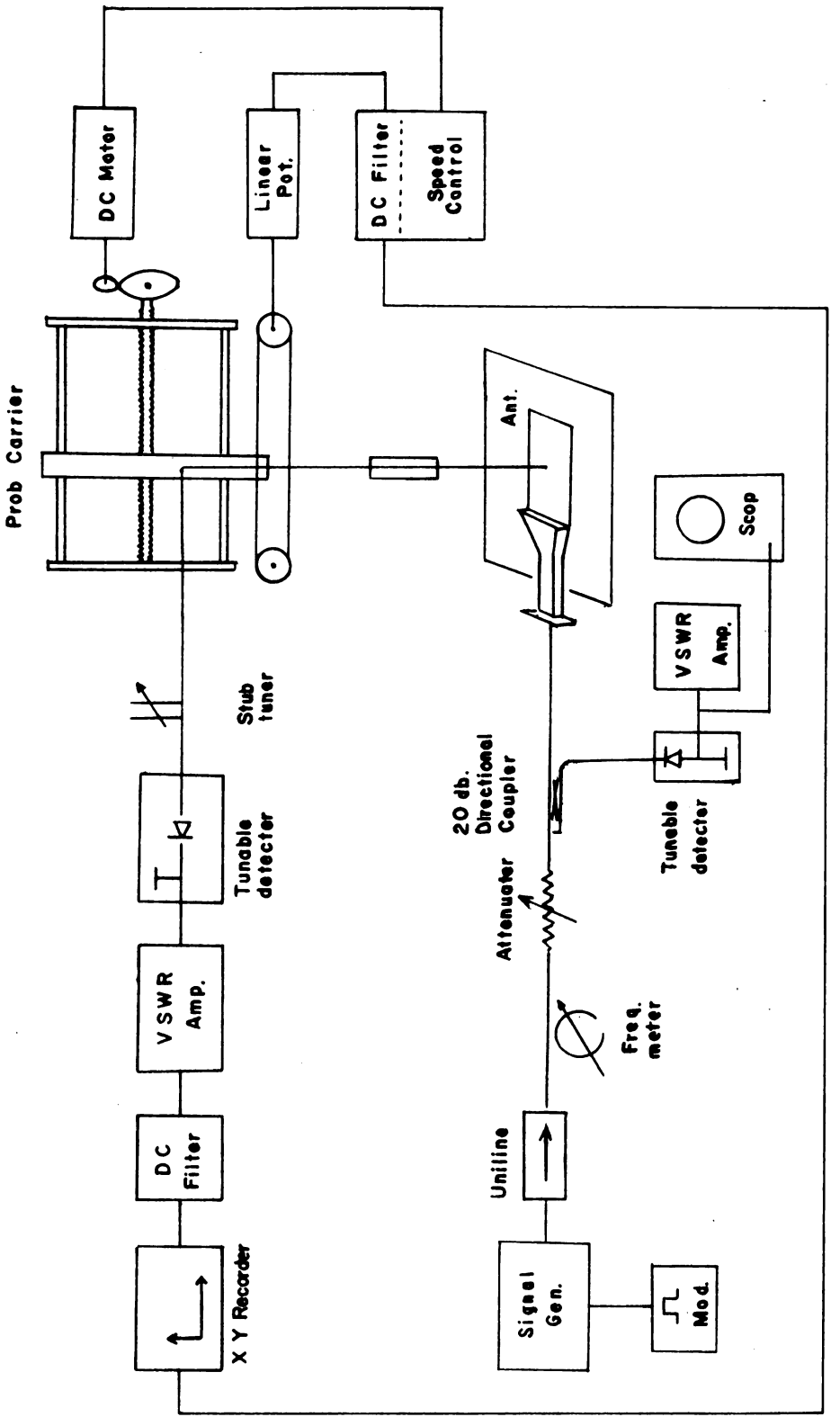

Figure 5.3 Surface Field Measurement System

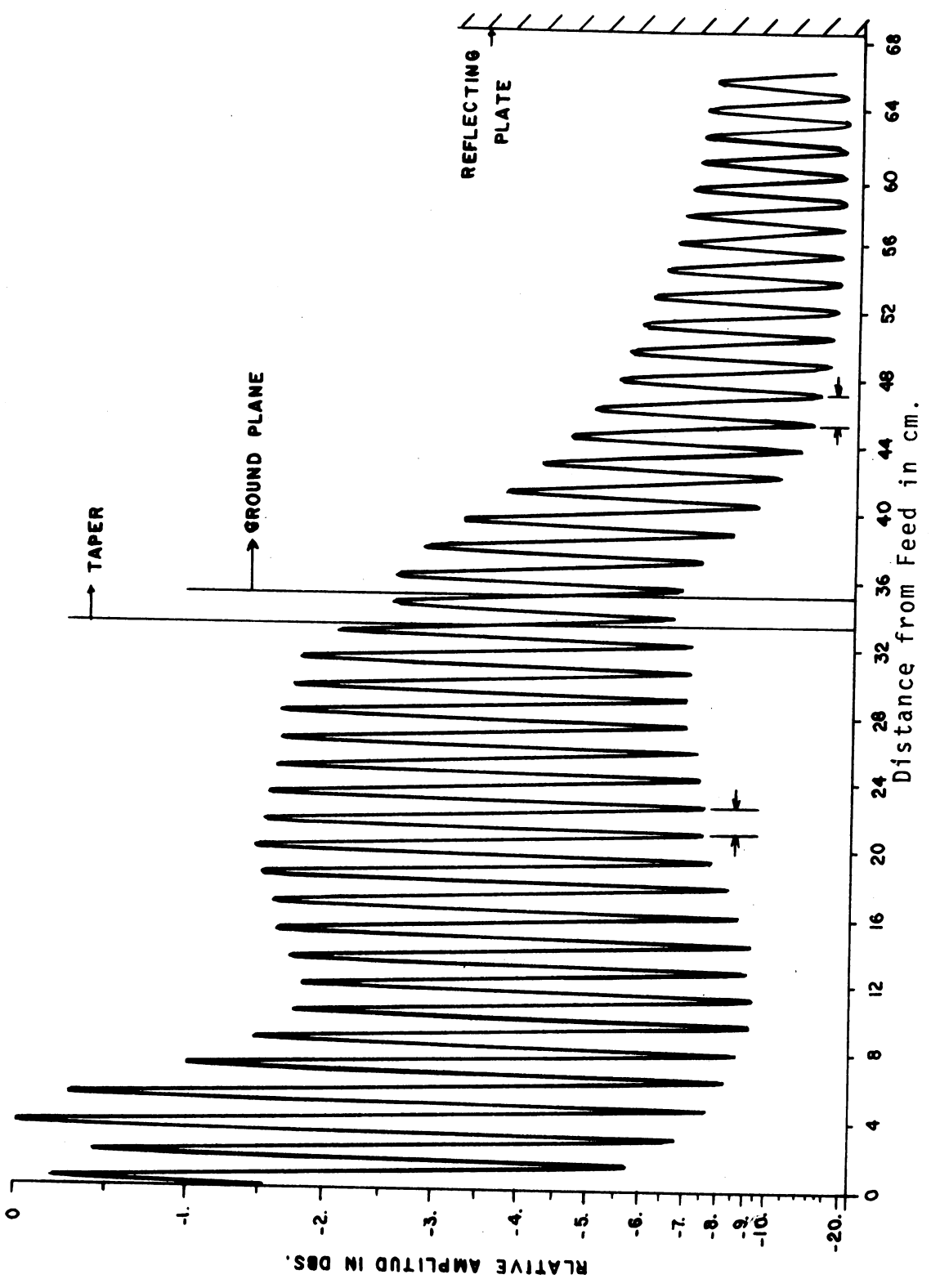

Figure 5.4 Standing Waves by a Reflecting Plate Placed at the End of Antenna

As the second test, the attenuation of the electric field (α_0 for E_y) along the normal direction away from the antenna surface was measured at several points at an interval of 10 cm along the center line of the surface. The intensity of E_y was then measured as a function of the vertical distance. The measured field intensities are plotted for several frequencies in Figure 5.5a and 5.5b. The field patterns show that the electric field attenuates very rapidly as the probe moves upward. At 3 cm height, the field has attenuated below -10 dbs; the indication of a slow surface wave with a high attenuation constant in y direction ($E_y = \frac{-\beta_0}{\omega\varepsilon} H_0 e^{-\alpha_0 y} e^{-j\beta_0 z}$). The attenuation constant α_0 was determined by plotting the field amplitude on a semi-log paper. The slope of the line on the semi-log paper corresponds to the attenuation constant α_0. Since the crystal detector detects power, the actual attenuation constant is one half of the slope of the line. Figure 5.6a shows the measured attenuation constants in comparison with the theoretical values. It shows very good agreement with theory.

With this confirmation of the existence of slow surface wave on the corrugated surface, the phase velocity of the wave was measured by a simple standing wave method. For this measurement, a large reflecting plate (10 λ_0 X 10 λ_0 at 9 Ghz.) was placed at the end of the corrugation, and the standing wave distribution of E_y component along the center line of the corrugated surface was recorded with the calibrated distance scale. This measurement was repeated five to ten times for a frequency to minimize the possible measurement errors on the calibration of the distance scale. The average guided wavelength over the surface was then calculated from the standing wave pattern.

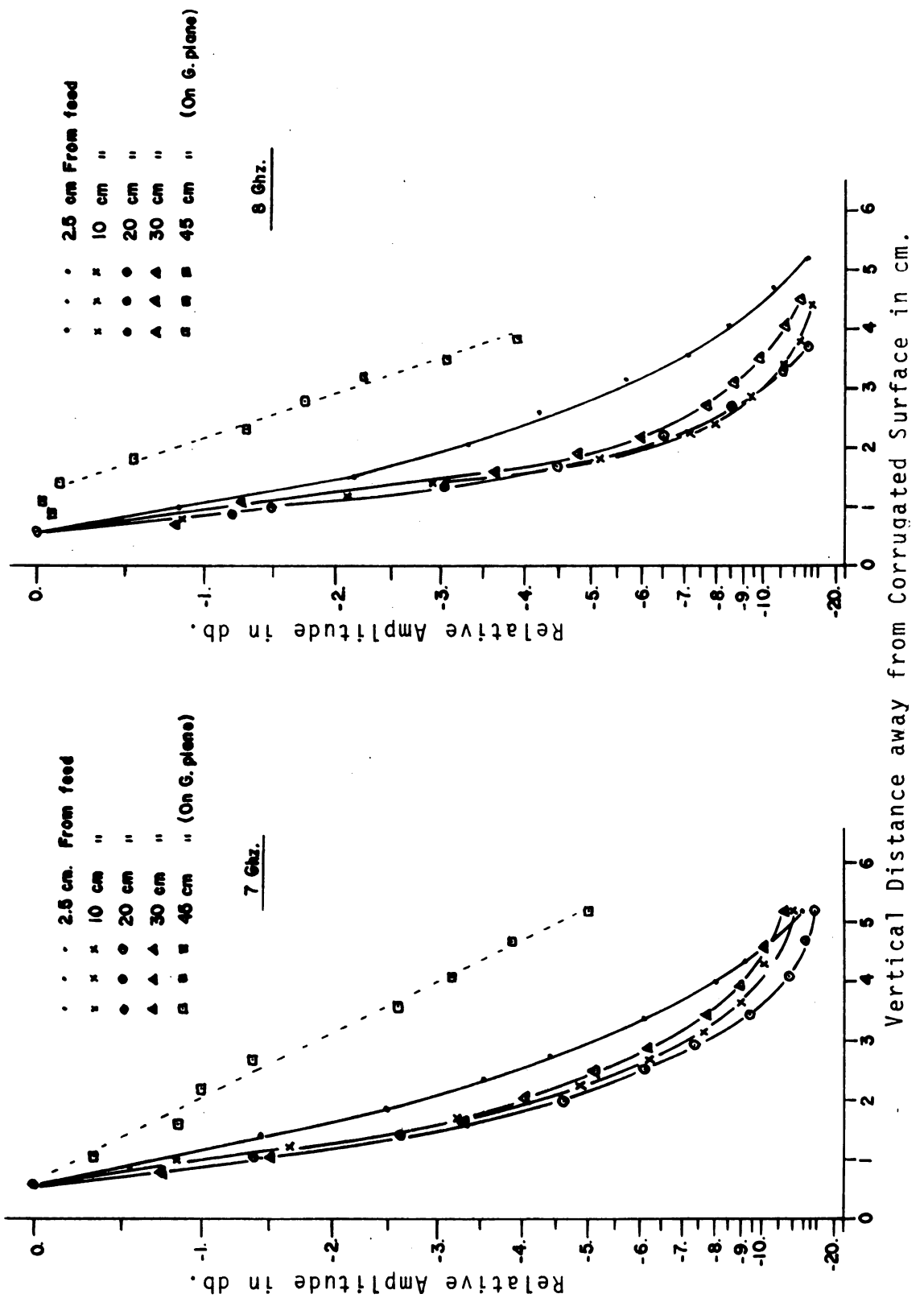

Figure 5.5a Normal Electric Field Distribution
(E_y: 7-8 Ghz.)

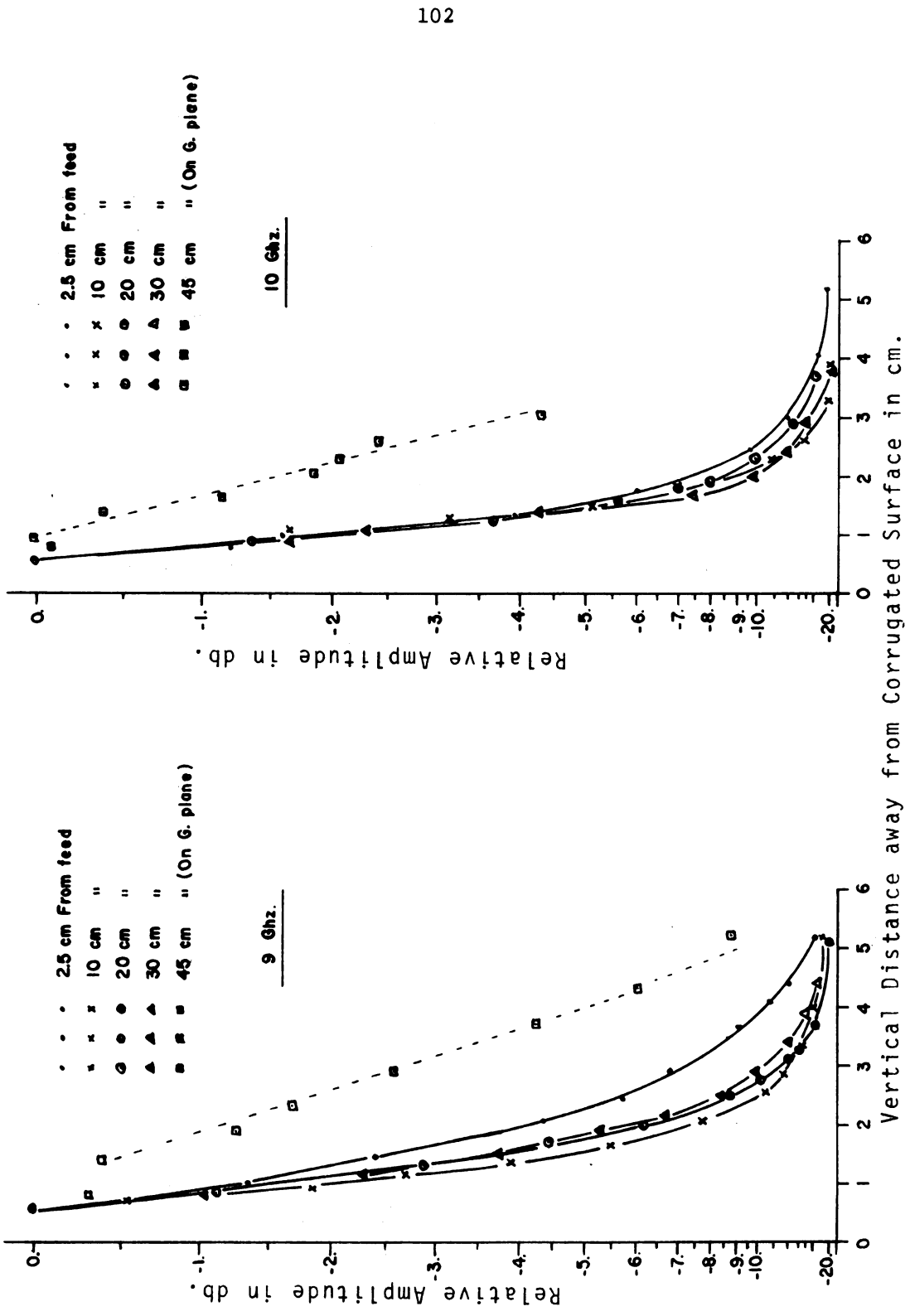

Figure 5.5b Normal Electric Field Distribution
(E_y: 9-10 Ghz.)

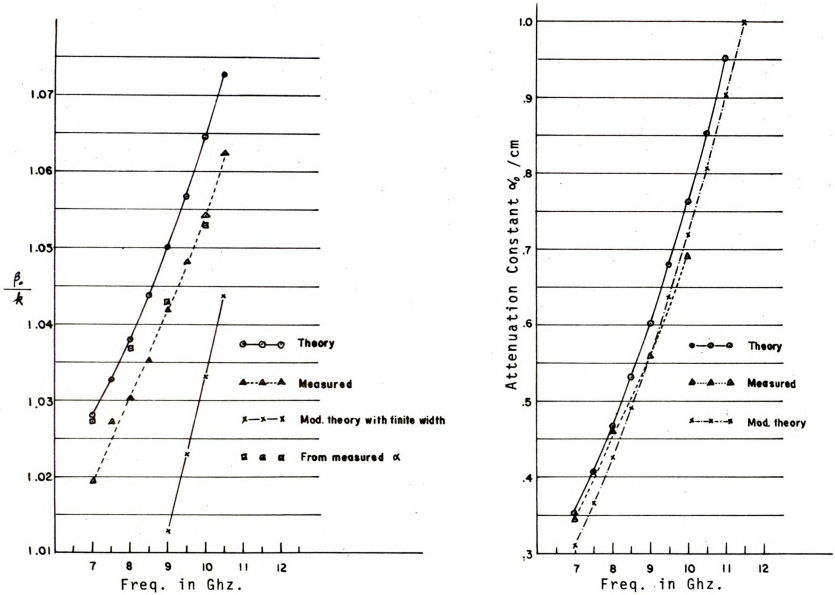

Figure 5.6 Attenuation Constant and Phase Constant

Figure 5.7 shows the typical standing wave patterns at 7 Ghz. and 9 Ghz. along with the accurately calibrated probe travelling distance. Figure 5.6b shows the measured phase constant ratio (β_0/k) for various frequencies in comparison with the theoretically predicted values. The experimental values agree with the theory for the infinitely wide corrugation within a few percent deviation. The phase velocity was also indirectly calculated from the measured attenuation constants and plotted in Figure 5.6b for comparison. Those directly and indirectly calculated values for the phase constant ratio (β_0/k) agree very well. These experimental results confirm the existence of slow surface waves over the finite corrugated surface and also indicate that the phase velocity of the slow surface wave is close to that of the fundamental harmonic over an infinitely wide corrugated surface.

The amplitude distributions of the E_y, E_z and H_x components were measured over the total antenna surface by moving the appropriate probe along in several axial directions and several transverse directions in order to get three dimensional field distribution patterns over the frequency range of 7 Ghz. to 11 Ghz. In all these experiments, the probe height was kept constant at 0.7 cm away from the surface.

The typical amplitude distributions for the E_y component along the center line of the antenna surface are shown in Figure 5.8 and 5.9. The vertical axis is the relative magnitude of the measured field intensity in decibels and the horizontal axis is the probe travelling distance from the feed. The starting and the end points of the tapered section are indicated by two vertical lines. As was expected, the field distribution near feed shows an abrupt variation. It is probably due to the feed mismatch and the direct feed radiation. Moving away from

the feed about 2 wavelengths, the field settles down and exhibits a nearly uniform standing wave pattern. This standing wave may be caused by the impedance mismatch of the surface wave at the junction between the corrugation and the ground plane and at the end of the ground plane. The average reflection coefficients over the corrugated surface by the mismatches were calculated from the surface field distribution of the E_y component, and the results are plotted in Figure 5.10 for several frequencies in comparison with the approximate theoretical values. The measured reflection coefficient without the tapered section generally agrees with the approximate thoery, but the effects of the tapered section to the field mismatches are not conclusive from the results. In the course of the experiment, it was found that the electrical contact between the uniform corrugated surface section and the tapered corrugated section was very sensitive to the reflection coefficient as the wave on the surface slows down. Thus, for the meaningful results on the reflection coefficient, the electrical contact between the sections is required to be perfect.

Comparing the field distribution patterns for the cases with and without the tapered section in Figure 5.8 and 5.9, it was found that the tapered section offered a very good match for the low frequency case where the phase velocity of the surface wave was close to the speed of light. At the high frequency where the phase velocity is much slower, the tapered section failed to act as a matching section. It may imply that the length of the tapered section is the critical factor for the perfect matching as the case of the tapered uniform transmission lines (70).

Among the field components on the guiding surface, the E_z component may have the largest discontinuity at the end of the corrugation. In order to see whether the tapered section offers a smooth transition for the E_z component, the E_z field distribution was measured by using an E_z probe for the cases of with and without tapered section. The results are plotted in Figure 5.11 and Figure 5.12. As was found in the field distributions for the E_y component, the tapered section did not seem to act as a matching section for the E_z component at all. Thus, it may be necessary to investigate the fields over the tapered corrugated surface more carefully to determine the optimum length for minimum reflection due to the discontinuity. In the E_z field distributions, it was found that the E_z field is uniformly distributed over the guiding surface for all frequencies, even near the feed. This indicates that the fields in the corrugated guide have efficiently transformed to the surface wave on the open corrugated surface.

The distribution of the magnetic field component H_x of the surface wave was measured over the total antenna surface by a single loop probe. Since the single loop probe is also sensitive to the axial electric field component E_z on the corrugated surface, the measured field patterns are not pure magnetic field distribution on the corrugated surface, but they are true magnetic field distribution on the ground plane. However, since the intensity of the E_z component is very small compared to that of the H_x component ($E_z = -\frac{\alpha_0}{\omega\varepsilon} H_x$), the measured values may be mainly contributed by the H_x field component. Figure 5.13 and Figure 5.14 show the field distributions for the H_x component with and without the tapered section. The dotted line on the ground plane is the theoretically predicted curve. It shows that the theoretical

prediction does not agree with the experiment. In theory, the H field intensity on the tapered section was assumed the same as that on the uniform corrugated surface, but in the experiment the H field starts decreasing at the start of the tapered section as shown in Figure 5.13. In plotting the theoretical values, the normalized amplitude was chosen roughly the average level of the H_x on the corrugated surface. This level may not be totally H_x but a combination with E_z. On the corrugated surface, the disagreement between the theory and the experiment is expected, since the surface wave near the feed is supposed to be contaminated by the direct feed radiation which was not included in the theory. However, the field distribution away from the feed is almost uniform as the surface wave should behave, except a small standing wave component due to the mismatch at the ends of the corrugation and the ground plane.

In order to understand the complete surface field distribution on the antenna surface, the field distributions along several transverse directions were measured at several locations on the antenna surface. In each transverse plane, the field amplitude was normalized to the field strength at the center of the cross section, and plotted as a function of the probe travelling distance x. Figure 5.15 a-d and Figure 5.16 a-d show the transverse electric field distribution (E_y) and the transverse magnetic field distribution (H_x) respectively. The horizontal and vertical axes are the probe travelling distance at the several cross sections. The amplitude of the distribution can be read with the scale shown in the bottom left corner. Each field is normalized to zero db at the peak of the distribution that occurs along the center line of the antenna surface. Since the E_y component is directly related to the H_x

component by the surface impedance ($E_y = -\frac{\beta_0}{\omega\varepsilon} H_x$) based on theory, the normalized field patterns are almost identical. It is noted in Figure 5.15 a-d that the field variations resemble the $\cos(\frac{\pi x}{w})$ function over the surface. The $\cos(\frac{\pi x}{w})$ function is shown as the dotted lines for comparison in the figures. Note also that the guided waves are mostly confined to the corrugated surface and that the relative magnitude of the induced field on the ground plane in the vicinity of the corrugated surface is very small, well below -10 dbs along the side boundaries. Even on the ground plane in the strip of the same width as the corrugated surface, the induced field variations are close to the cosine function. As the phase velocity of the guided wave on the corrugated surface becomes slower, the induced field on the ground plane is mostly confined to the strip of the same width of the corrugated surface with slightly increasing intensity. Thus, for the phase velocity ratio β_0/k greater than 1.05, the transverse dimension of the ground plane may not be as important as compared to the length of the ground plane in determining the radiation patterns. The amplitude of the induced field is very low compared with the guided wave on the corrugation as evidenced in Figure 5.8, and the amplitude seems to spread out as it travels toward the end of the ground plane with rapidly reducing intensity.

With the above information on the surface field variations on the antenna surface, three dimensional field distributions were constructed. Figures 5.16 a,b,c are the normalized three dimensional field patterns for the surface field on the antenna surface. The figures illustrate the confinement of the wave on the corrugated surface and on a strip of the ground plane.

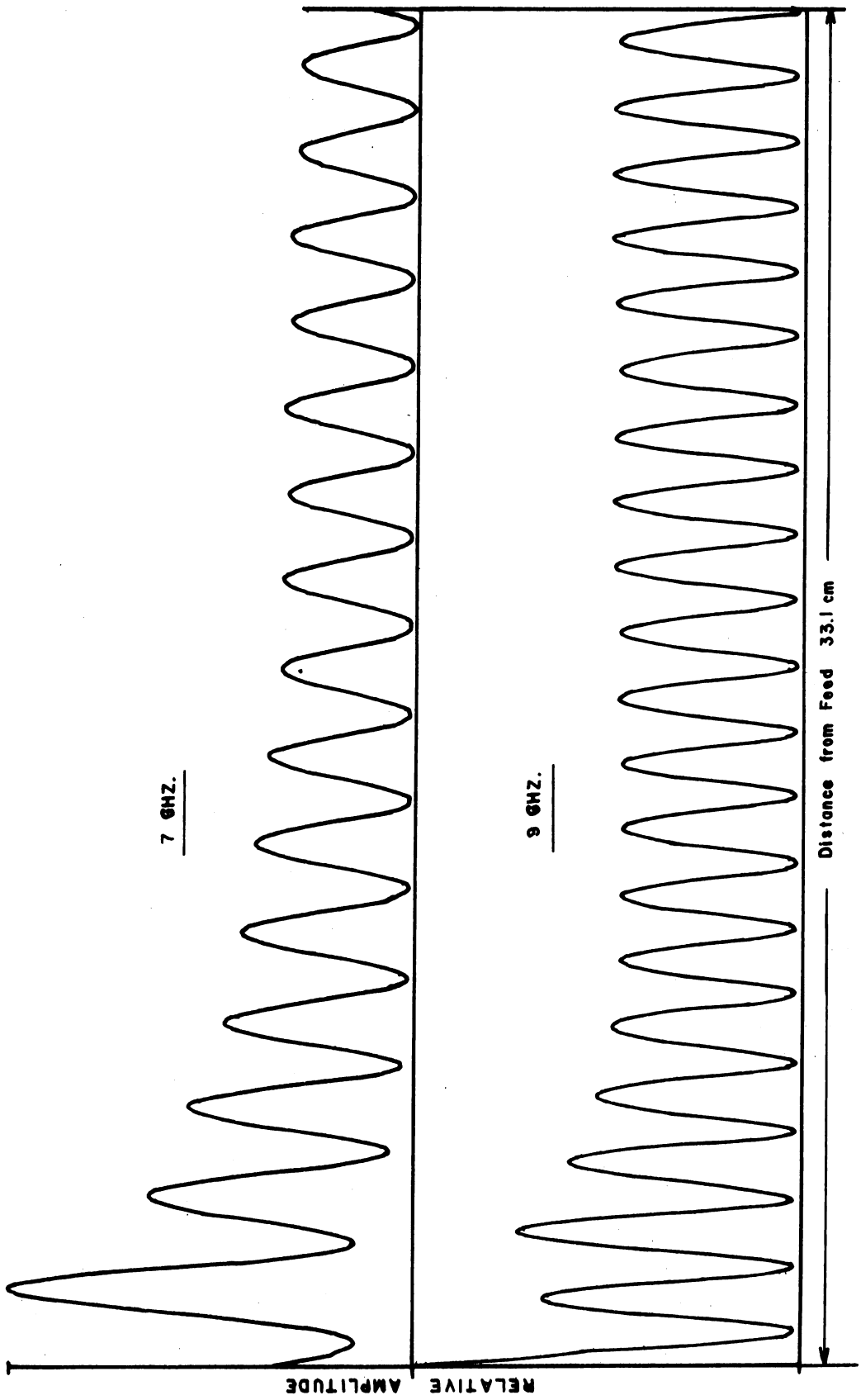

Figure 5.7 Typical Standing Wave Patterns of Surface Wave by a Reflecting Plate

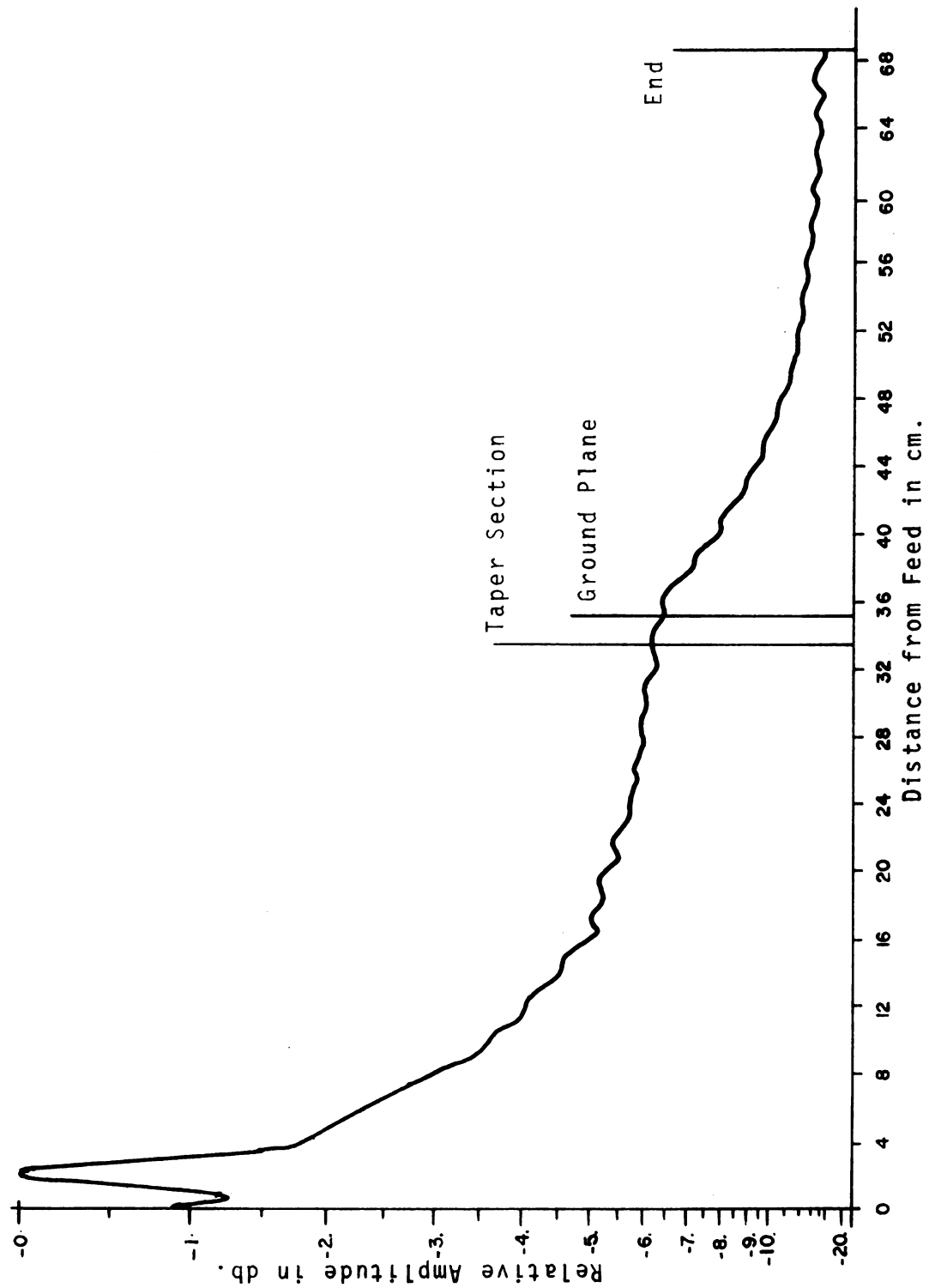

Figure 5.8a Surface Field Distribution for E_y with Tapered Section (7 Ghz.)

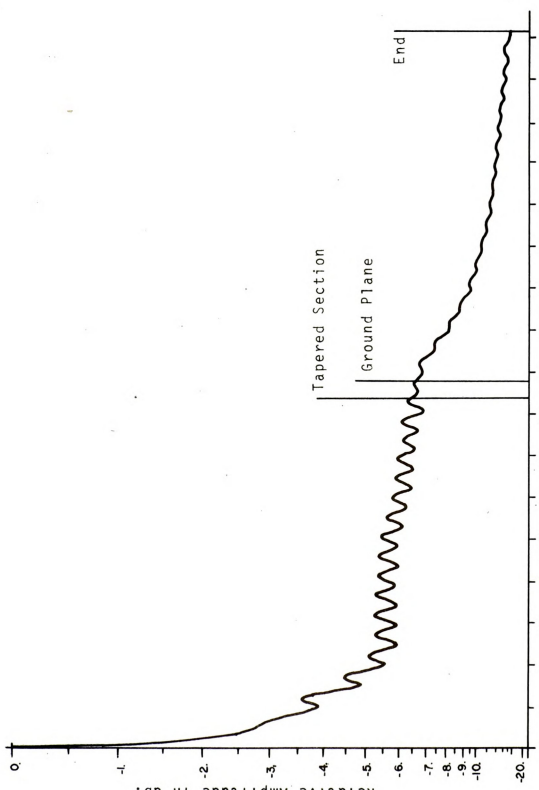

Figure 5.8b Surface Field Distribution for E_y with Tapered Section (8 Ghz.)

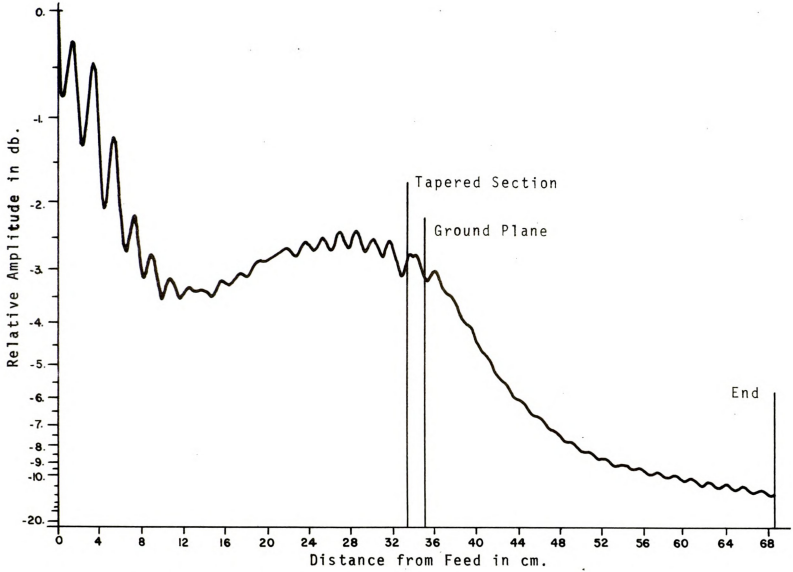

Figure 5.8c Surface Field Distribution for E_y with Tapered Section (9 Ghz.)

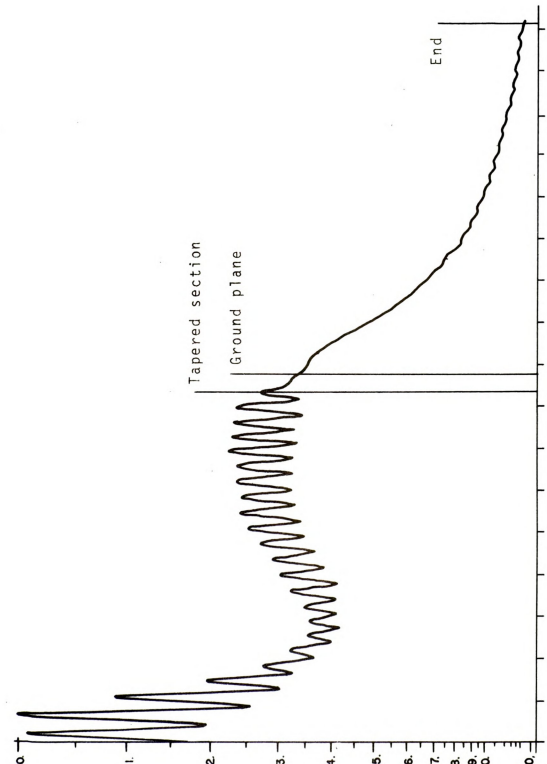

Figure 5.8d Surface Field Distribution for E_y with Tapered Section (10 Ghz.)

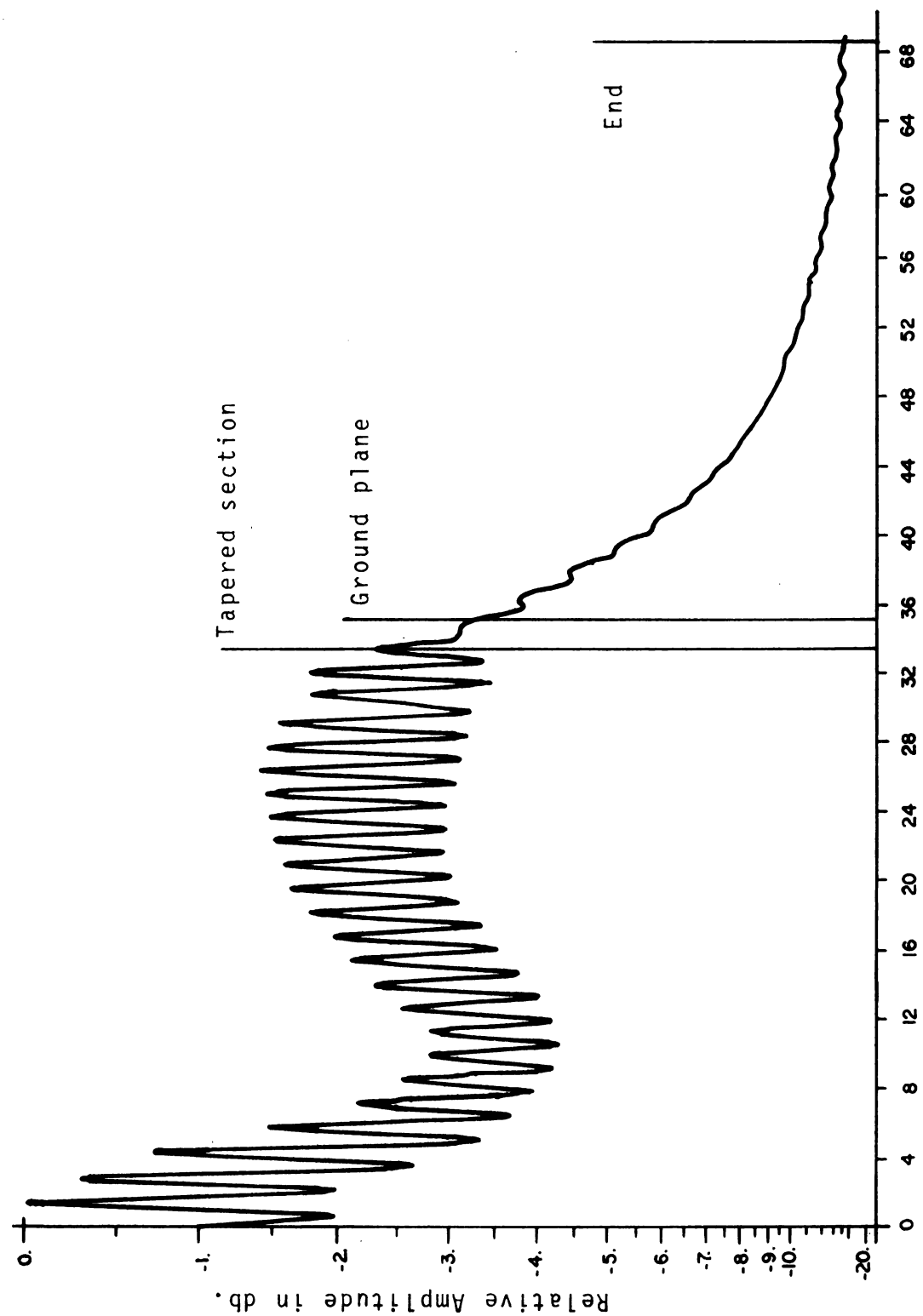

Figure 5.8e Surface Field Distribution for E_y with Tapered Section (10.5 Ghz.)

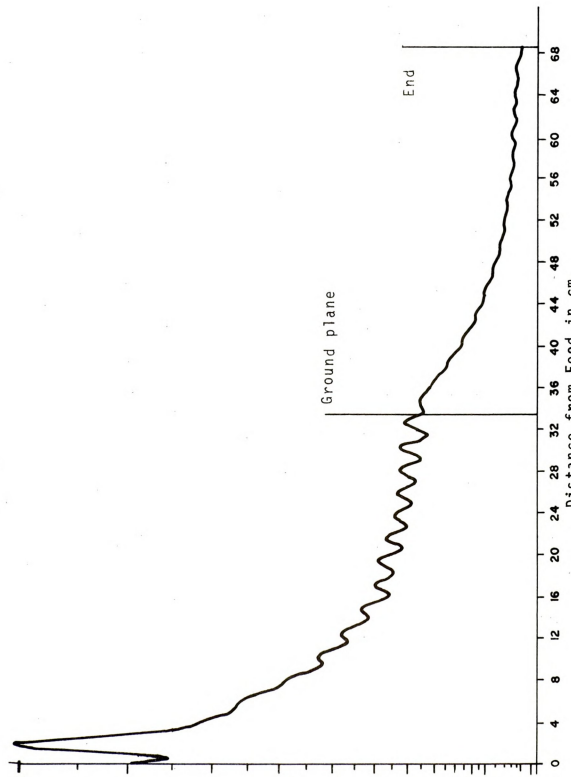

Figure 5.9a Surface Field Distribution for E_y without Tapered Section (7 Ghz.)

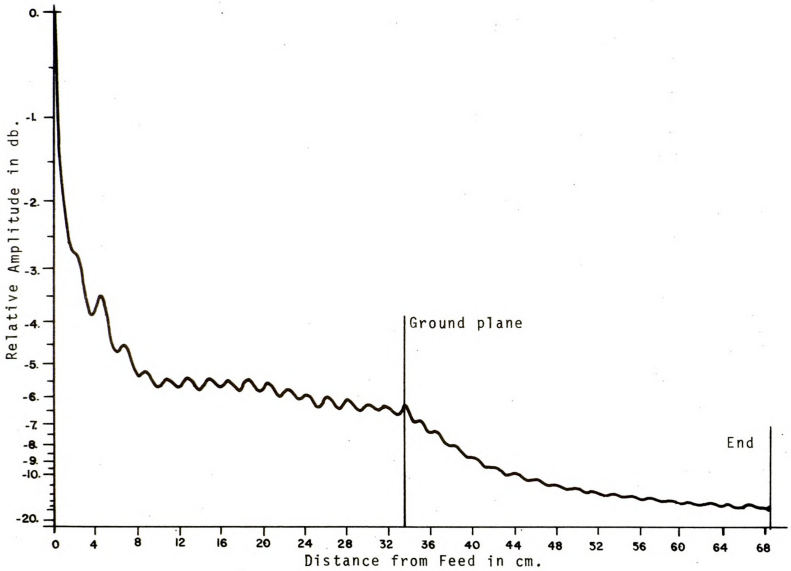

Figure 5.9b Surface Field Distribution for E_y without Tapered Section (8 Ghz.)

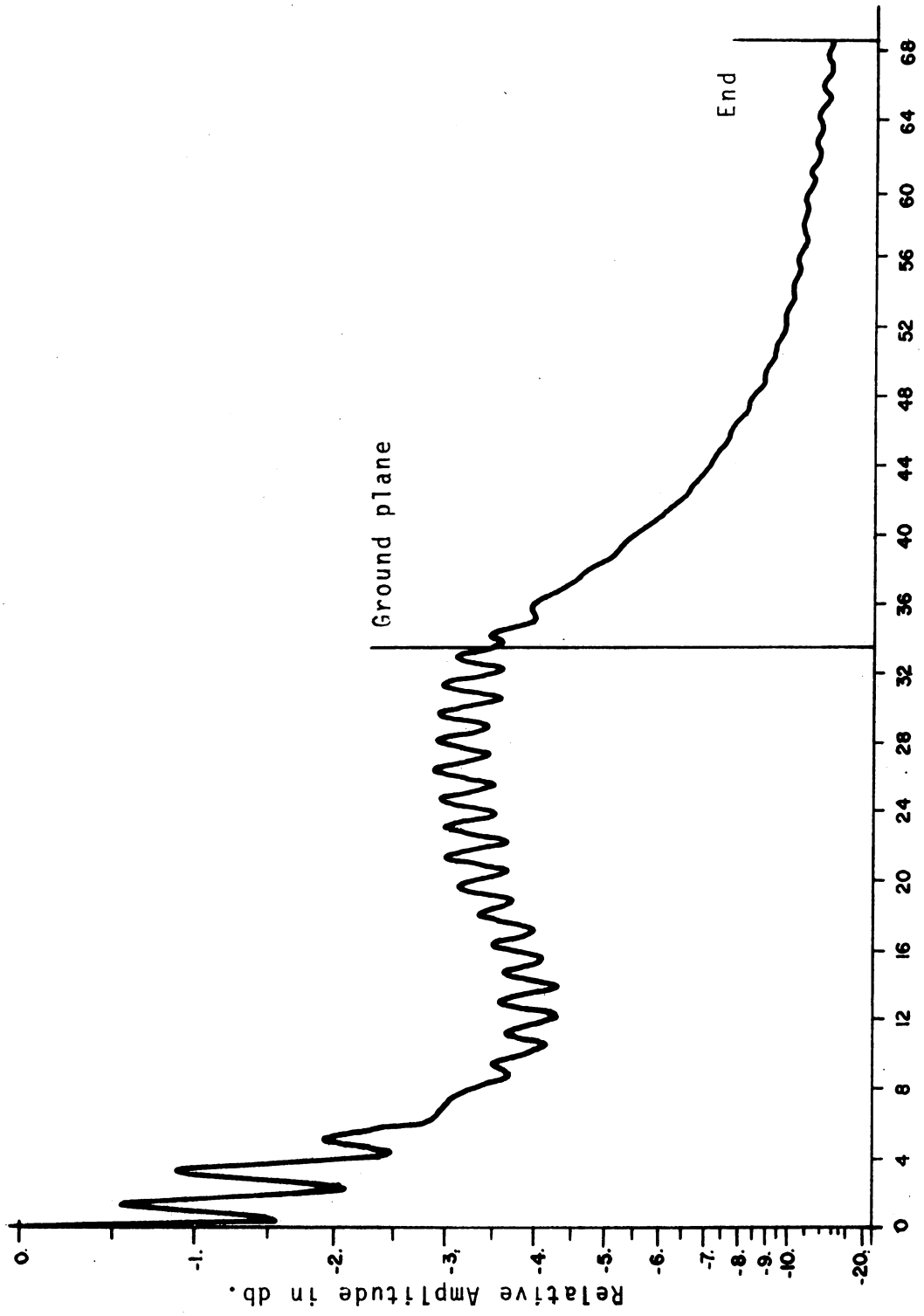

Figure 5.9c Surface Field Distribution for E_y without Tapered Section (9 Ghz.)

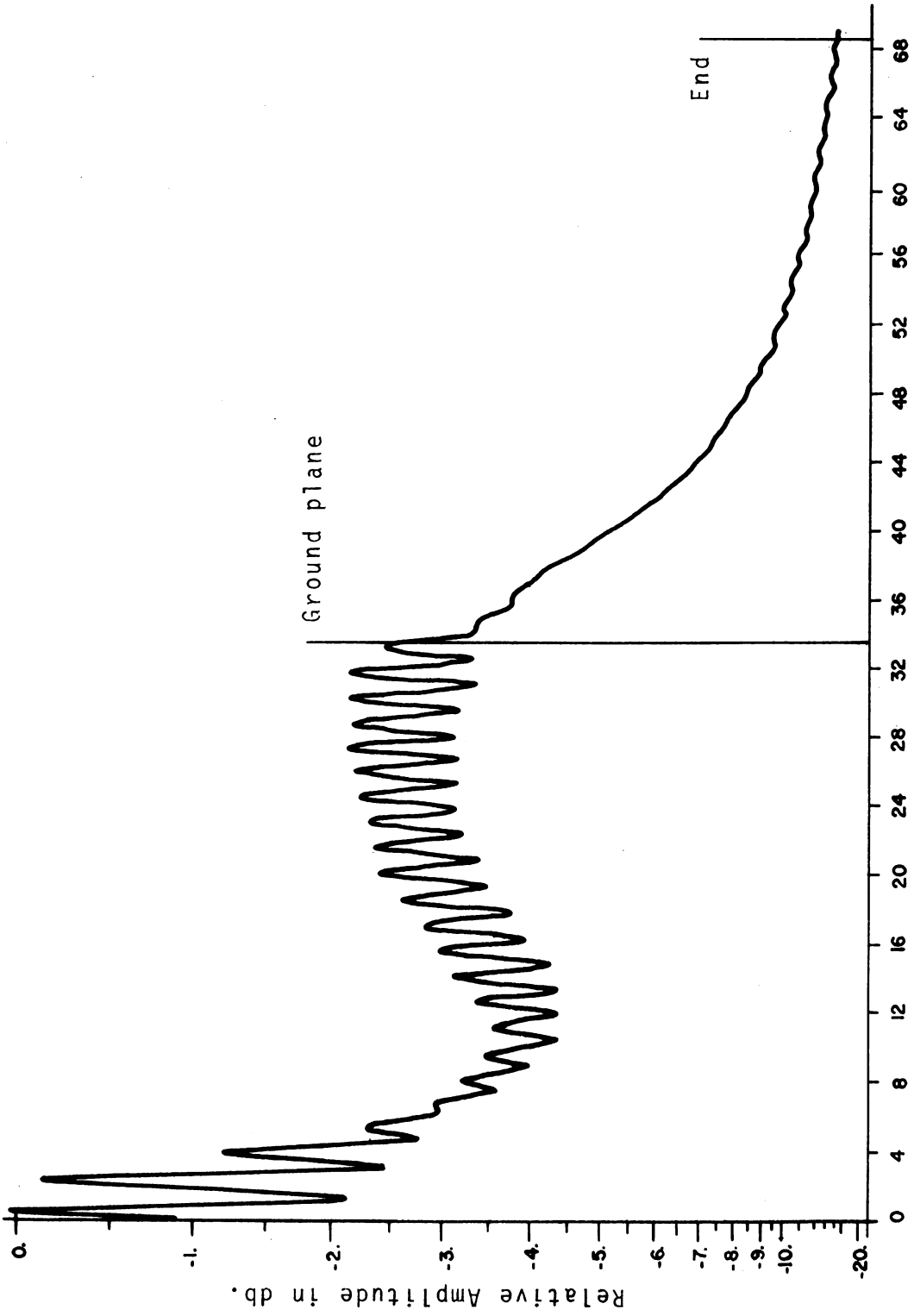

Figure 5.9d Surface Field Distribution for E_y without Tapered Section (10 Ghz.)

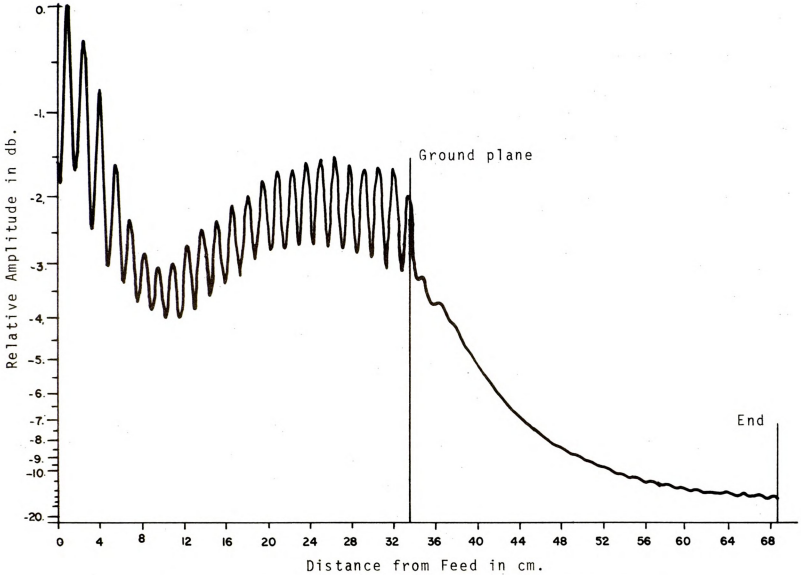

Figure 5.9e Surface Field Distribution for E_y without Tapered Section (10.5 Ghz.)

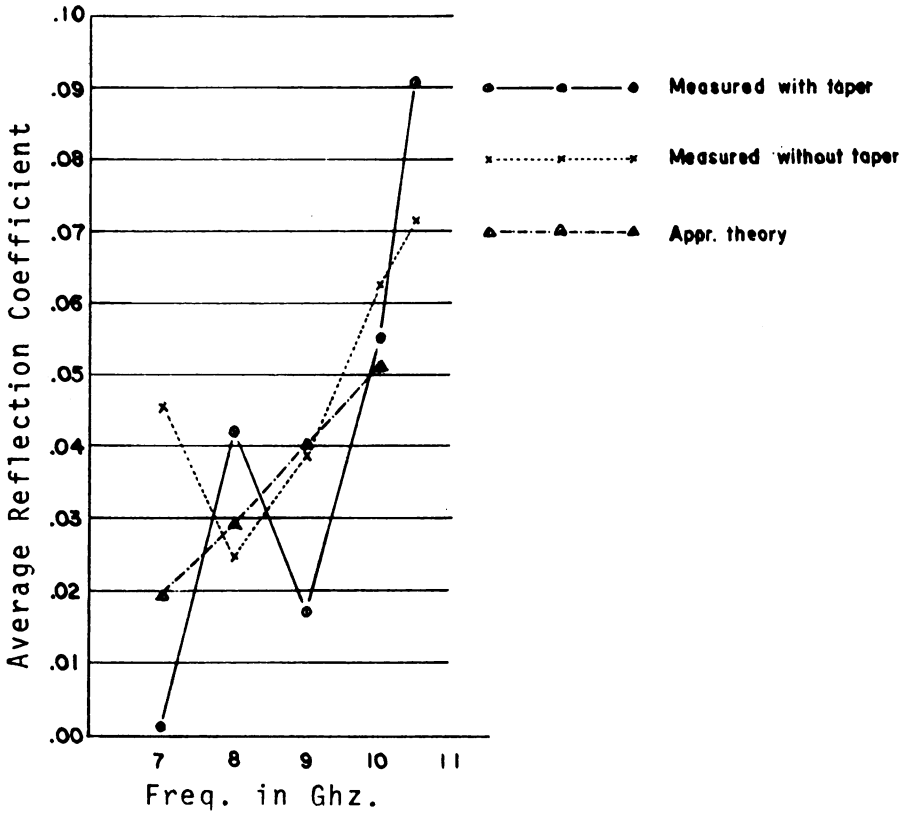

Figure 5.10 Average Reflection Coefficient Over Corrugated Surface for E_y Component

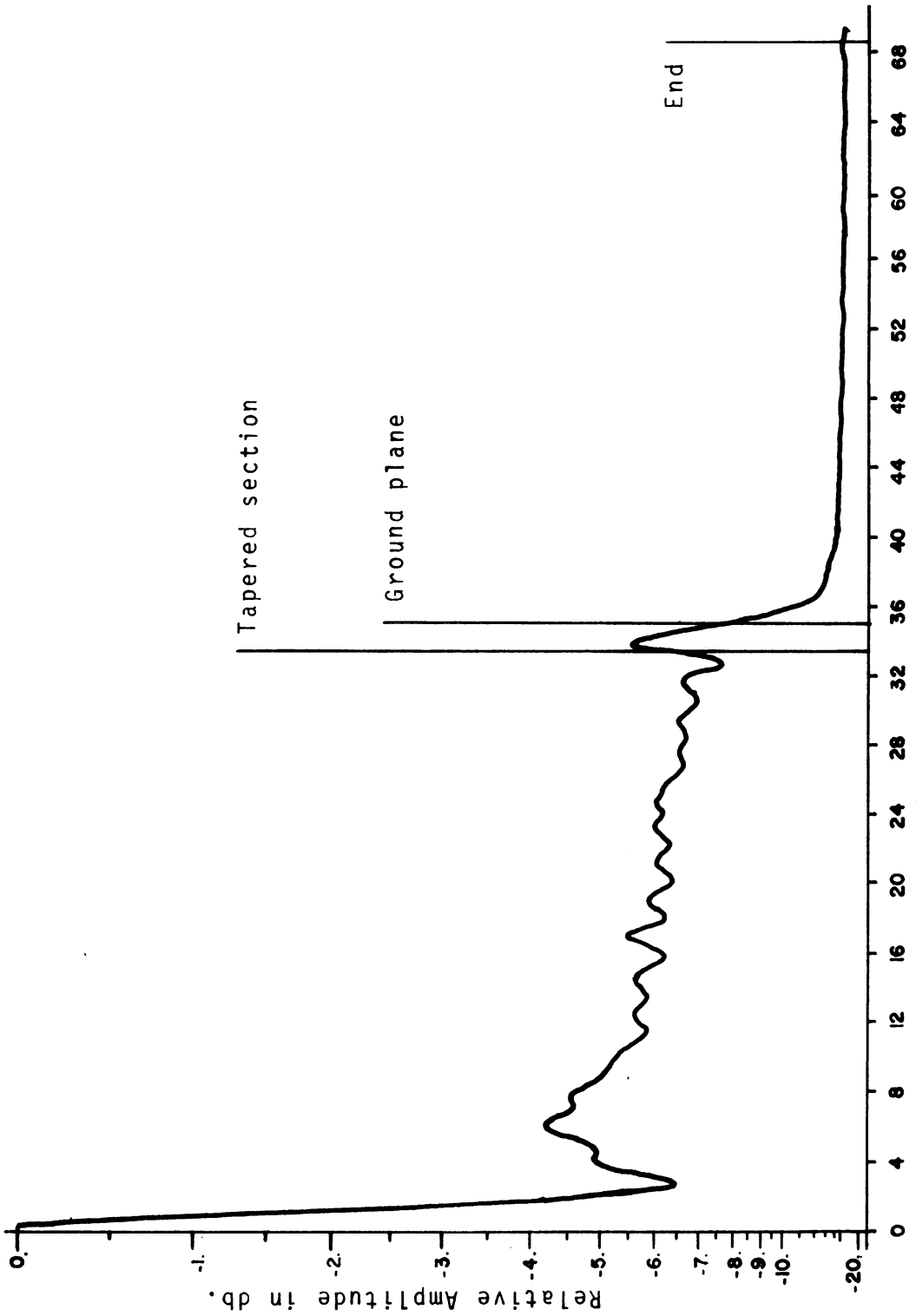

Figure 5.11a Surface Field Distribution for E_z with Tapered Section (7 Ghz.)

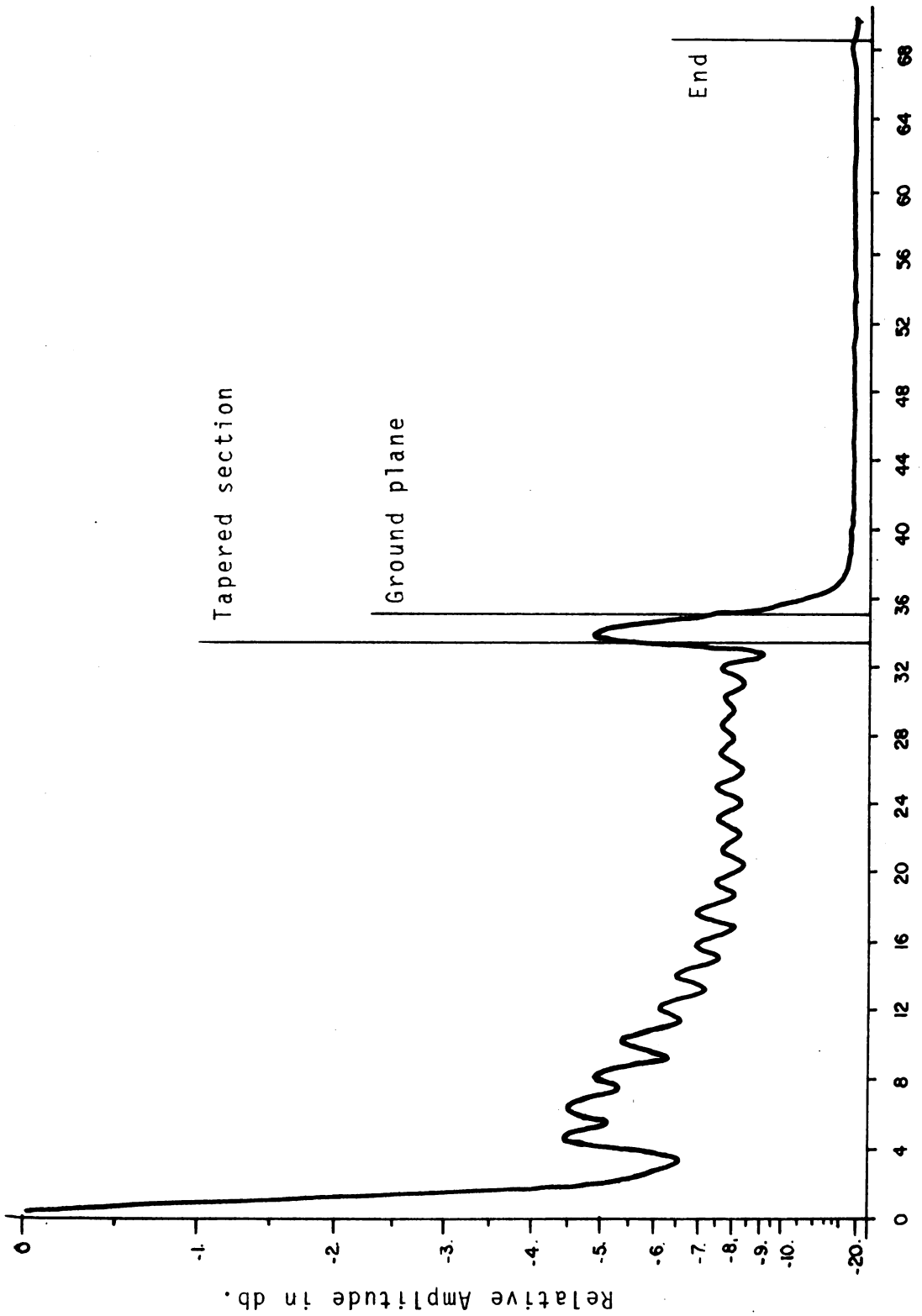

Figure 5.11b Surface Field Distribution for E_z with Tapered Section (8 Ghz.)

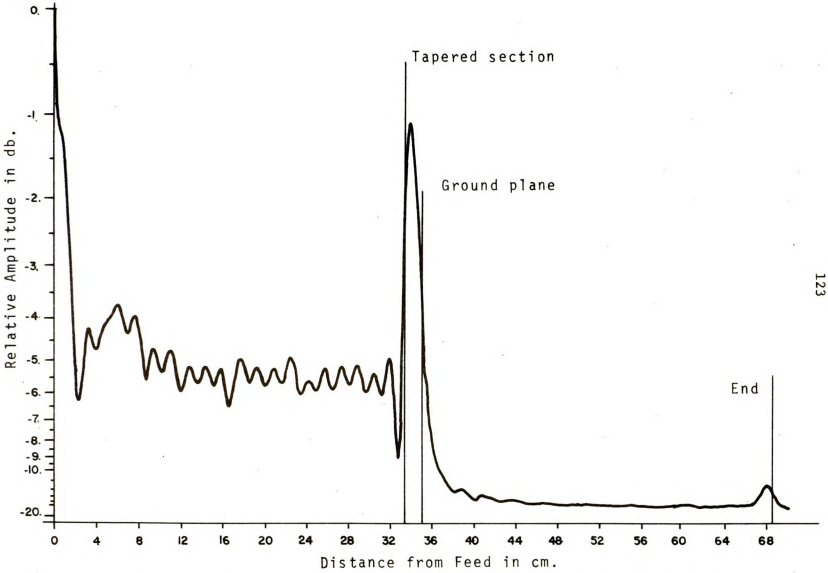

Figure 5.11c Surface Field Distribution for E_z with Tapered Section (9 Ghz.)

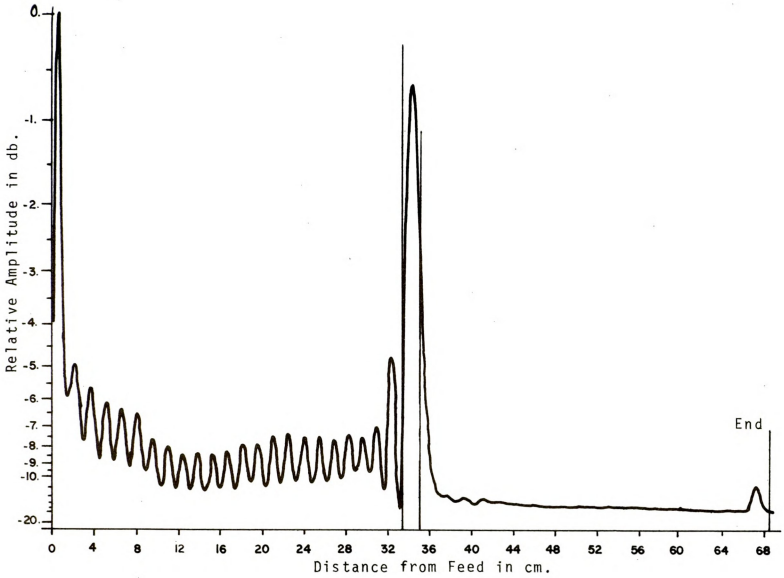

Figure 5.11d Surface Field Distribution for E_z with Tapered Section (10 Ghz.)

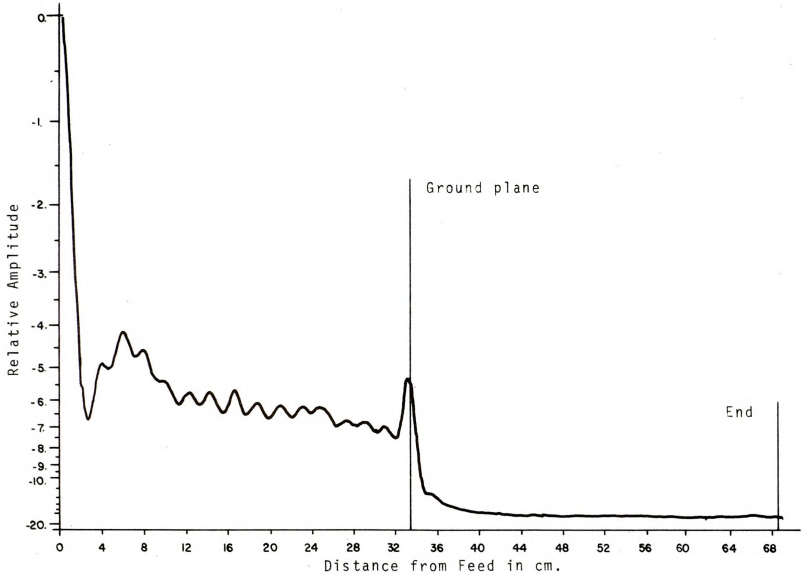

Figure 5.12a Surface Field Distribution for E_z without Tapered Section (7 Ghz.)

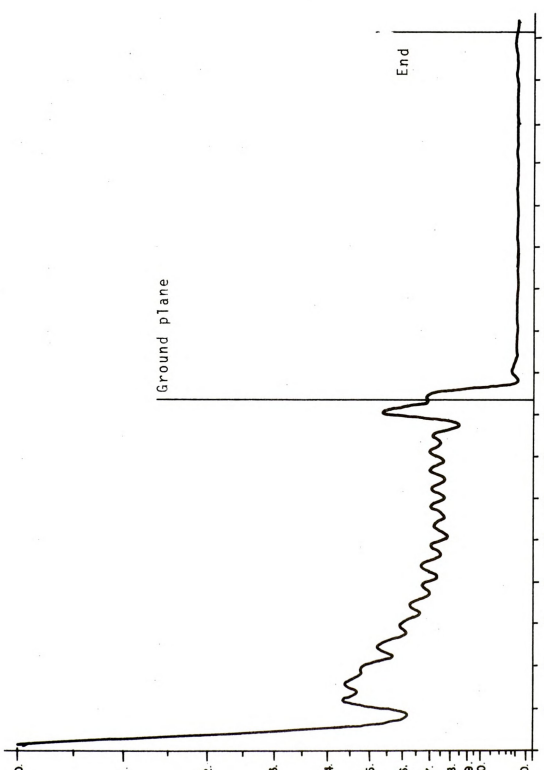

Figure 5.12b Surface Field Distribution for E_z without Tapered Section (8 Ghz.)

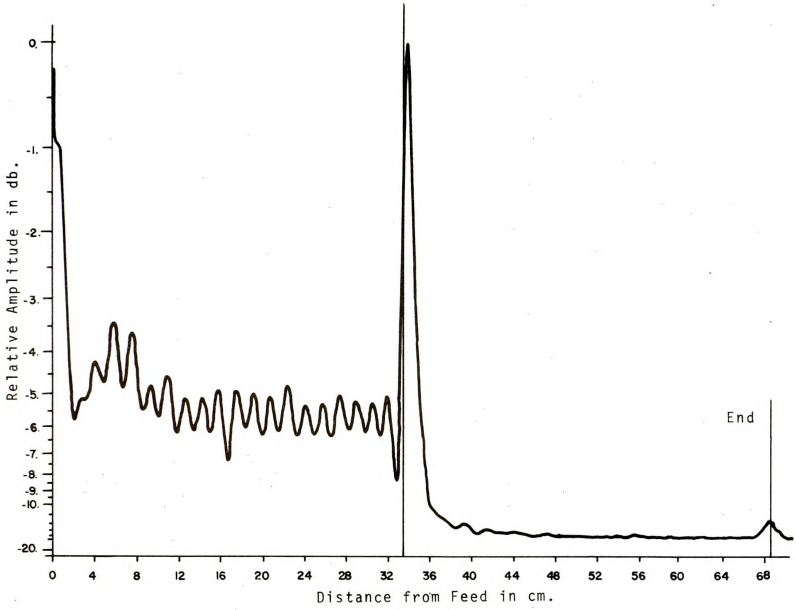

Figure 5.12c Surface Field Distribution for E_z without Tapered Section (9 Ghz.)

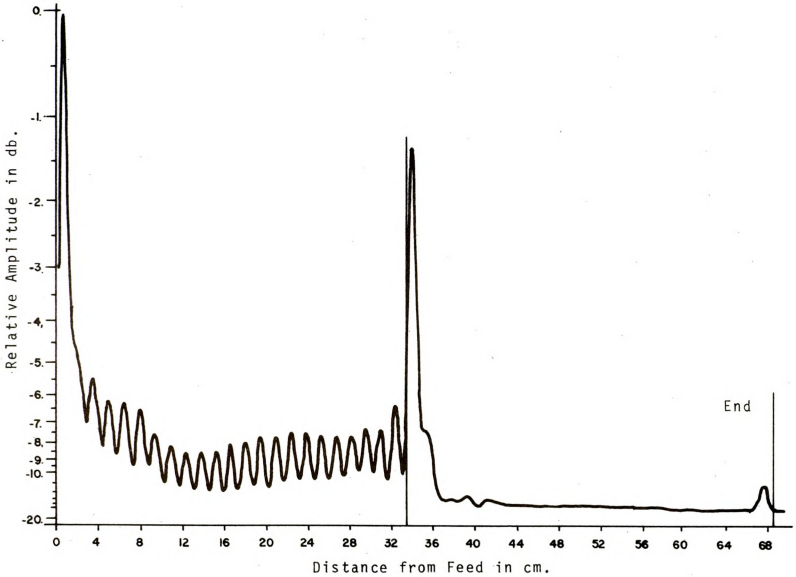

Figure 5.12d Surface Field Distribution for E_z without Tapered Section (10 Ghz.)

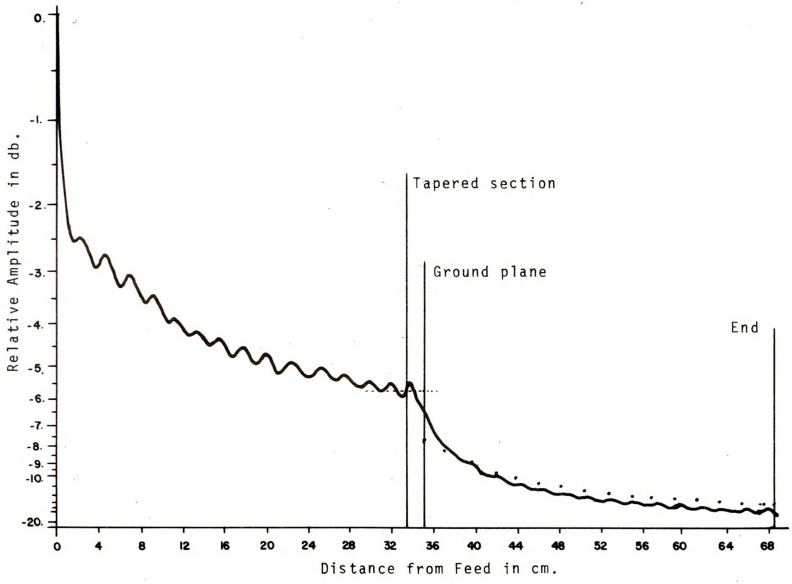

Figure 5.13a Surface Field Distribution for H_x with Tapered Section
(7 Ghz.: _____ measured, ... calculated)

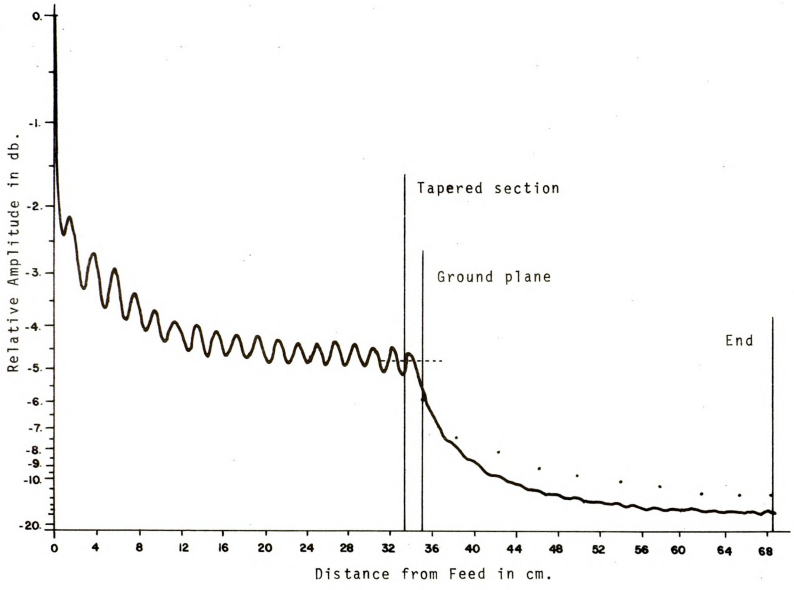

Figure 5.13b Surface Field Distribution for H_x with Tapered Section
(8 Ghz.: _____ measured, ... calculated)

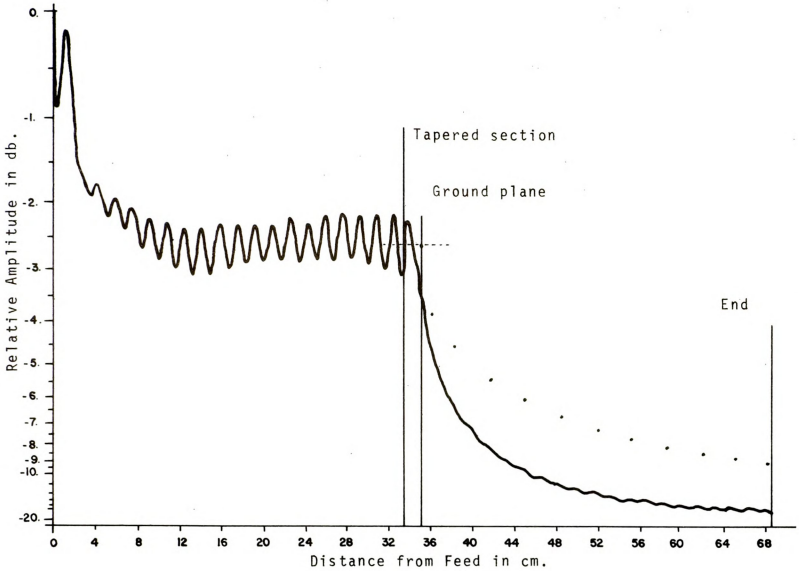

Figure 5.13c Surface Field Distribution for H_x with Tapered Section
(9 Ghz.: _____ measured, ... calculated)

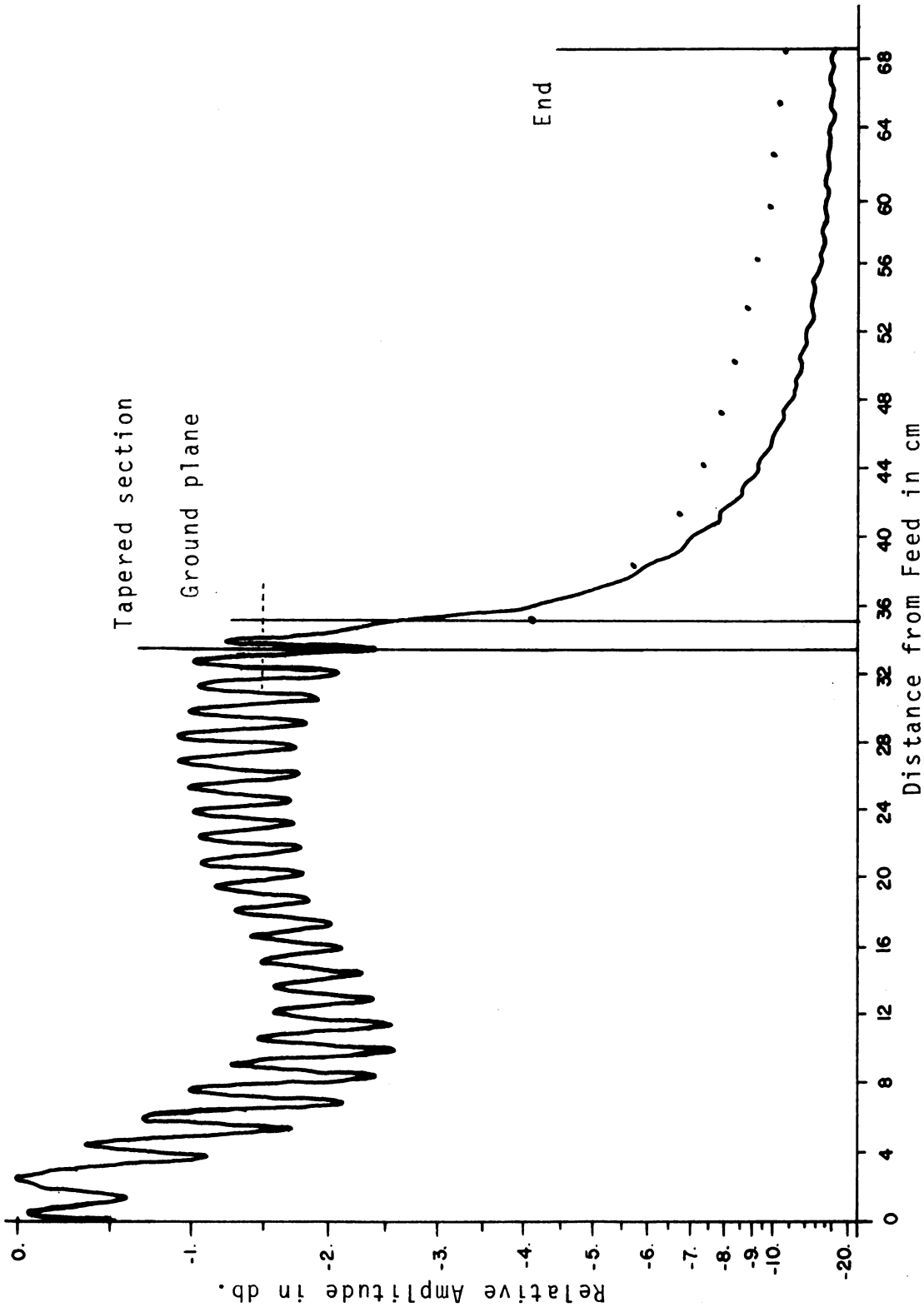

Figure 5.13d Surface Field Distribution for H_x with Tapered Section
(10 Ghz.: _____ measured, ... calculated)

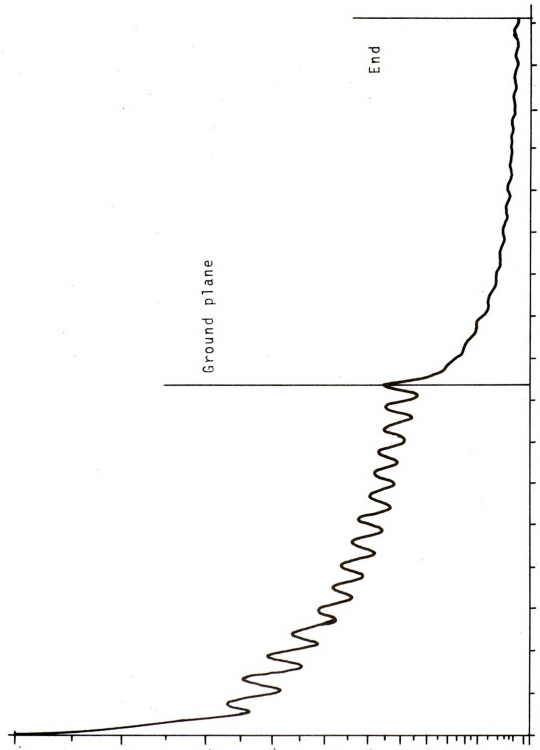

Figure 5.14a Surface Field Distribution for H_x without Tapered Section (7 Ghz.)

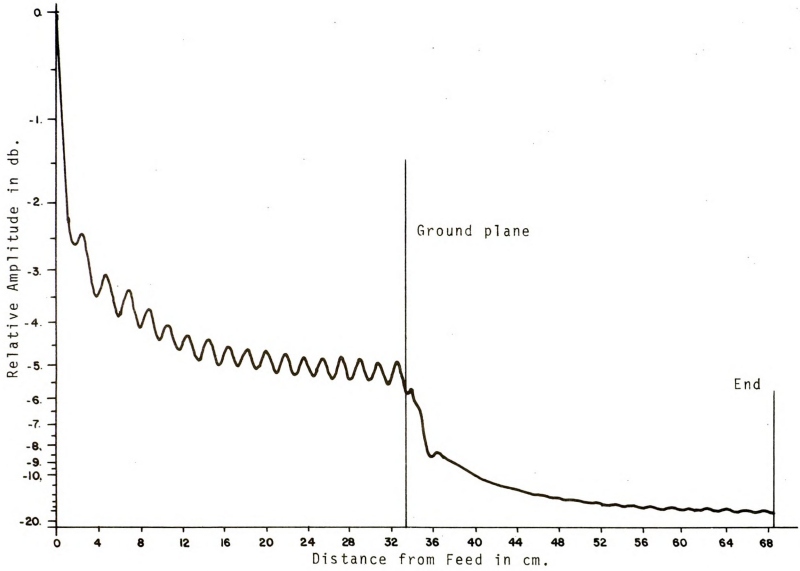

Figure 5.14b Surface Field Distribution for H_x without Tapered Section (8 Ghz.)

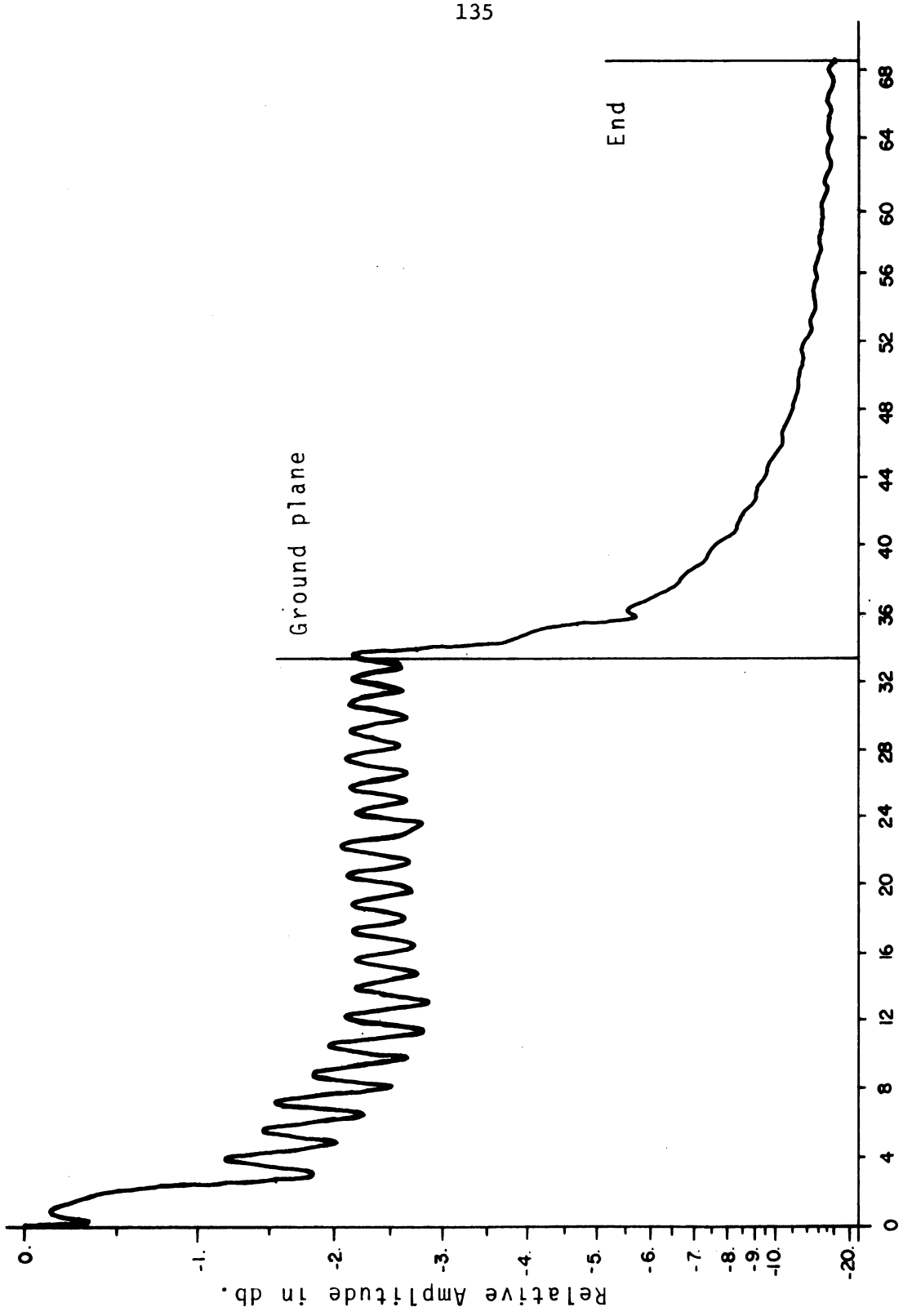

Figure 5.14c Surface Field Distribution for H_x without Tapered Section (9 Ghz.)

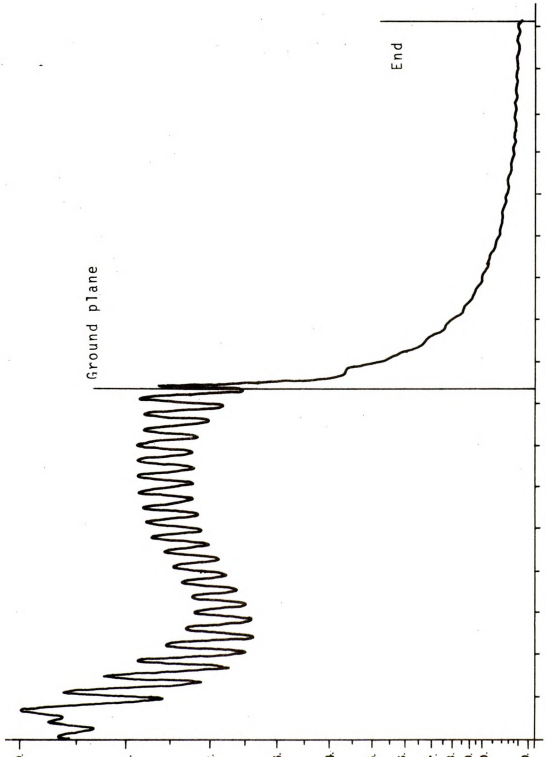

Figure 5.14d Surface Field Distribution for H_x without Tapered Section (10 Ghz.)

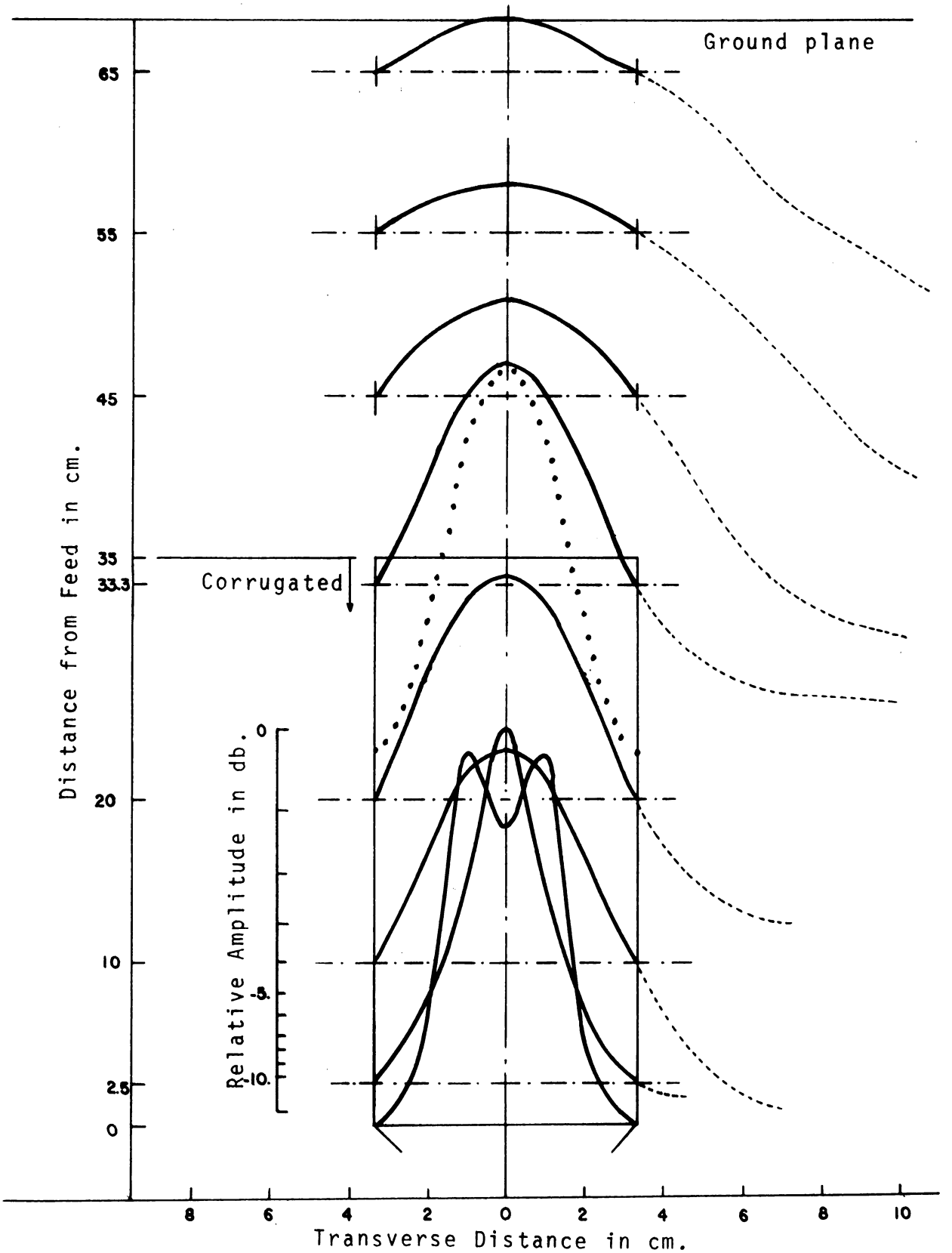

Figure 5.15a Surface Field Distribution for E_y in Transverse Direction (7 Ghz.)

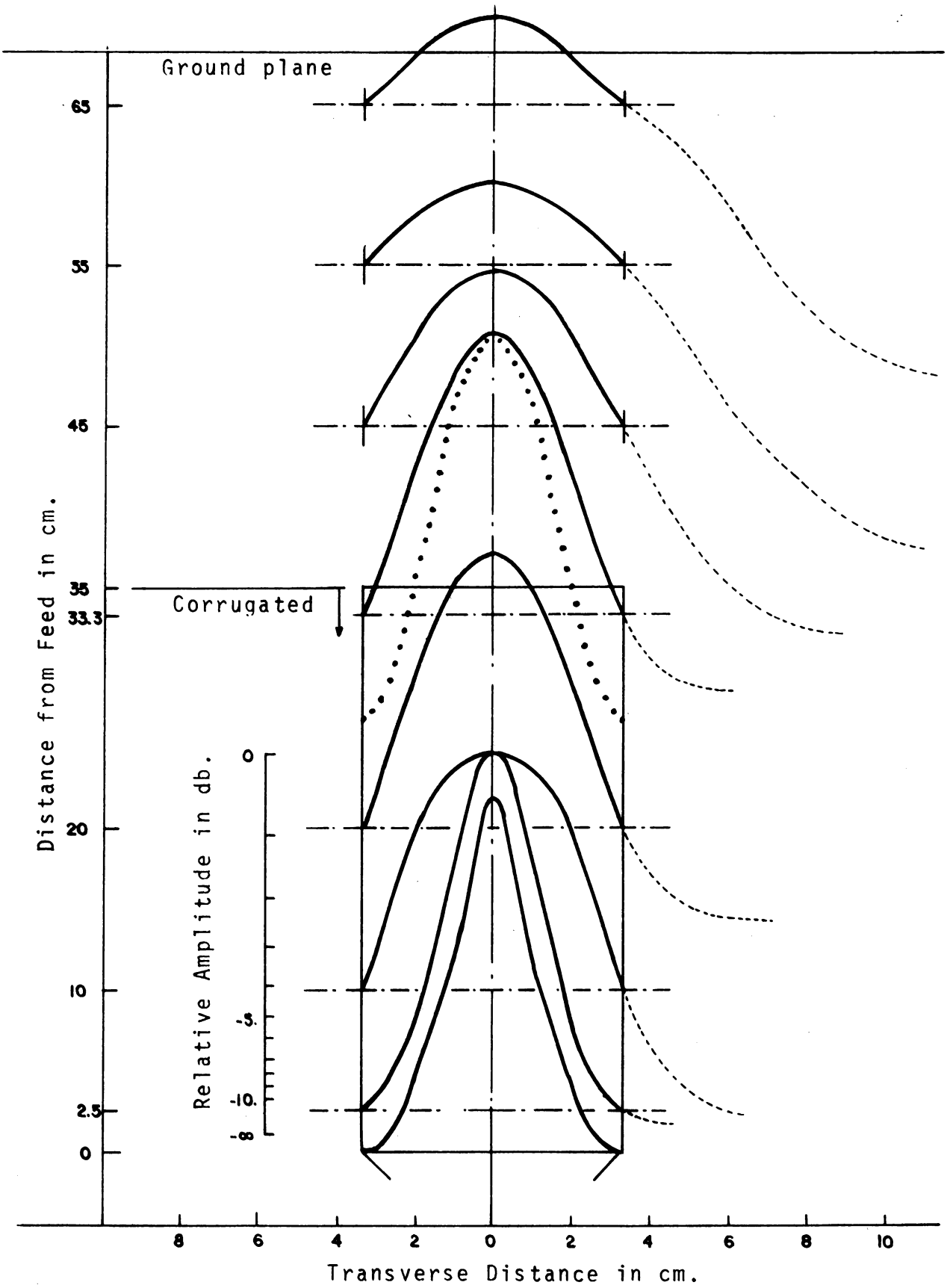

Figure 5.15b Surface Field Distribution for E_y in Transverse Direction (8 Ghz.)

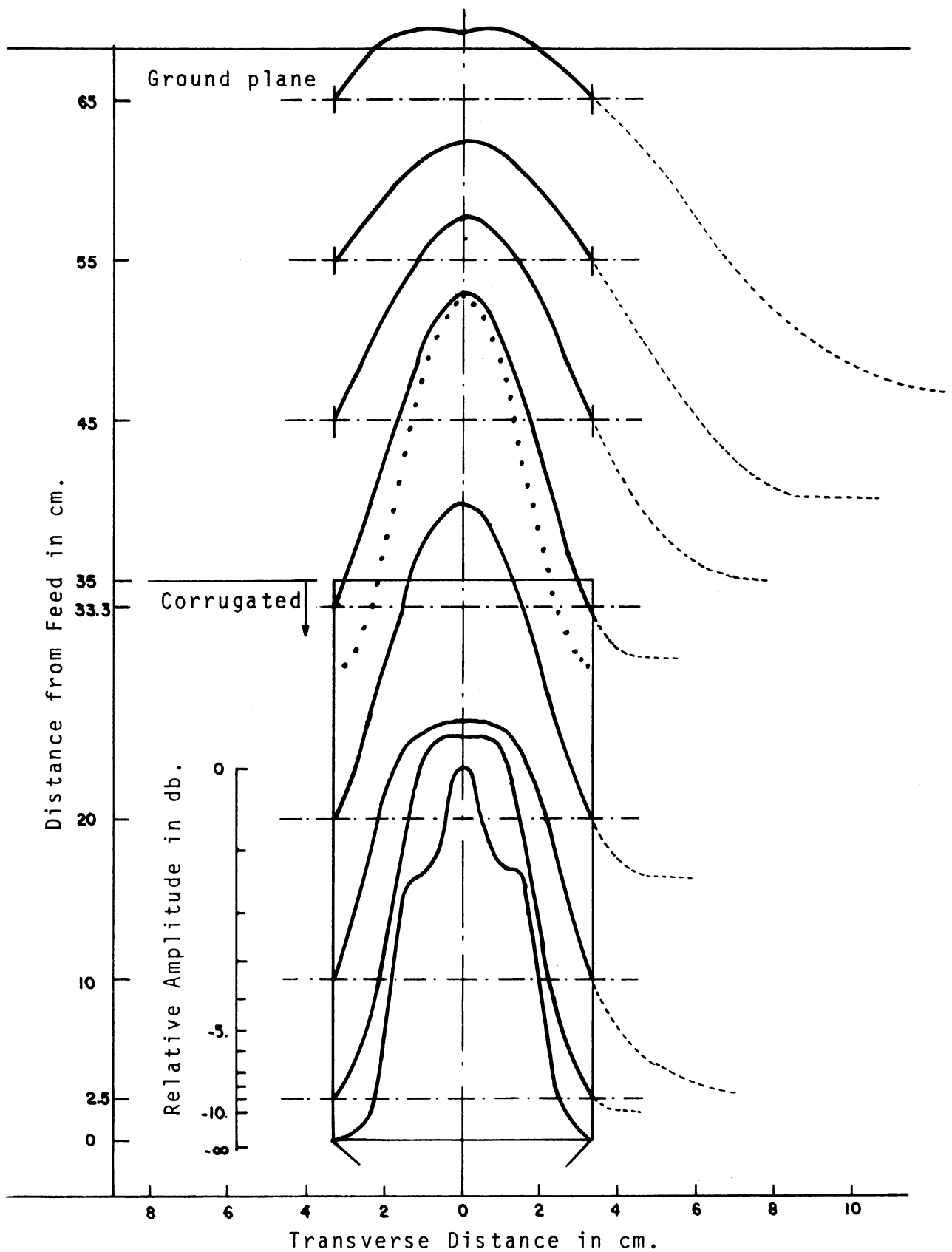

Figure 5.15c Surface Field Distribution for E_y in Transverse Direction (9 Ghz.)

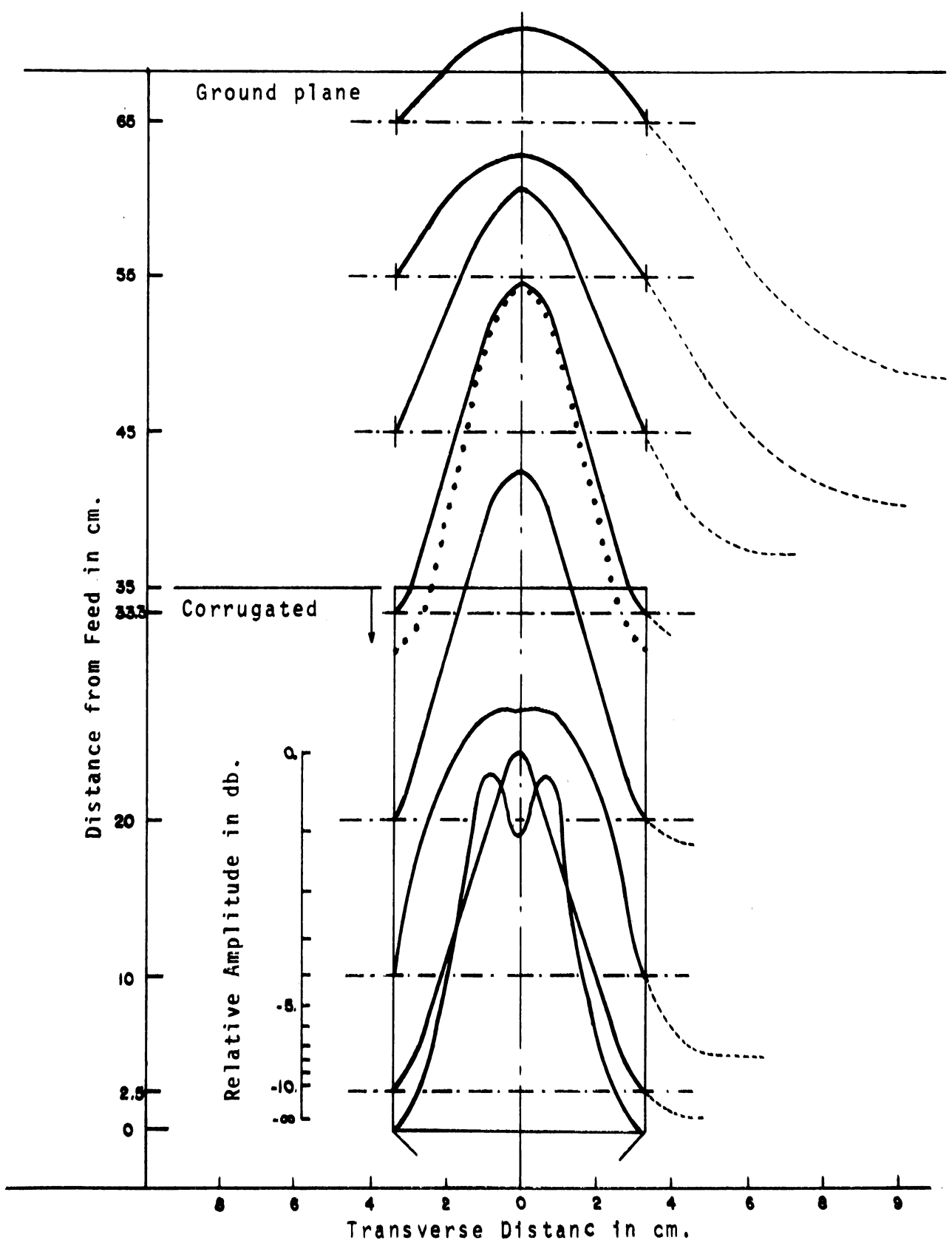

Figure 5.15d Surface Field Distribution for E_y in Transverse Direction (10 Ghz)

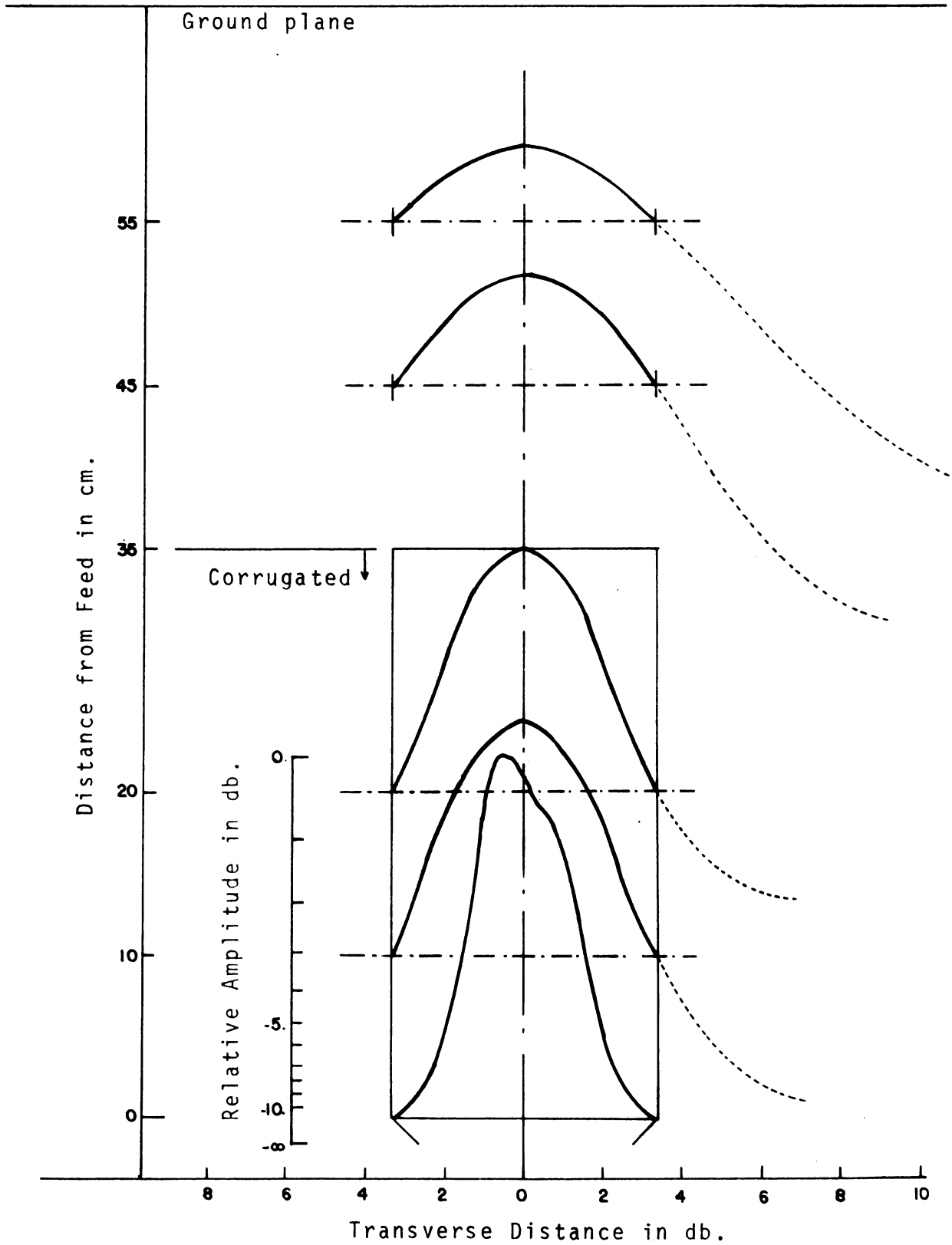

Figure 5.16a Surface Field Distribution for H_x in Transverse Direction (7 Ghz.)

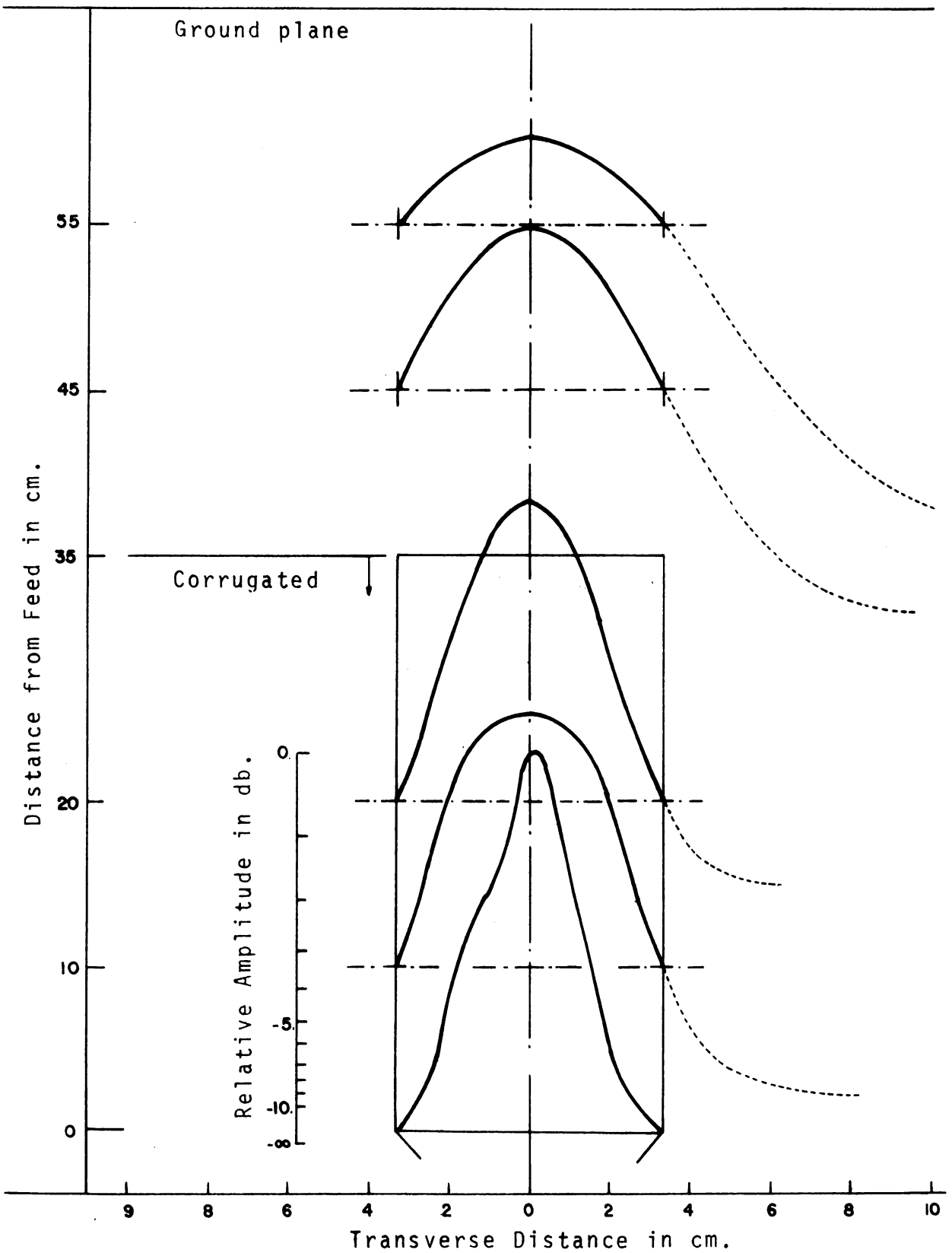

Figure 5.16b Surface Field Distribution for H_x in Transverse Direction (8 Ghz.)

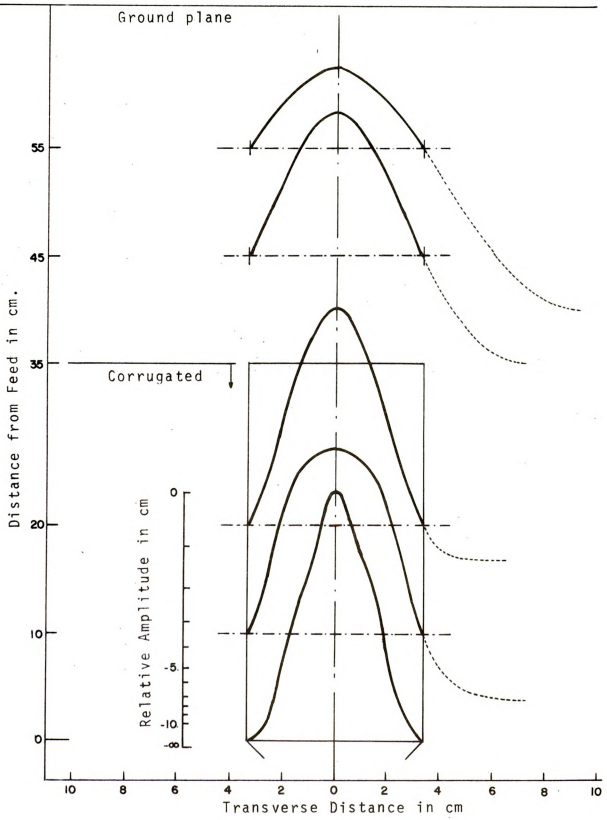

Figure 5.16c Surface Field Distribution for H_x in Transverse Direction (9 Ghz.)

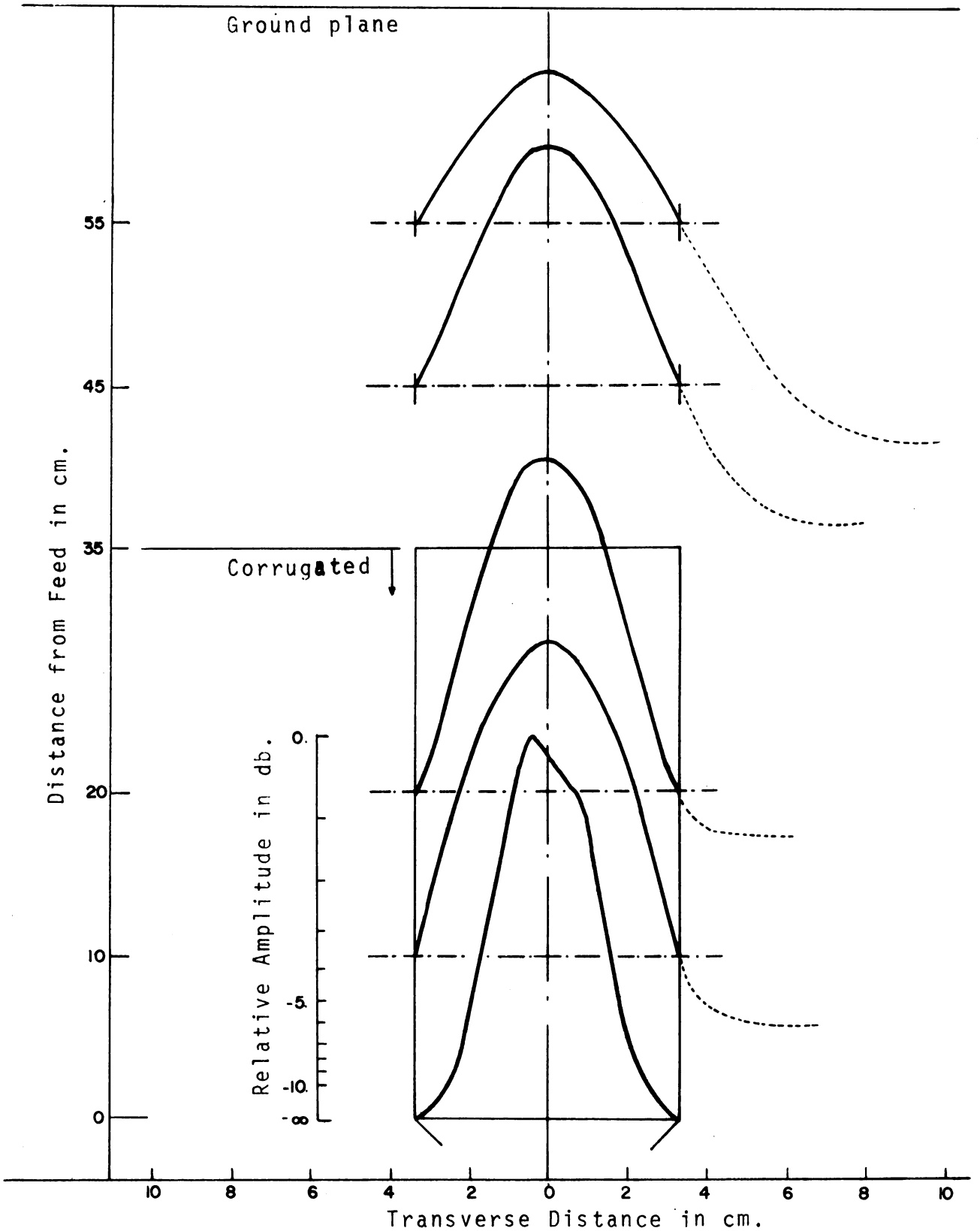

Figure 5.16d Surface Field Distribution for H_x in Transverse Direction (10 Ghz.)

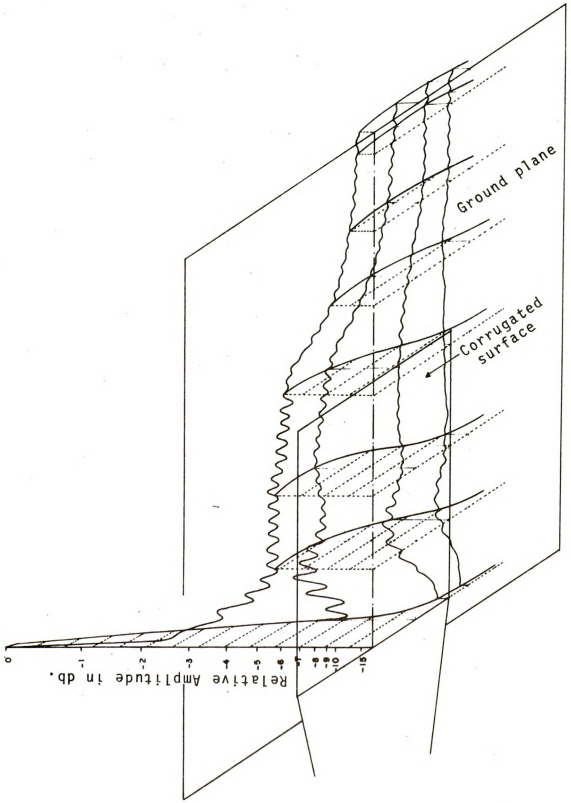

Figure 5.17a Three Dimensional Surface Field Distribution for E_y (8 Ghz.)

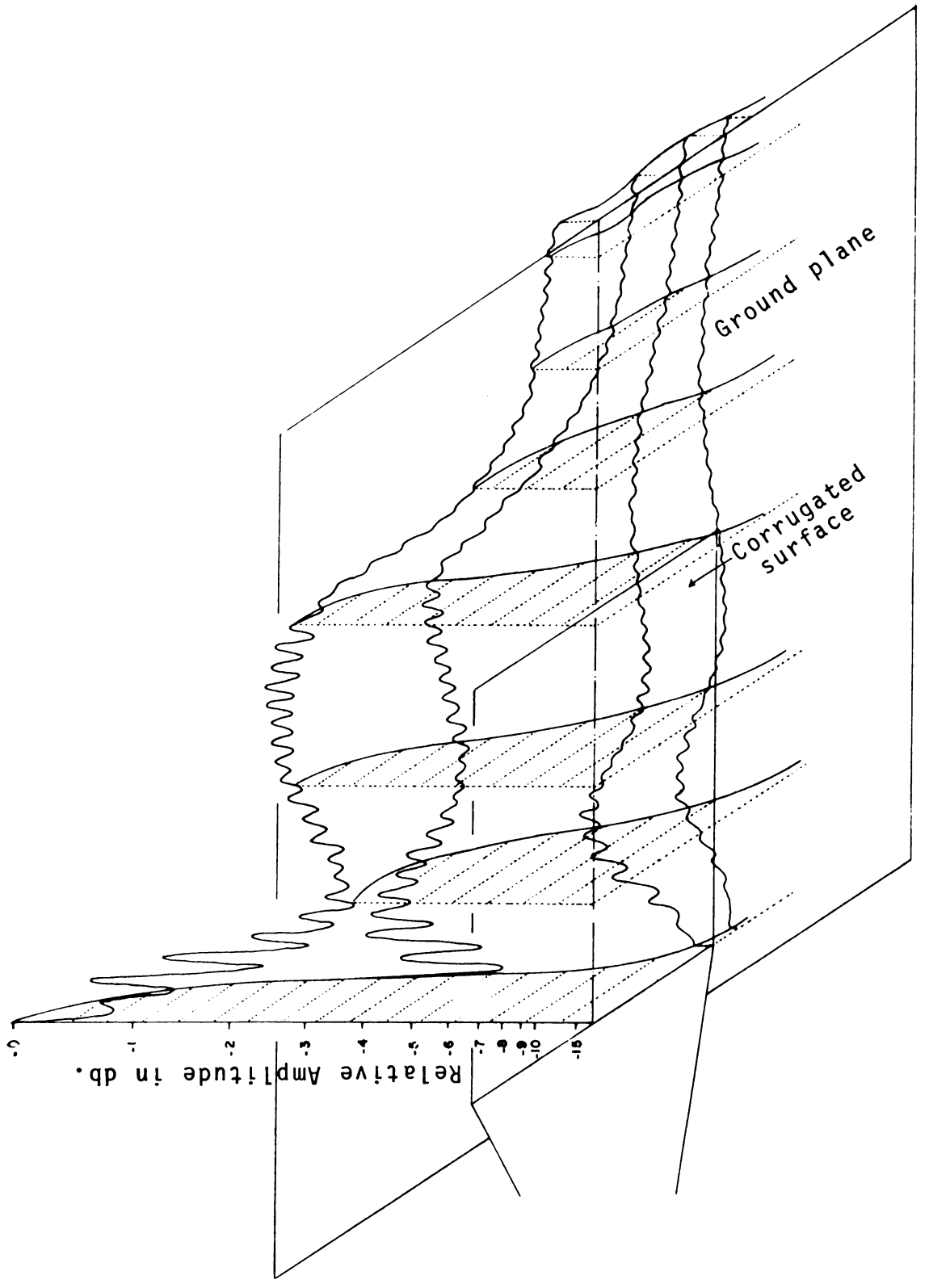

Figure 5.17b Three Dimensional Surface Field Distribution for E_y (9 Ghz.)

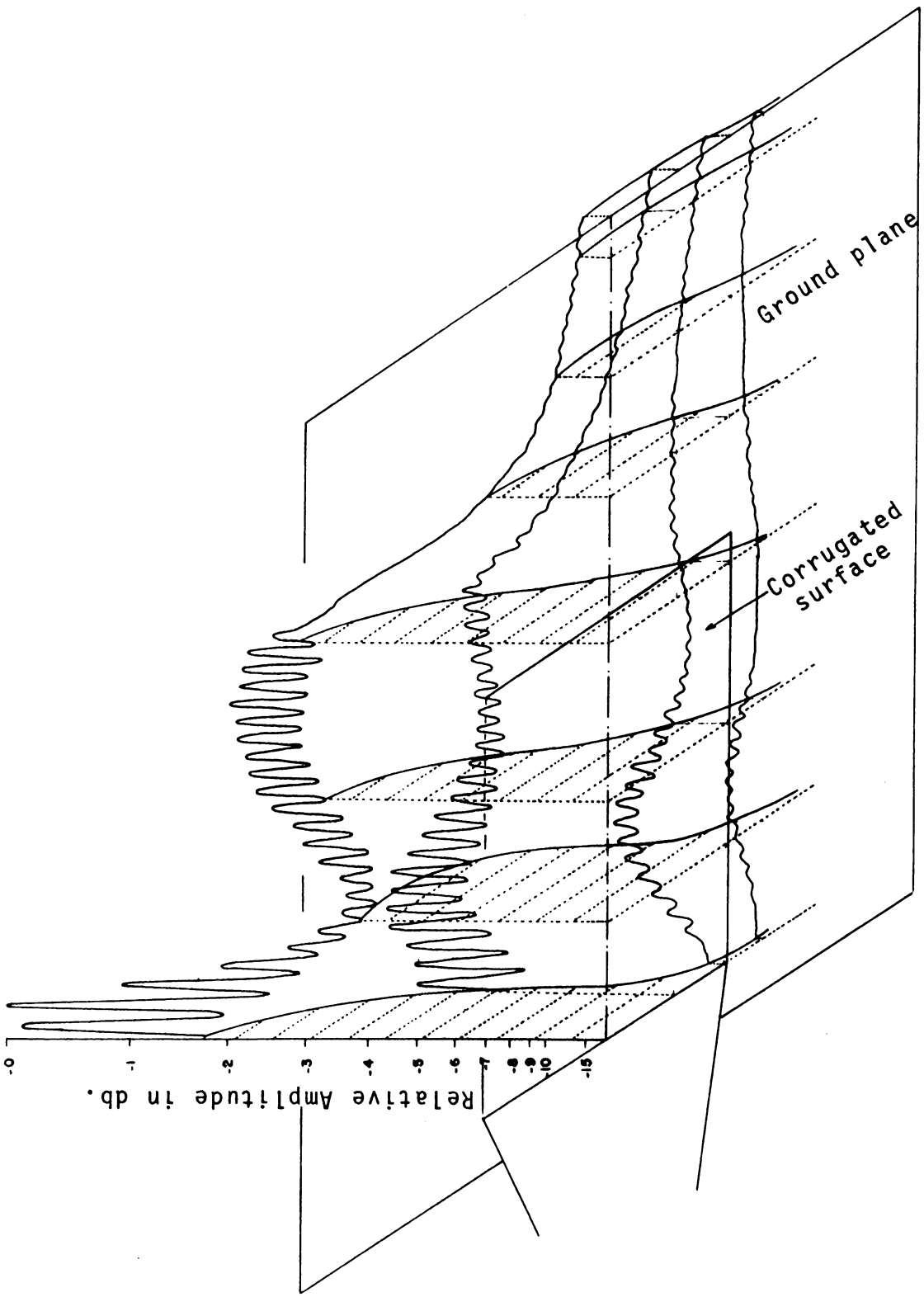

Figure 5.17c Three Dimensional Surface Field Distribution for E_y (10 Ghz.)

5.3 Radiation Patterns of a Single Radiator

For the evaluation of the antenna performance, a tapered microwave anechoic chamber was constructed based on a simple ground reflection analysis (Appendix B). The anechoic chamber has the shape of a pyramidal horn that tapers from a small transmitting end to a large rectangular test region as shown in Figure B.1.

In the anechoic chamber, it is not possible to eliminate all the reflected waves from the walls covered with microwave absorbers. Thus, for the design of the chamber, the direct path signals from the transmitter and the reflected signals from the walls are adjusted to add in phase in the quiet zone by adjusting the taper angle and the range distance. This creates a slowly varying spatial interference pattern in the test target area. This periodic perturbation can be minimized by choosing a proper cone angle and chamber dimensions.

The chamber was designed to operate for the frequency as low as 1000 Mhz. The minimum apex cone angle was chosen to be 36° for the optimum operation considering the space limitation. The theoretically predicted field variation in the horizontal cut at 1000 Mhz was below -0.25 db along the excursion of ±4 feet from the center of the sqaure area located at 12.5 feet from the transmitting end. The field variation along the axis of the chamber was calculated to be + 0.1 db in the square test region. This field variation in the chamber is comparable with the field distribution for a free space test range.

As the frequency of the operation is increased, the field variation is expected to be improved further, since the reflectivity of the microwave absorbers used in the chamber decreases to the level below

the value that is used in the calculation and in addition, the electrical dimensions of the chamber become larger. In order to reduce the possible back scattering from the rear wall, the rear wall was shaped in a slightly angled wedge to divert the reflected waves away from the test area.

For the measurement of the radiation patterns, the test antenna was used as a receiving antenna and a conical horn antenna as a transmitting antenna. For the correct beam direction, a critical antenna alignment between the test antenna and the transmitting antenna was necessary. At first, the antennas were very carefully aligned by using a surveying level. Later it was found that the use of a simple laser beam proved to be more than satisfactory.

Figures 5.18 a-b are the E-plane radiation patterns of a single corrugated antenna over the frequency range of 7 Ghz. to 10.5 Ghz. In Figure 5.18, the solid line is the measured pattern and the dotted line is the theoretically calculated pattern. The measured beam tilts from the true end-fire direction, which are 8° to 10.5°. The deviation of 1° is within the accuracy of antenna alignment. The measured half power beam width in the frequency range varies from 11.5° to 12.5°, which is in excellent agreement with the theory.

The H-plane patterns of a single corrugated antenna are shown in Figures 5.19a and 19b in comparison with the theoretically calculated patterns. The measured half power beam width varies from 21° at 7 Ghz. to 12.5° at 10 Ghz. The result does not agree too well with the theory. The theory predicts the half power beam width of 23° at 7 Ghz. and 16° at 10 Ghs. This disagreement may be due to the approximation made for the transverse field distribution function f(x). The H-plane patterns were

calculated with $f(x) = 1$ and $f(x) = \cos(\frac{\pi x}{w})$. The approximate distribution function $f(x) = \cos(\frac{\pi x}{w})$ gives about the same half-power beam width as that for $f(x) = 1$.

In order to see the effect of the ground plane on the beam tilt, the radiation patterns at 9 Ghz. were taken with the ground planes of various lengths attached to the corrugated surface. The measured E-plane radiation patterns are shown in Figure 5.20 with the calculated patterns. The half power beam width agrees well with the theory but there is a disagreement in the maximum beam direction. Only the trend of the beam shift agrees with the theory. An interesting fact is that on the contrary to the common belief on the trend of the beam shift that it should move toward the ground plane as the length of the ground plane increases. It was observed that as the length of the ground plane was shorted, the maximum beam direction was, in fact, shifted toward the true end-fire direction accompanied with the reduction in directivity. This deviation from the theory may be perhaps due to the currents flowing along the edges of the finite ground plane, since as the ground plane is shortened, the magnitude of the induced current on the edge of the ground plane may increase, resulting in a strong edge effect. To see the edge effect, the ground plane was completely removed from the antenna structure, and the E-plane and H-plane radiation patterns were taken. These patterns are shown in Figure 21.a and Figure 21.b. The disagreement between the experiment and the theory which did not include the edge effect is accentuated in the figures. Therefore, it is concluded that when the length of the ground plane is less than 10 wavelengths or so, the theory should include the edge currents to predict accurately the radiation pattern of a slow surface end-fire antenna. In practice, the ground plane is most likely greater than 10 wavelengths,

and the effect of the edge current may be neglected.

Figures 22a and 22b show the radiation patterns for the single radiator with various lengths of the corrugated surface. For this measurement, the total antenna length, the corrugated surface and the ground plane, was fixed to the 20.5 wavelengths at 9 Ghz, and the length of the corrugated surface was then varied by covering the surface with a conducting aluminum tape. As shown in Figure 22a, the theory and the experiment are in excellent agreement except for the side lobe levels. This excellent agreement may imply that the well defined surface wave propagates on the corrugated surface with a high launching efficiency at the aperture and that the longer the length of the ground plane is, the smaller the current is induced at the end resulting the negligible effect to the radiation pattern.

In chapter 2, it was found that when the dimension of the corrugated waveguide was adjusted to the width, a, of 2 λ_0 and the height, b, of 0.5 λ_0 the phase velocity of the fundamental wave in the guide was about equal to that on the open corrugated surface, implying the possibility of the smooth field transition at the horn aperture with the supression of feed radiation. In order to check the possibility, the height of the transition horn was reduced to 0.5 λ_0 at 9 Ghz, and the E-plane and H-plane radiation patterns were taken over the frequency range of 7 Ghz to 9.75 Ghz. Figures 5.23a and 5.23b show the measured radiation patterns with the theoretically predicted patterns in dotted lines. It is noted in the figures that the experimental radiation patterns are in excellent agreement with the theory in the maximum beam direction and the beam width. The degree of the agreement in the radiation pattern for the corrugated antenna with the modified horn is much better than

those patterns shown in Figure 5.18. This may indicate that if the dimensions of the corrugated waveguide are adjusted to the proper values using the dispersion relation in equation (2.51) so that the phase velocity in the guide is close to that on the open corrugated surface, the surface wave launching efficiency at the horn aperture may improve, resulting less feed radiation which is highly desirable for the practical end-fire antenna.

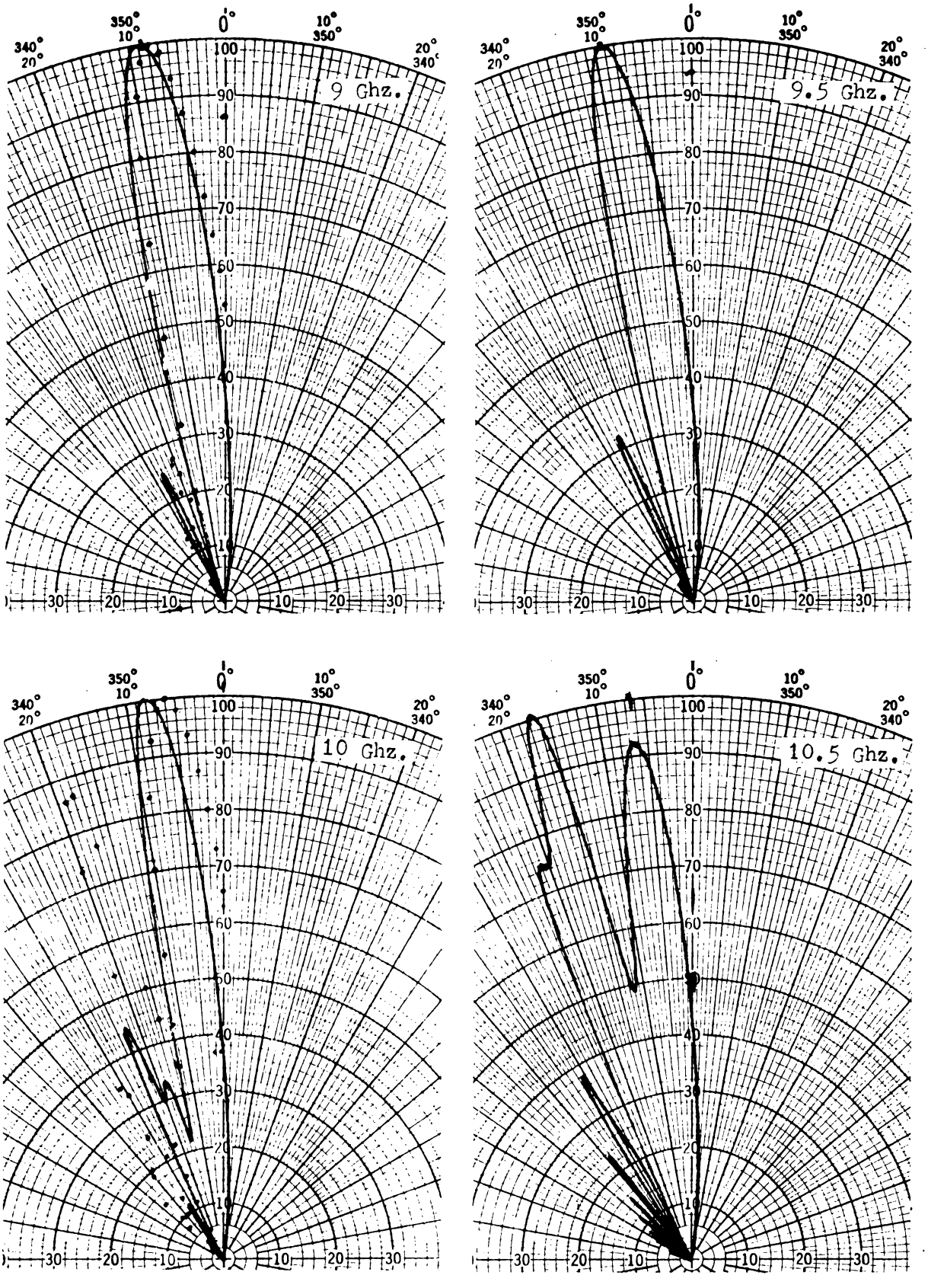

Figure 5.18b E-Plane Radiation Patterns of a Single Radiator
(9-10.5 Ghz.: ——— measured, ... calculated)

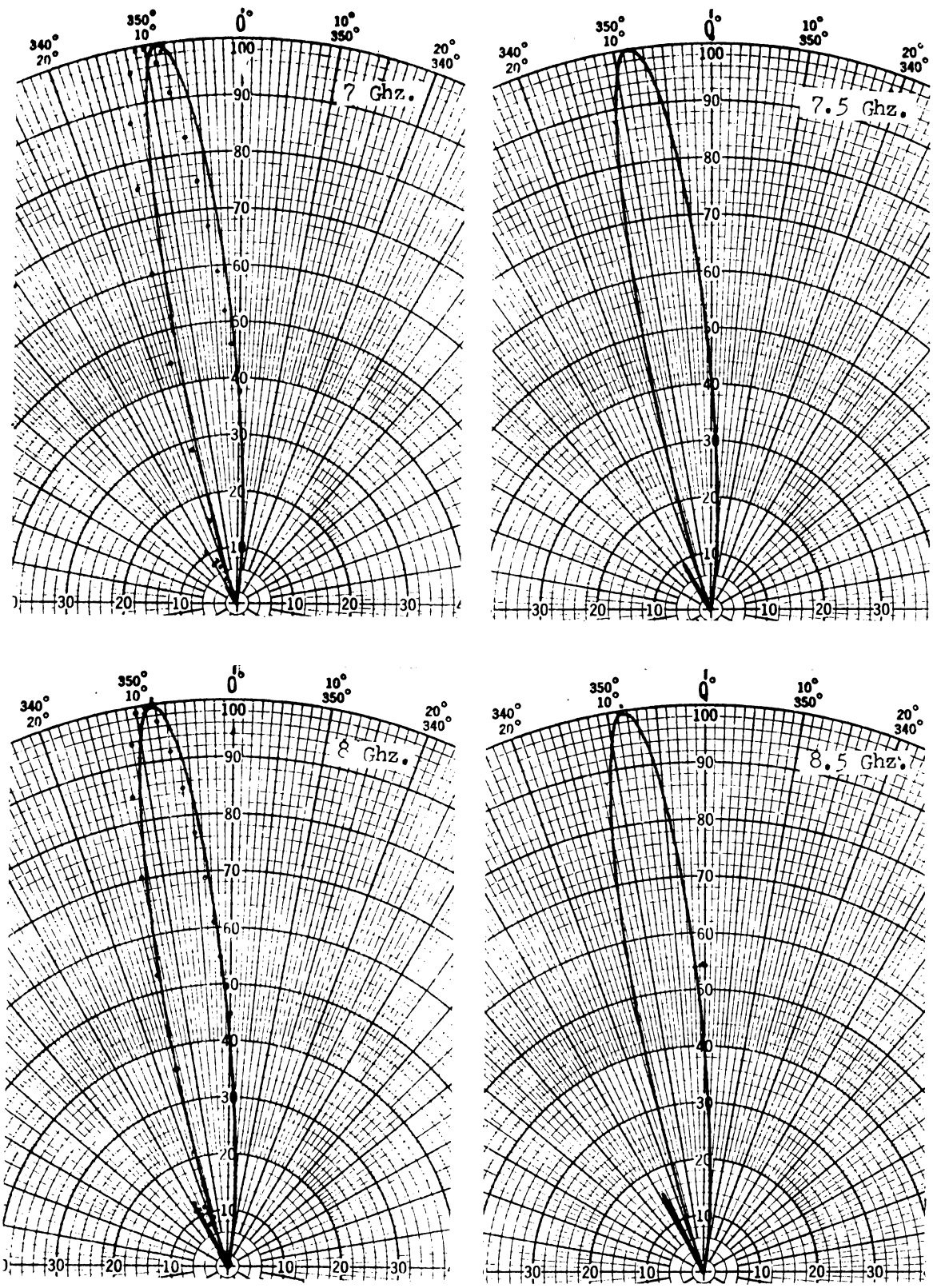

Figure 5.18a E-Plane Radiation Patterns of a Single Radiator (7-8.5 Ghz.: ——— measured, ····· calculated)

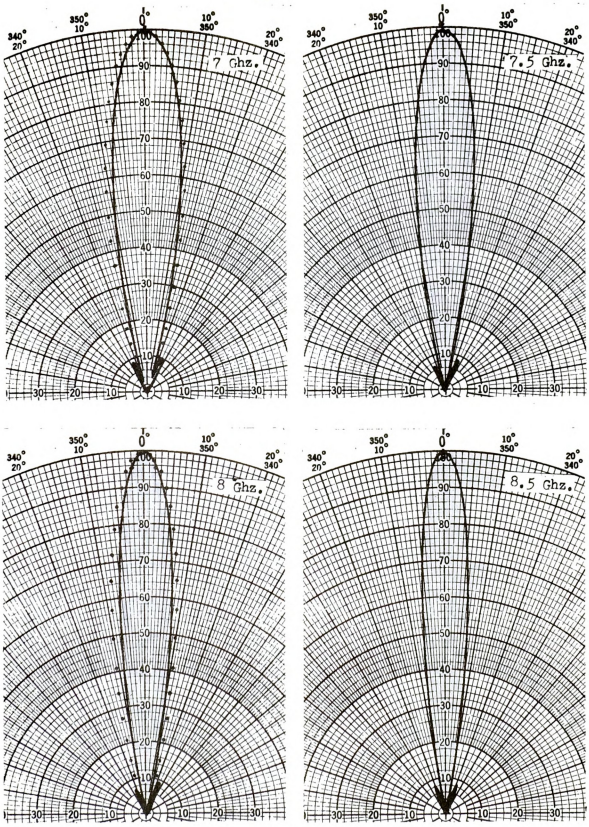

Figure 5.19a H-Plane Radiation Patterns of a Single Radiator
(7-8.5 Ghz.: ——— measured, ...calculated)

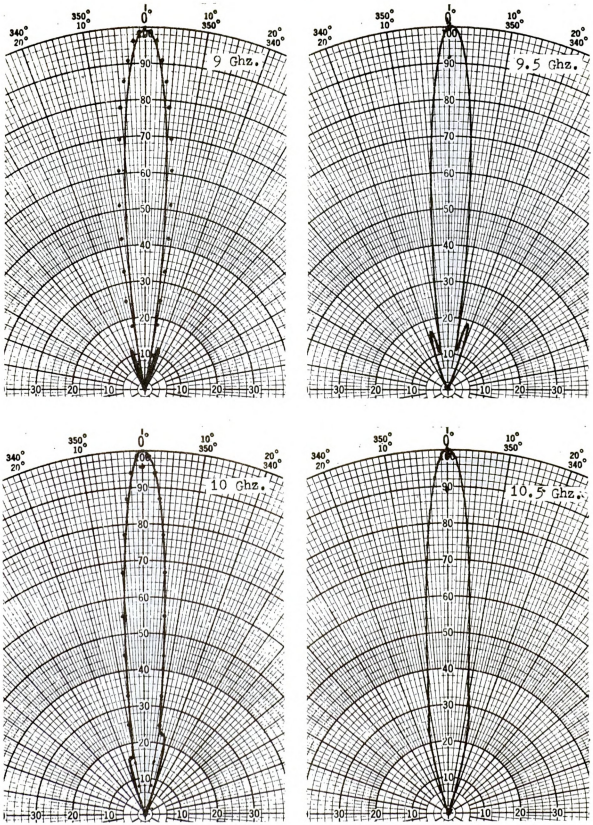

Figure 5.19b H-Plane Radiation Patterns of a Single Radiator
(9-10.5 Ghz.: _____ measured, ... calculated)

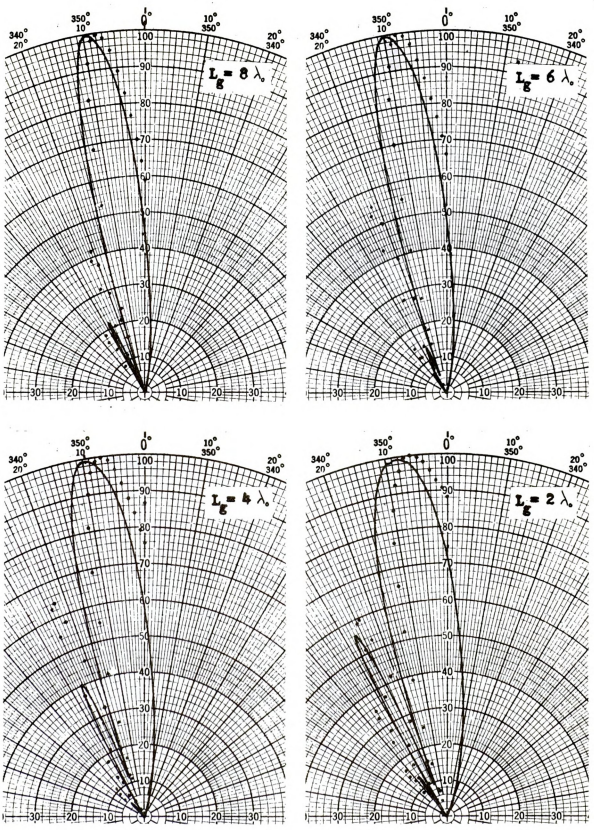

Figure 5.20 E-Plane Radiation Patterns of a Single Radiator with Different Ground Plane Length at 9 Ghz. (_____ measured, ... calculated)

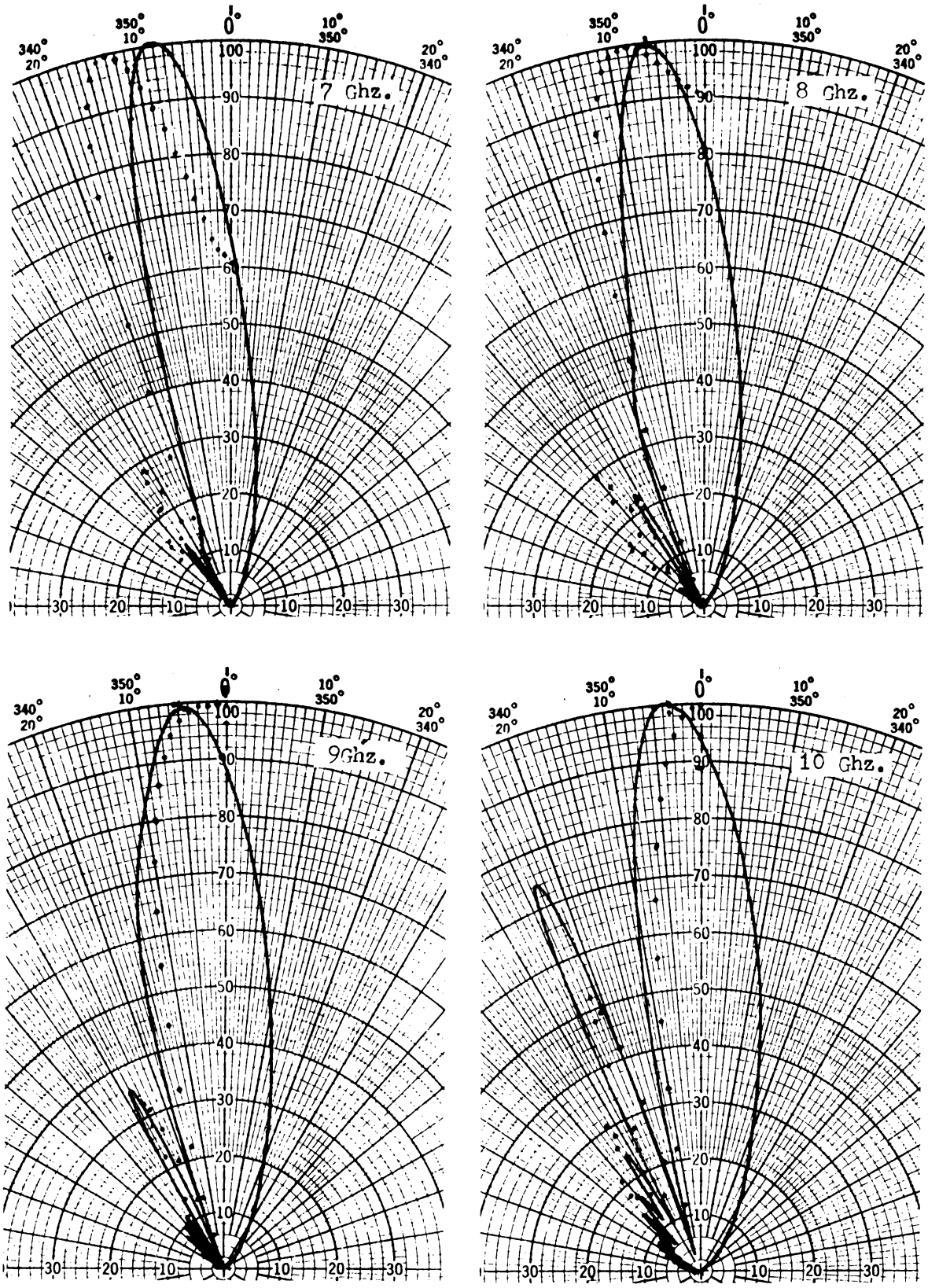

Figure 5.21a E-Plane Radiation Patterns of a Single Radiator without Ground Plane
(7-10 Ghz.: ——— measured, ····· calculated)

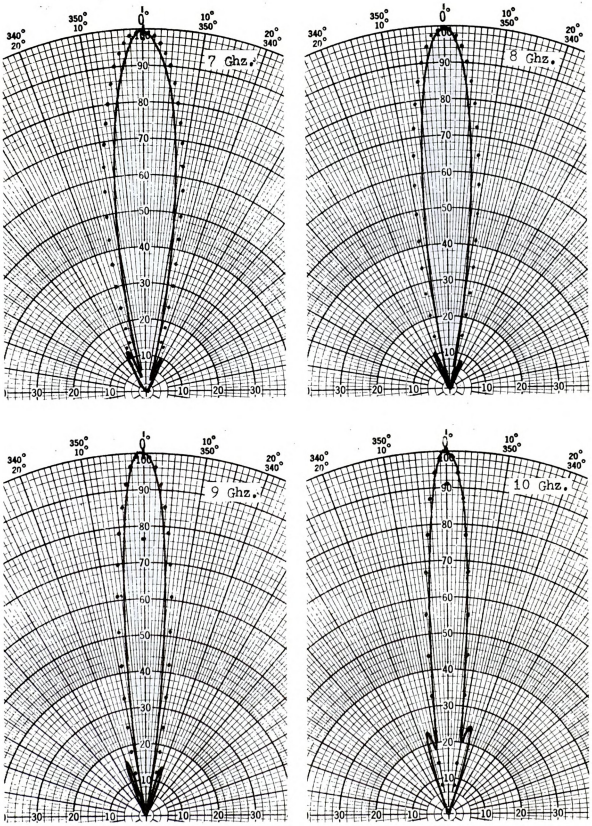

Figure 5.21b H-Plane Radiation Patterns of a Single Radiator without Ground Plane
(7-10 Ghz.: ——— measured, ... calculated)

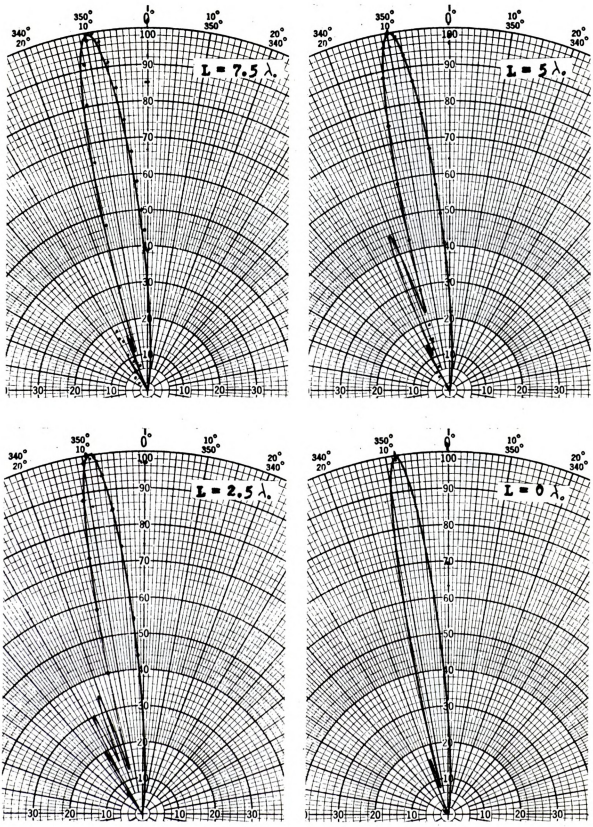

Figure 5.22a E-Plane Radiation Patterns of a Single Radiator with Different Corrugated Surface Length at 9 Ghz. (_____ measured, ····· calculated)

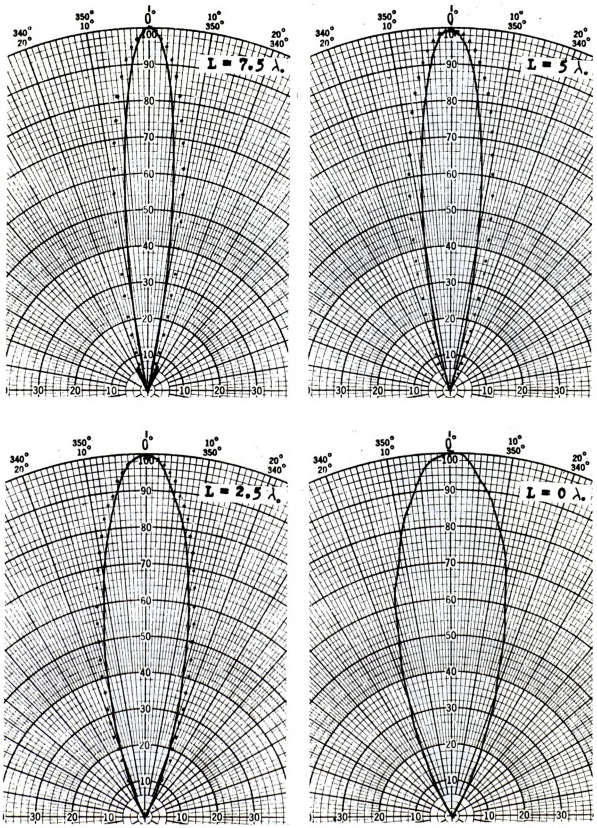

Figure 5.22b H-Plane Radiation Patterns of a Single Radiator With Different Corrugated Surface Length at 9 Ghz.
(_____ measured, ····· calculated)

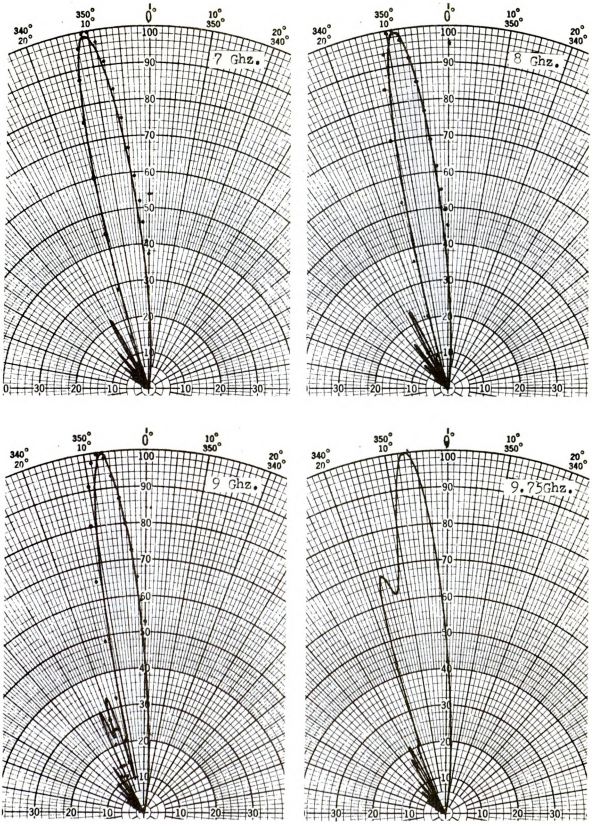

Figure 5.23a E-Plane Radiation Patterns of a Single Radiator with Modified Horn Feed
(7-9.75 Ghz.: _____ measured, ... calculated)

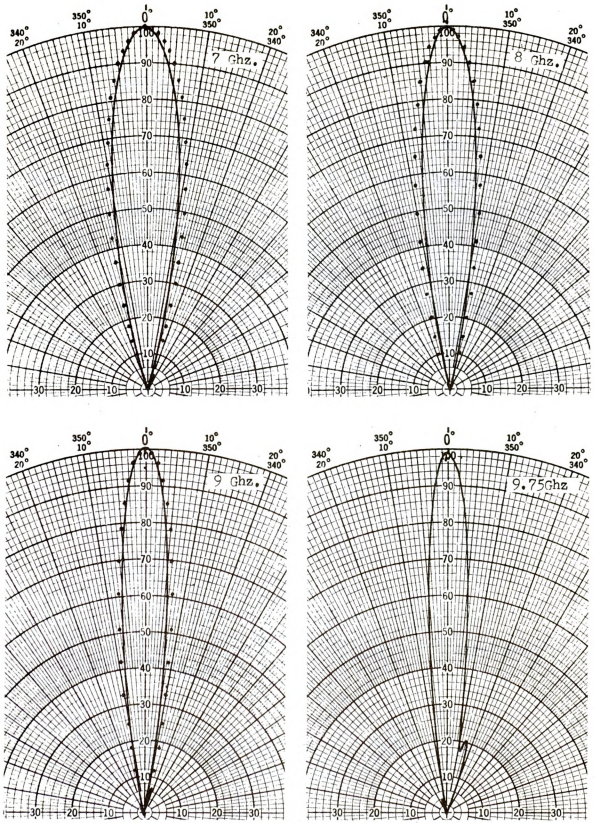

Figure 5.23b H-Plane Radiation Patterns of a Single Radiator with Modified Horn Feed
(7-9.75 Ghz.: _____ measured, ... calculated)

5.4 Input Impedance of a Single Radiator

The input impedance of the single corrugated antenna was measured using the conventional null shift method. The measured input impedance is referred to the input of the 2 inches long uniform standard rectangular waveguide connected to the corrugated rectangular waveguide in tandem. Figure 2.24 shows the input standing wave ratio for two identical corrugated antennas at the input of the antennas over the frequency range of 7 Ghz to 11 Ghz. Both antennas have almost the same input impedance. Figure 2.25 shows the plot of the input impedance on a Smith chart for antenna No. 1. The input impedance of the corrugated antenna is very well matched to the waveguide over the wide frequency range.

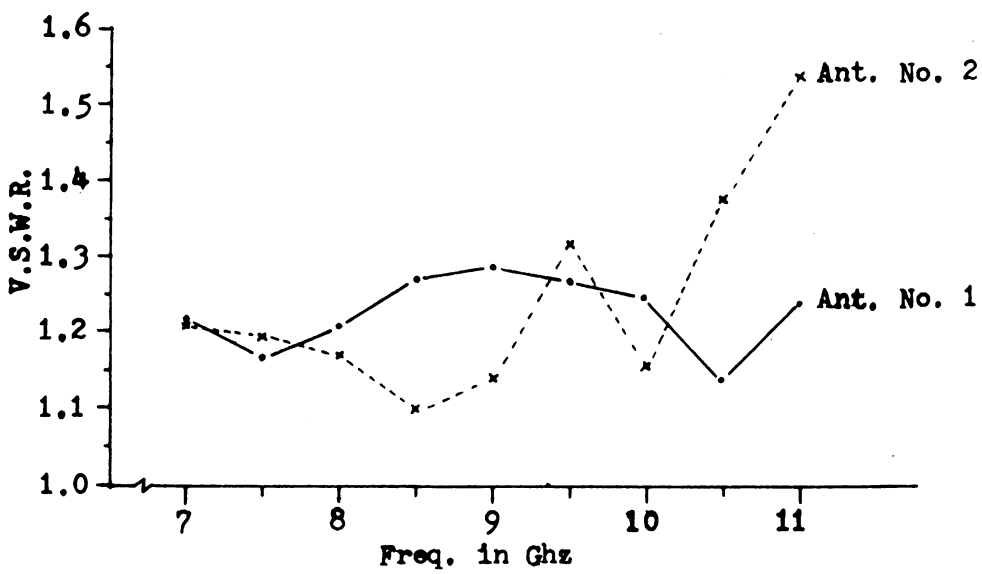

Figure 5.24 Input Standing Wave Ratio of Corrugated Antenna.

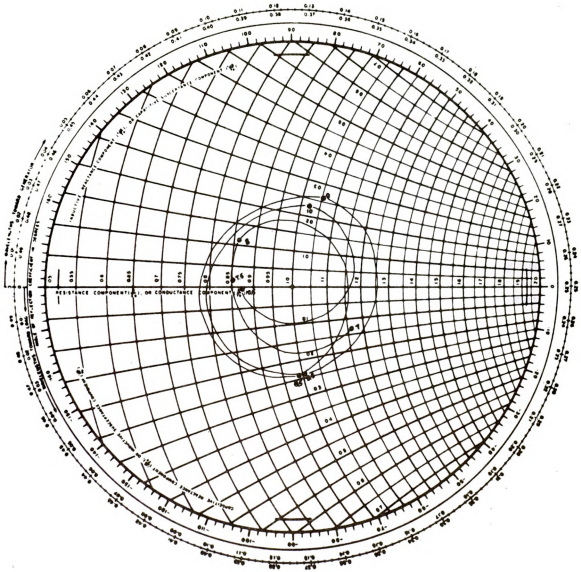

Figure 5.25 Input Impedance of Corrugated Antenna

5.5 Composit Radiator

It was found in section 5.3 that the maximum beam direction of a surface wave antenna is always tilted upward whenever the guiding surface is placed on a finite ground plane. In many applications of the end-fire antennas, the beam tilt is not desirable especially for the line of sight communication.

In order to correct the beam tilt, two identical corrugated antennas were arrayed on a wedge shape ground plane as shown in Figure 5.1. This geometry of the wedge shape ground plane simulates a part of wing or fuselage of an aircraft, and it also offers an array configuration suitable for the beam scanning. Figure 5.26 explains the roll of the pattern multiplication of the two identical beam radiating from the two antennas placed on the opposite side of the ground plane.

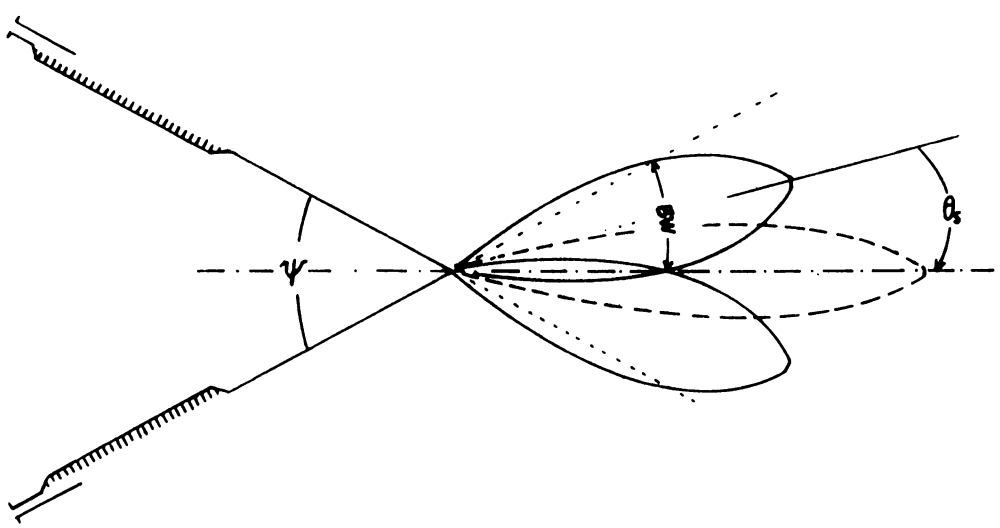

Figure 5.26 Geometry of Composite Radiator

In the Figure 5.26, it is noted that if the receiving or the transmitting power level of one of the two antennas is controlled relative to that of the other antenna, the resultant beam from the antenna array will scan in the plane perpendicular to the antenna surface. The range of the scan angle depends on the wedge angle and the beam tilt angle. It is limited by the half power beam width of the individual radiator. The maximum wedge angle for keeping the maximum beam intensity along the axial direction with low side lobe level can be shown to be the angle twice of the half power beam width. The maximum scan angle is simply related by

$$\text{Scan angle} = \frac{1}{2} \quad (\text{Wedge angle} - \text{Half power beam width})$$

For the scanning of the beam, each antenna on the wedge shape ground plane was connected to a waveguide tee through the calibrated adjustable waveguide attenuators for both channels. The E-plane radiation patterns for the antenna array were measured with Antenna No. 1 set to 0 db and Antenna No. 2 set at the different attenuation levels. Figure 5.27 shows the radiation patterns for the antenna array of 20° wedge angle, and Figure 5.28 shows those for the antenna array of 30° wedge angle. Figure 5.29 is the H-plane radiation patterns of the antenna array of wedge angle of 20° with equal power level on both of the channels. Figure 5.30 shows the photograph of the antenna array in the anechoic chamber for the radiation pattern measurement. Figure 5.31 is the surface field measurement system for a single corrugated antenna.

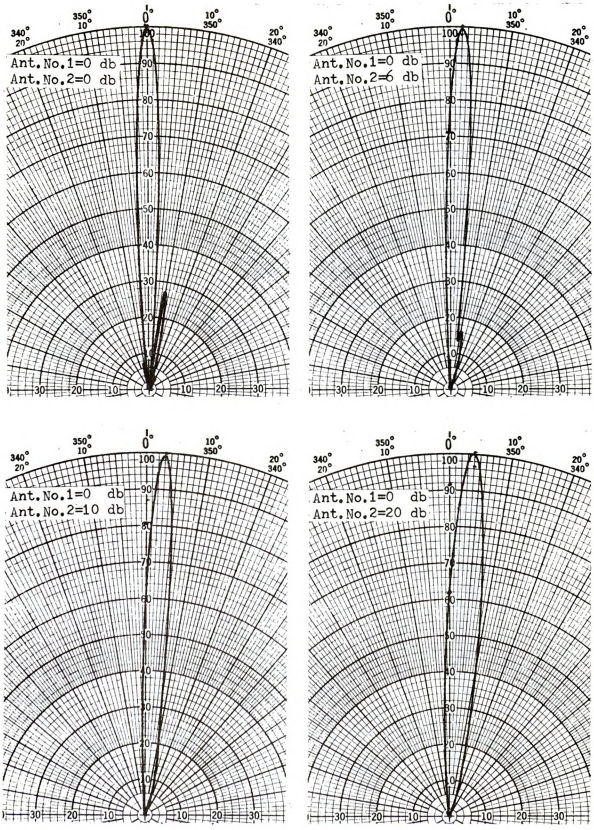

Figure 5.27a E-Plane Radiation Patterns of Composite Radiator with Wedge Angle 20° for Beam Scanning at 7 Ghz.

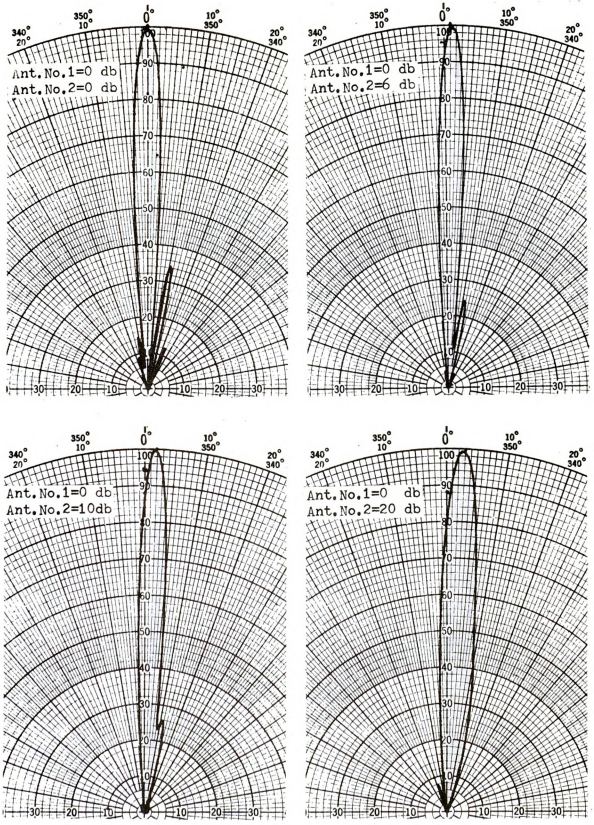

Figure 5.27b E-Plane Radiation Patterns of Composite Radiator with Wedge Angle 20° for Beam Scanning at 8 Ghz.

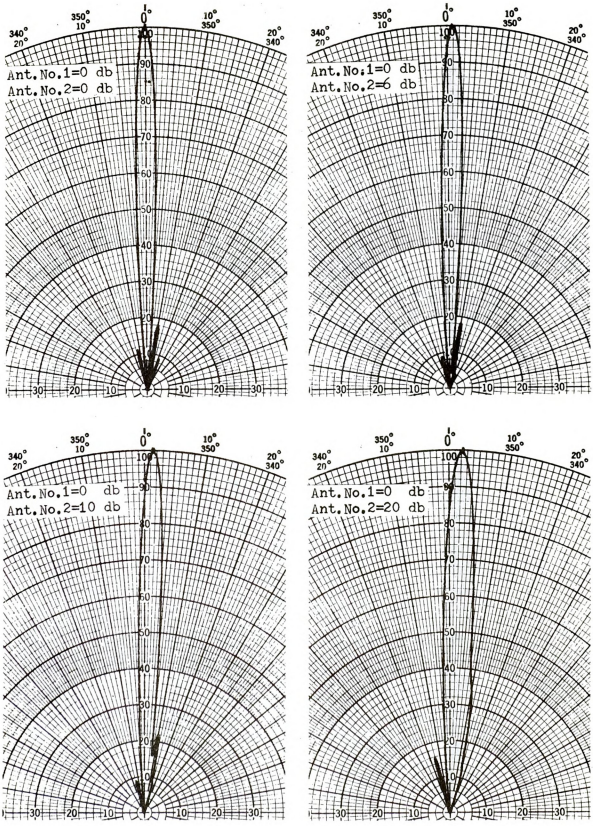

Figure 5.27c E-Plane Radiation Patterns of Composite Radiator with Wedge Angle 20° for Beam Scanning at 9 Ghz.

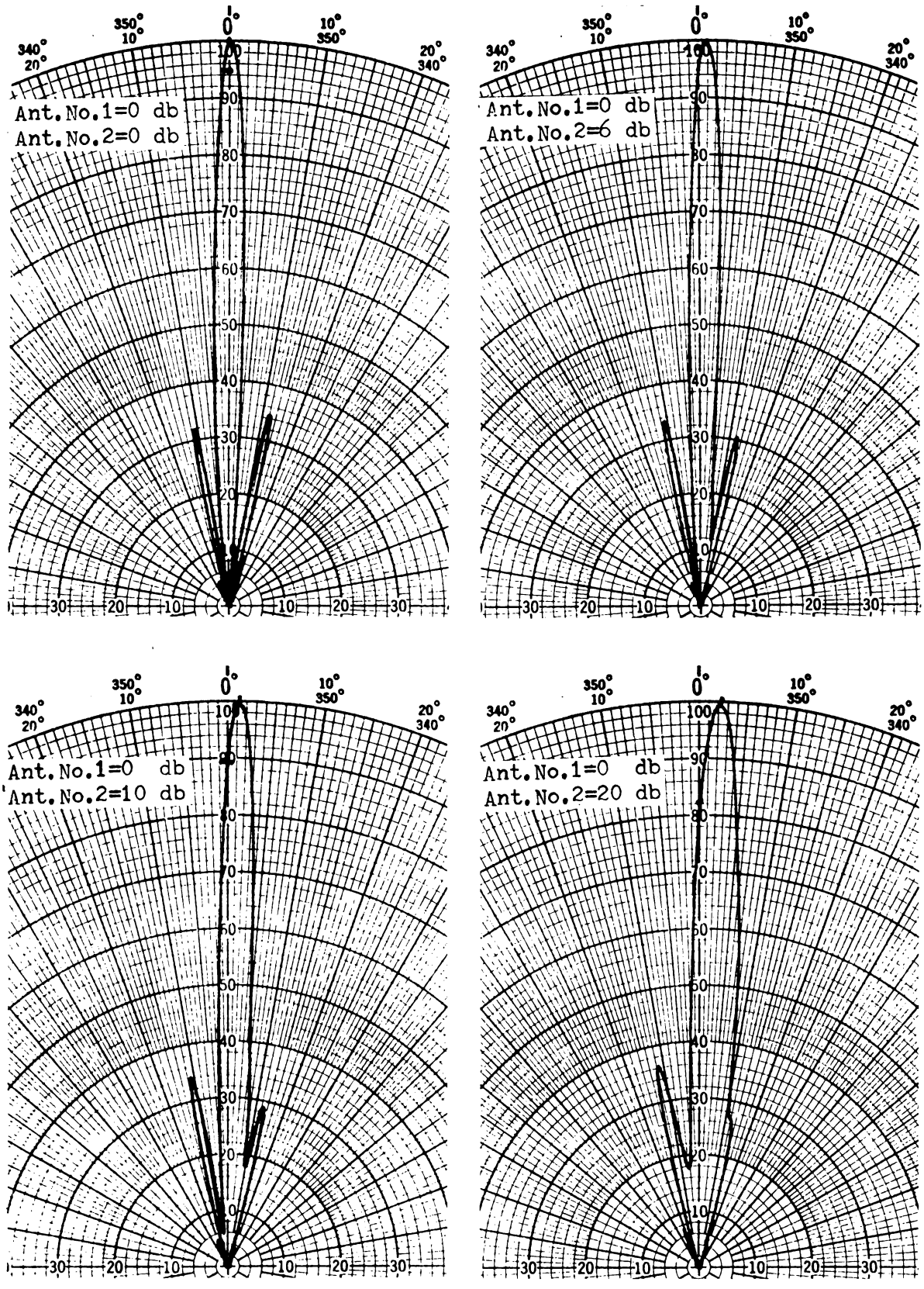

Figure 5.27d E-Plane Radiation Patterns of Composite Radiator with Wedge Angle 20° for Beam Scanning at 10 Ghz.

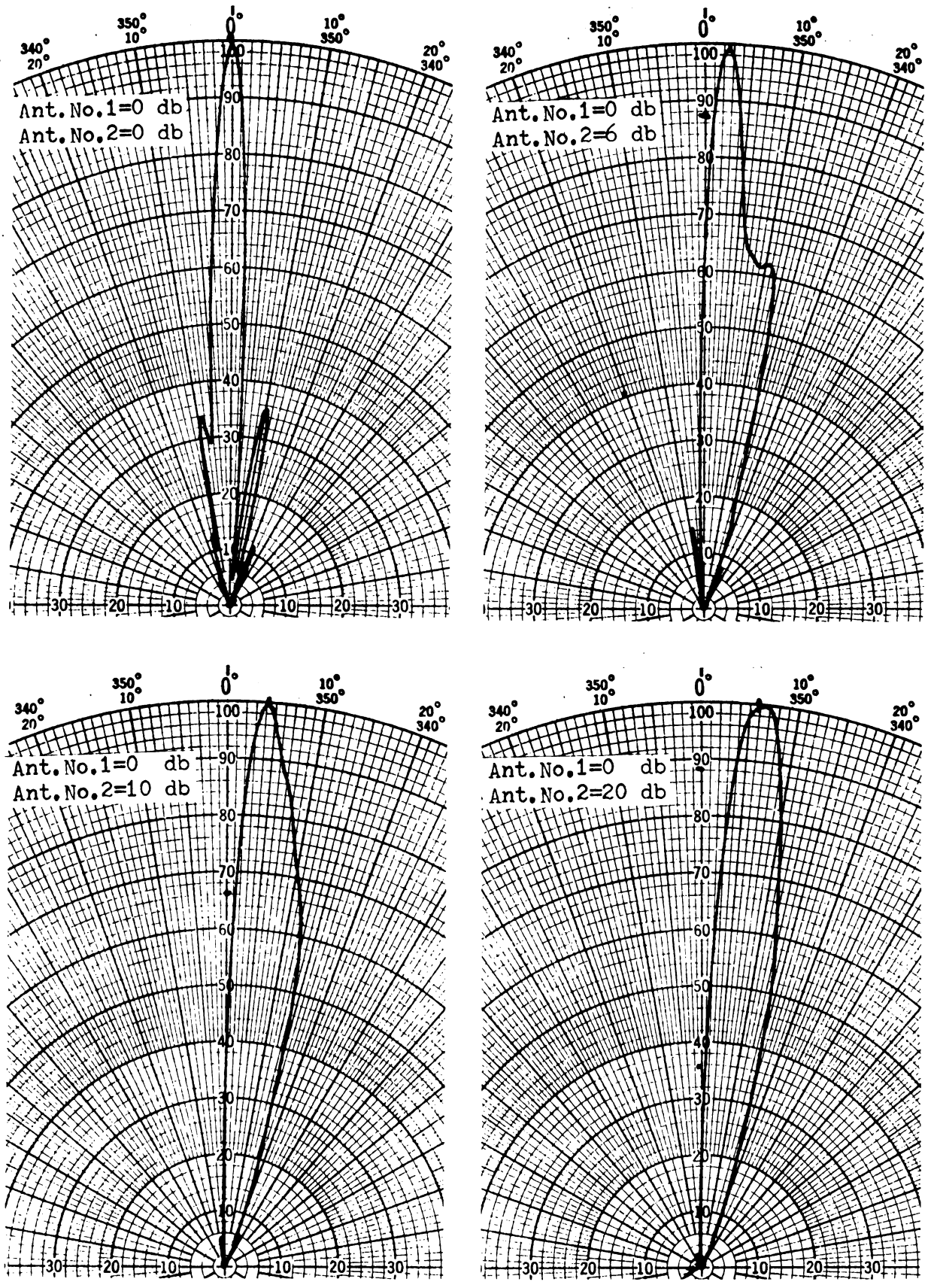

Figure 5.28a E-Plane Radiation Patterns of Composite Radiator with Wedge Angle 30° for Beam Scanning at 7 Ghz.

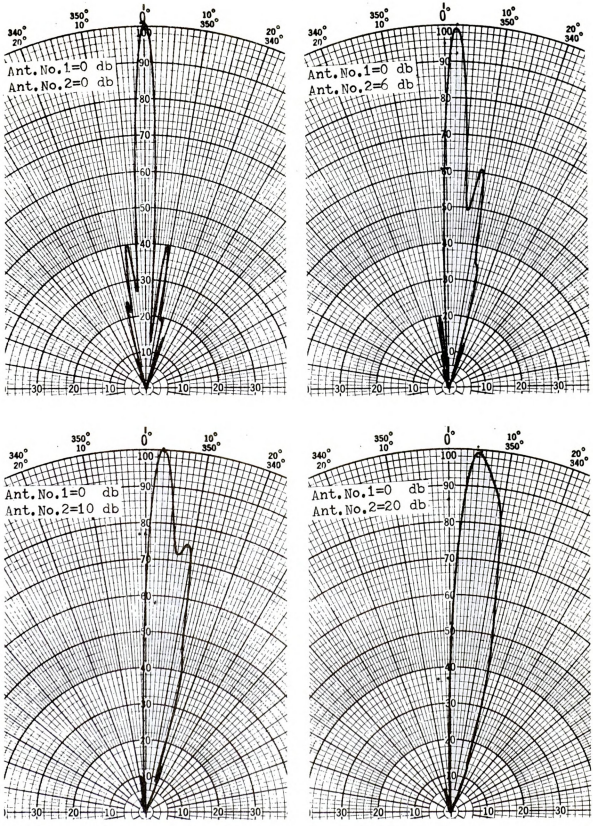

Figure 5.28b E-Plane Radiation Patterns of Composite Radiator with Wedge Angle 30° for Beam Scanning at 8 Ghz.

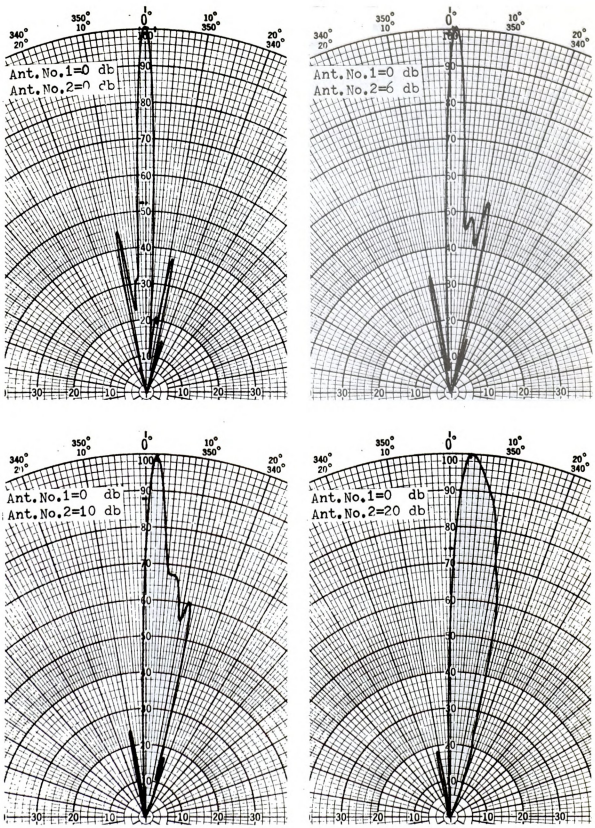

Figure 5.28c E-Plane Radiation Patterns of Composite Radiator with Wedge Angle 30° for Beam Scanning at 9 Ghz.

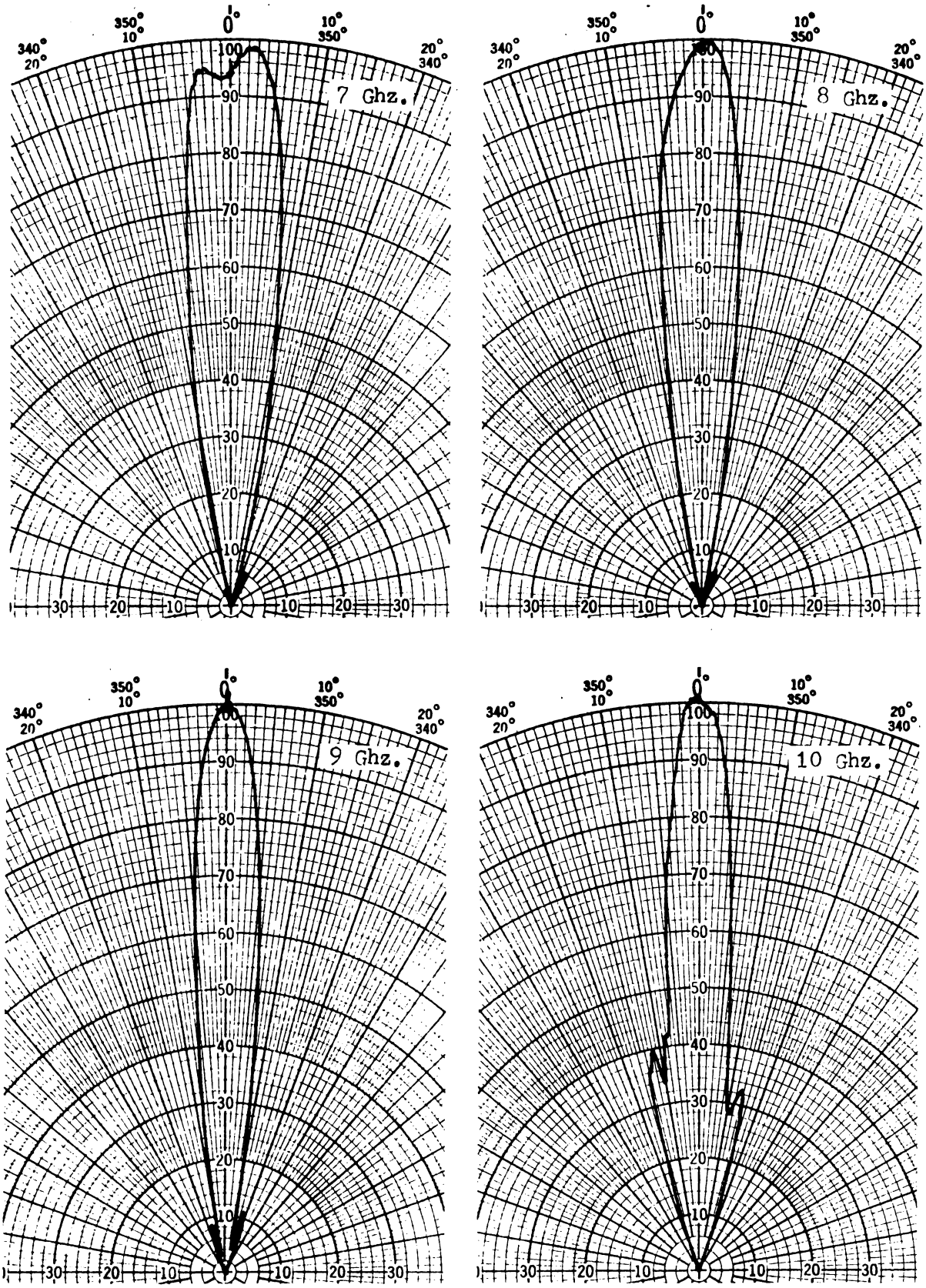

Figure 5.29 H-Plane Radiation Patterns of Composite Radiator with Wedge Angle 20° and Equal Power Level on Both Radiators

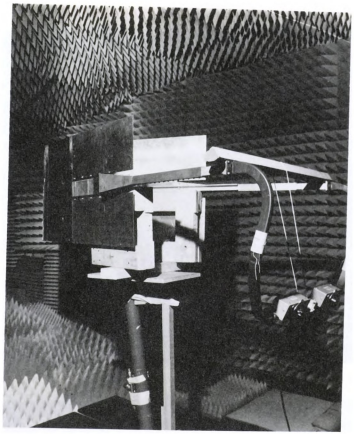

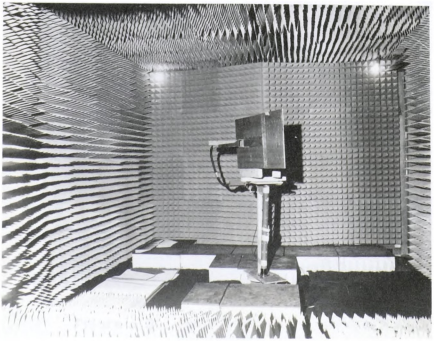

Figure 5.30 Photographs of Corrugated Antenna Array in Anechoic Chamber

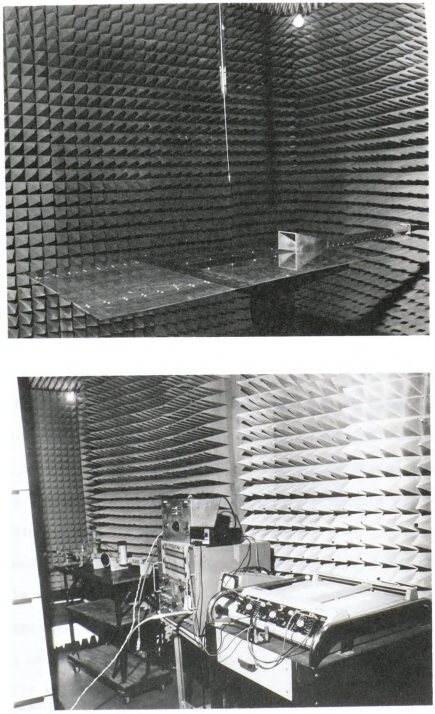

Figure 5.31 Photograph of Surface-Field Measurement System.

5.6 Conclusion

An approximate theoretical analysis on the propagation and radiation of surface waves guided on a flat corrugated surface mounted on a finite ground plane has developed, and an extensive experimental investigation has been performed to conform the validity of the approximate analysis and to develop scannable flush mounted end-fire antenna.

In the analysis, it was found that a surface wave can be efficiently launched on a finite corrugated surface by controlling the width of the corrugated rectangular waveguide with keeping the waveguide. to a minimum height, and that a slow surface wave can be guided on a finite corrugated surface extended from the bottom wall of a corrugated rectangular waveguide.

The experimental investigation confirmed that a corrugated surface with finite dimensions does support slow surface waves, and the waves were found to propagate axially confining most of the energy along the center line of the guiding surface. For the effective surface wave launcher, a bottom wall corrugated rectangular waveguide was found to be very efficient and a simple device.

It was found that the inevitable beam tilt due to the finite ground plane can be utilized in the beam scanning by arraying two identical surface wave antennas on a wedge shaped ground plane and by controlling the power level of each antenna. The maximum scan angle are determined by the beam tilt angle and the wedge angle.

From the theoretical analysis and the experimental results a conceptual flush mounted end-fire antenna may have the geometry shown in Figure 5.32.

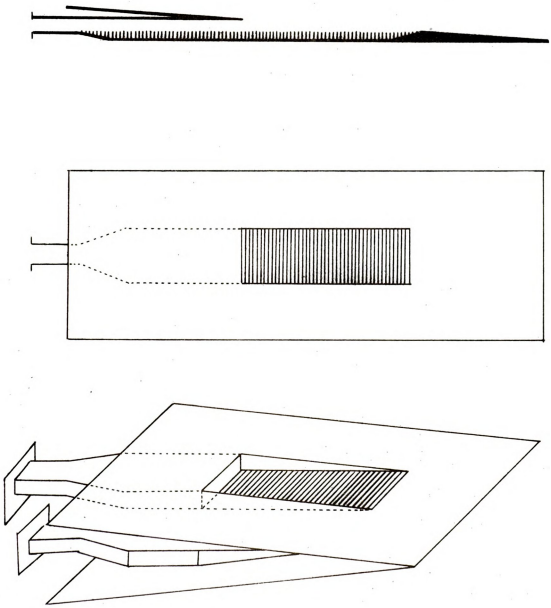

Figure 5.32 A Flush Mounted Surface Wave Antenna

REFERENCES

REFERENCES

1. Sommerfeld, A., "Über die Ausbreitung der Wellen in der drohtlosen Telegraphis", Annallen der physik, 4th Series, 28, p. 669, 1909, and 4th Series, 81, p. 1135, 1926.

2. Zenneck, J., "Über die Fortpflanzung ebener elektromagnetischer Wellen Langs einer ebenen Leiberflache und ihre Beziehung zur drahtlosen Telegraphie", Annalen der physik, 23, pp. 846-866, Sept. 1907.

3. Schelkunoff, S.A., "Anatomy of Surface Waves", IRE Trans. AP-7, pp. S 133-139, Dec. 1959.

4. Goubau, G., "Waves on Interfaces", IRE Trans. AP-7, pp. S 140-146, Dec. 1959.

5. Barlow, H.M., "Surface Waves Supported by Cylindrical Surfaces", IRE Trans. AP-7, pp. S 147-153, Dec. 1959.

6. Brown, J., "Some Theoretical Results for Surface Wave Launcher", IRE Trans. AP-7, pp. S 169-174, Dec. 1959.

7. Barlow, H.M. and Cullen, A.L., "Surface Wave", Proc. IEE., Vol. 100, Part 3, No. 68, pp. 329-347, Nov. 1953.

8. Barlow, H.M. and Karbowiak, A.E., "An Investigation of the Characteristics of Cylindrical Surface Waves", Proc. IEE., Vol. 100, Part 3, No. 68, pp. 321-328, Nov. 1953.

9. Brown, J., "The Type of Wave Which May Exist Near a Guiding Surface", Proc. IEE., Vol. 100, Part 3, No. 68, pp. 363-364, Nov. 1953.

10. Tamie T. and Oliner, A.A., "Guided Complex Waves, Part I, Fields at an Interface", Proc. IEE., Vol. 110, No. 2, pp. 310-324, Feb. 1963.

11. Brillouin, L., "Wave Guides for Slow Waves", J. Appl. Phys., Vol. 19, pp. 1023-1041, Nov. 1948.

12. Walkinshaw, W., "Theoretical Design of Linear Accelerator for Electrons", Proc. Phy. Soc., Vol. 345, pp. 249-254, Sept. 1948.

13. Shersby-Harvie, R.B.R., "Travelling Wave Linear Accelerators", Proc. Phy. Soc., Vol. 345, pp. 255-264, Sept. 1948.

14. Rotman, W., "A Study of Simple Surface Corrugated Guide", Proc. IRE., Vol. 39, pp. 952-959, Aug. 1951.

15. Hurd, R.A., "The Propagation of An Electromagnetic Wave Along An Infinite Corrugated Surface", Can. J. Phy., Vol. 32, No. 12, pp. 727-734, Dec. 1954.

16. Whitehead, E.A.N., "The Theory of Parallel-Plate Media for Microwave Lenses", Proc. IEE. 98, Part III, No. 51, pp. 133-140, 1951.

17. Feodora Berz, L., "Reflection and Refraction of Microwaves at a Set of Parallel Metalic Plates", Proc. IEE. 98, Part III, No. 51, pp. 47-55, 1951.

18. Hurd, R.A. and Gruenberg, H., "H-Plane Bifurcation of Rectangular Waveguides", Can. J. Phy., Vol. 32, pp. 694-701, Nov. 1954.

19. Mittra, R., "Relative Convergence of the Solution of a Doubly Infinite Set of Equations", J. Res. NBS, Vol. 67D, No. 2, pp. 245-254, Mar.-Apr. 1963.

20. Karjala, D.S. and Mittra, R., "Scattering at the Junction of Two Semi-Infinite Parallel-Impedance Plane Wave Guides", Can J. Phy., Vol. 43, pp. 849-854, May 1965.

21. Karjala, D.S. and Mittra, R., "Scattering by a Semi-Infinite Impedance Strip in a Waveguide", App. Sci. Res., Section B, Vol. 12, pp. 157-164, 1965.

22. Mittra, R., Lee,S.W., and Vanblaricum, G.F., "A Modified Residue Calculus Technique", Int. J. Engng, Sci., Vol. 6, pp. 395-408, 1968.

23. Mittra, R. and Laxpati, S., "Propagation in a Wave Guide with Glide Reflection Symmetry", Can. J. Phy., Vol. 43, pp. 353-373, Feb. 1965.

24. Mittra, R. and Lee, S.W., Analytical Techniques in the Theory of Guided Waves, Macmillan, New York, New York, 1971.

25. Goubau, G., "Surface Waves and Their Application to Transmission Lines", J. App. Phy., Vol. 21, pp. 1119-1128, 1950.

26. Tai, C.T., "The Effect of a Grounded Slab on the Radiation From a Line Source", J. App. Phys. Vol. 22, pp. 405-414, 1951.

27. Whitmer, R. M., "Fields in Non-metallic Waveguides", Proc. IRE., Vol. 36, p. 1105, 1948.

28. Goubau, G., "On the Excitation of Surface Waves", Proc. IRE, Vol. 40, p. 865, 1952.

29. Friedman, B. and Williams, W., "Excitation of Surface Waves", Proc. IEE. Vol. , pp. 252-258, Jan. 1958.

30. Angulo, C.M. and Chang, W.S.C., "The Launching of Surface Waves by a Parallel Plate Waveguides", IRE. Trans., AP-7, pp. 359-368, Oct. 1959.

31. Chu, T.S. and Karp, S.N., "The Field of a Dipole Above an Infinite Corrugated Plane", Quart. Appl. Math., Vol. XXI, No. 4, pp. 257-268, Jan. 1964.

32. Wait, J.R., "Radiation from a Vertical Dipole Over a Stratified Ground, I", IRE. Trans. AP-1, pp. 9-11, July 1953, Part II, Trans. AP-2, pp. 144-146, Oct. 1954.

33. Wait, J.R., "Excitation of Surface Waves on Conducting, Stratified Dielectric Clad and Corrugated Surfaces", J. Res. N.B.S., Vol. 59, pp. 365-377, Dec. 1957.

34. Cullen, A.L., "The Excitation of Plane Surface Waves", Proc. IEE, Vol. 101, Part IV, pp. 225-234, 1954.

35. Fernando, W.M.G. and Barlow, H.E.M., "An Investigation of the Properties of Radial Cylindrical Surface Waves Launched Over Flat Reactive Surfaces", Proc. IEE, 100, B, pp. 307-318, May 1956.

36. Barlow, H.M. and Brown, J., Radio Surface Waves, Oxford Univ. Press, 1962.

37. Mueller and Tyrell, "Polyrod Antenna", Bell Sys. Tech. J., Vol. 26, p. 837, 1947.

38. Halliday, D. F. and Kiely, D. G., "Dielectric Rod Aerials", J. of IEE., Vol. 91, Part III, p. 105, 1944.

39. Watson, R.B. and Horton, C.W., "The Radiation Patterns of Dielectric Rod - Experiment and Theory", J. Appl. Phys., Vol. 19, p. 661, 1948.

40. Horton, C.W., Karal, Jr., F.C. and McKinney, C.M., "On the Radiation Patterns of Dielectric Rods of Circular Cross Section - the $TM_{0,1}$ Modes", J. Appl. Phys., Vol. 21, pp. 1279-1283.

41. Brown, J. and Spector, J.O., "The Radiation Properties of End-Fire Aerials", Proc. IEE., Vol. 104, Part III, pp. 27-34, 1957.

42. James, J.R., "Theoretical Investigation of Cylindrical Dielectric Rod Antennas", Proc. IEE, Vol. 114, No. 3, pp. 309-319, 1967.

43. Andersen, J.B., "Radiation from Surface-Wave Antennas", Elect. Letters, Vol. 3, pp. 251-252, 1967.

44. Hersch, W., "The Surface-Wave Aerial", Proc. IEE, Monograph No. 363E, pp. 202-212, Feb. 1960.

45. Kay, A.F., "Scattering of a Surface Wave by a Discontinuity in Reactance", IRE. Trans., AP-7, pp. 22-31, 1959.

46. Kane, Julius, "The Mathematical Theory of a Class of Surface Wave Antennas", Quart. Appl. Math., Vol. 21, pp. 199-214, 1963.

47. Andersen, J.B., "An Analysis of Surface Wave Antenna", in J. Brown (ed.) Electromagnetic Wave Theory, Peramon Press, N.Y., 1967.

48. Felesen, L.B. and Marcuvitz, N., "Modal Analysis and Synthesis of Electromagnetic Fields", Poly. Tech. Inst. Rept. No., PIBMRI-1056-62, Sept. 1962.

49. Karp, S.N. and Karal, Jr., F.C., "Vertex Excited Surface Waves on Both Faces of a Right-Angled Wedge", Comm. Pure & Appl. Math, Vol. XII, pp. 435-455, 1959.

50. Booker, H.G. and Clemmow, P.C., "The Concept of Angular Spectrum of Plane Waves, and Its Relation to That of Polar Diagram and Aperture Distribution", Proc. IEE, Vol. 97, Part III, pp. 11-17, 1950.

51. Collin, R.C. and Zucker, F.J., Antenna Theory Part 2, McGraw-Hill Book Co., New York, 1969.

52. Felsen, L.B., "Radiation from a Tapered Surface Wave Antenna", IRE Trans., AP-8, pp. 577-586, Nov. 1960.

53. Chu, T.S. and Kouyoumjian, R.G., "On the Surface Wave Diffraction by a Wedge", IEE Trans. A.&P., AP-13, pp. 159-164.

54. Chu, T.S., Kouyoumjian, R.G., Karal, F.C. and Karp, S.N., "The Diffraction of Surface Waves by a Terminated Structure in the Form of a Right-Angled Bend", IEE Trans. A.&P., AP-10, pp. 679-686, Nov. 1962.

55. Angulo, C.M., "Diffraction of Surface Waves by a Semi-Infinite Dielectric Slab", IRE. Trans. A.&P., AP-5, pp. 100-109, Jan. 1957.

56. Ehrlich, M.J. and Newkirk, L.L., "Corrugated Surface Antennas", IRE Nat. Conv. Rec. Pt. 2, pp. 18-23, 1953.

57. Elliot, R.S., "On the Theory of Corrugated Plane Surface", IRE Trans. A.&P., AP-2, pp. 71-81, Apr. 1954.

58. Senisper, R., "Electromagnetic Wave Propagation on Helical Structures", Proc. IRE, Vol. 45, pp. 149-161.

59. Pierce, J.R., "Circuits for Travelling Wave Tubes", Proc. IRE., Vol. 37, pp. 510-515, 1949.

60. Collin, R.E., Field Theory of Guided Waves, McGraw-Hill Book Company, Inc., New York, 1960.

61. Reynolds, D.K. and Lucke, W.S., "Corrugated End-Fire Antennas", Proc. Nat. Elec. Conf., Vol. 6, pp. 16-28, 1951.

62. Zucker, F.J., "A Surface Antenna Paradox", paper presented at URSI Fall Meeting, Penn. State Univ., 1958.

63. James J.R., "Radiation from Surface-Wave Antennas", Elect. Letters, Vol. 3, No. 7, p. 344, July 1967.

64. Dyson, J.D., "The Measurement of Phase at UHF and Microwave Frequencies", IEE Trans., MTT-14, No. 9, pp. 410-423, Sept. 1966.

65. Whiteside, H., "Electromagnetic Field Probes", Craft Lab. Tech. Rept., No. 377, Harvard University, Oct. 1962.

66. Justice, R. and Rumsey, V.H., "Measurement of Electric Field Distributions", IRE Trans. AP- , pp. 177-179, Oct. 1955.

67. Rumsey, V.H., "Reactive Concept in Electromagnetic Theory", Phys. Rev., Vol. 94, p. 2, Sept. 1954.

68. Magulus, P.P. and Matthews, P.A., "Current-distribution Measurements on Thin Conducting Sheets", Proc. IEE., Vol. 112, No. 4, pp. 655-660, April 1965.

69. Bacon, J., "An X Band Phase Plotter", Proc. NEC, Vol. X, pp. 256-263, Oct. 1954.

70. Gent, A.W. and Wallis, P.J., "Impedance Matching by Tappered Transmission Lines", Proc. IEE., Vol. 93, Part III A, pp. 559-563, 1947.

71. Noble, B., Methods Based on the Wiener-Hopf Technique, MacMillan, 1958.

72. Emerson, W.H., and Sefton, Jr., H.B., "An Improved Design for Indoor Ranges", IRE Proc., Vol. 53, pp. 1079-1081, Aug. 1965.

73. Jordan, E.C. and Balmain, K.G., Electromagnetic Waves and Rad Radiating System, Prentice-Hall Inc., 2nd Ed., p. 629, 1968.

74. King, H.E., Shimaabukuro, F.I., and Wong, J.L., "Characteristics of a Tapered Anechoic Chamber", IEE Trans., AP- , pp. 488-490, May 1967.

75. Hiatt, R.E., Knott, E.F. and Senior, T.B.A., "A Study of UHF Absorbers and Anechoic Rooms", University of Michigan Rad. Lab. Rept. No. 5391-1-F.

76. Von Hippel, A., Dielectric Materials and Applications, John Wiley & Son, Inc., New York.

77. King, H.E., Shimabukuro, F.I., and Wong, J.L., "94 Gc Measurements of Microwave Absorbing Materials", Air Force Report No. SSD-TR-66-71, March 1966.

78. Clark, A.G., McMillan, E.B., Schmitt, H.J., and Webber, Jr., A.H., "Testing of Absorbers and Free Space Rooms", McMillan Industrial Corp. Rept. No. F.S. -4, 1961.

APPENDICES

APPENDIX A

AN EXAMPLE OF THE APERTURE INTEGRATION METHOD

APPENDIX A

AN EXAMPLE ON THE APERTURE INTEGRATION METHOD

The validity of the aperture integration method applied to a surface wave radiation will be briefly proved by considering a simple example. Consider an infinitely long reactive surface with unit width supporting a TM surface wave,

$$H_x = H_0 e^{-\alpha y - j\beta z}$$

$$E_y = \frac{-\beta}{\omega\varepsilon} H_x \qquad (A.1)$$

$$E_z = \frac{-j\alpha}{\omega\varepsilon} H_x$$

With the coordinates shown in Figure A.1,

$$\hat{n} = \hat{y}$$

$$(\hat{n} \times \vec{E}) \times \hat{r} = -E_z(\hat{\theta} \sin\phi + \hat{\phi} \cos\phi)$$

$$\hat{n} \times \vec{H} = H_x(-\hat{r} \cos\theta + \hat{\theta} \sin\theta)$$

$$\hat{r} \cdot \vec{r}' = x' \sin\theta \cos\phi + z' \cos\theta$$

The E component of the radiation field can be obtained as

$$E_\theta = -\frac{e^{-jkr}}{4\pi r} \frac{kH_0}{\omega\varepsilon} (\alpha \sin\phi + jk \sin\theta) \cdot \int_0^1 \int_{-\infty}^{\infty} e^{jkx' \sin\theta \cos\phi} \; e^{-jk(\frac{\beta}{k} - \cos\theta)z'} \, dx'dz' \qquad (A.2)$$

The E plane pattern function is then determined as

$$E_\theta(\phi=\frac{\pi}{2}) = \frac{kH_0}{\omega\varepsilon}(\alpha + jk\sin\theta)\int_{-\infty}^{\infty} e^{-jk(\frac{\beta}{k}-\cos\theta)z'}dz'$$

$$= \frac{kH_0}{\omega\varepsilon}(\alpha + jk\sin\theta)\,\delta(\frac{\beta}{k}-\cos\theta)$$

$$= 0 \qquad (A.3)$$

since $\frac{\beta}{k}$ is always greater than unity for the slow surface wave. This proves that a uniform surface wave on an infinite plane cannot radiate.

Consider next a semi-infinite reactive surface supporting a TM surface wave defined as (A.1) and terminated at z=0 without reflection at this end. First, if the aperture integration method is applied to the semi-infinite guiding surface, the E plane radiation pattern function $E_{\theta_1}(\phi=\frac{\pi}{2})$ can be expressed as

$$E_{\theta_1}(\phi=\frac{\pi}{2}) = \frac{kH_0}{\omega\varepsilon}(\alpha + jk\sin\theta)\int_{-\infty}^{0} e^{-jk(\frac{\beta}{k}-\cos\theta)z'}dz'$$

$$= \frac{kH_0}{\omega\varepsilon}\,\frac{j(\alpha + jk\sin\theta)}{\beta - k\cos} \qquad (A.4)$$

where k is assumed slightly complex in carrying out the lower limit integration. If there is no reflection of the surface wave at the end, the fields on the terminal plane, z = 0 plane, may be expressed as

$$H_x = H_0 e^{-\alpha y}$$

$$E_y = \frac{-\beta}{\omega\varepsilon} H_0 e^{-\alpha y} \qquad (A.5)$$

$$E_z = \frac{-j\alpha}{\omega\varepsilon} H_0 e^{-\alpha y}$$

With the coordinate shown in Figure A.1c,

$$\hat{n} = \hat{z}$$

$$(\hat{n} \times \vec{E}) \times \hat{r} = (\hat{\theta} \sin \phi - \hat{\phi} \cos\theta \cos \phi)\, E_y \tag{A.6}$$

$$\hat{n} \times \vec{H} = (\hat{r} \sin \theta \sin \phi + \hat{\theta} \cos \theta \sin \phi + \hat{\phi} \cos \phi)\, H_x$$

the far-field expression for E_θ component may be obtained by integrating the above fields over the terminal plane as

$$E_\theta = -\frac{e^{-jkr}}{4\pi r} \frac{kH_0}{\omega\epsilon} \, j(\beta \sin \phi + k \cos \theta \sin \phi) \cdot \int_{S'} e^{-(\alpha - jk \sin \theta \sin \phi)y'} e^{jkx' \sin \theta \cos \phi} \, dx'dy' \tag{A.7}$$

The E plane pattern function $E_{\theta_2}(\phi = \frac{\pi}{2})$ for the unit width of the aperture is given by

$$E_{\theta_2}(\phi = \tfrac{\pi}{2}) = (\frac{kH_0}{\omega\epsilon}) \, j(\beta + k \cos \theta) \int_0^\infty e^{-(\alpha - jk \sin \theta)y'} \, dy'$$

$$= \frac{k\epsilon}{\omega\epsilon} \frac{j(\beta + k \cos \theta)(\alpha + jk \sin \theta)}{\alpha^2 + k^2 \sin^2 \theta} \tag{A.8}$$

In (A.8) the wave number must satisfy the relation of $\alpha^2 = \beta^2 - k^2$. With this relation, (A.8) can be rewritten as

$$E_{\theta_2}(\phi = \tfrac{\pi}{2}) = (\frac{kH_0}{\omega\epsilon}) \frac{j(\alpha + jk \sin \theta)}{\beta - k \cos \theta} \tag{A.9}$$

Note that (A.4) and (A.9) are identical pattern functions. This verifies that as long as the aperture integration is carried out properly, a correct result is obtained irrespective of how the aperture is chosen.

This also proves the validity of the aperture integration method by Kirchhoff's theory to the surface wave structures.

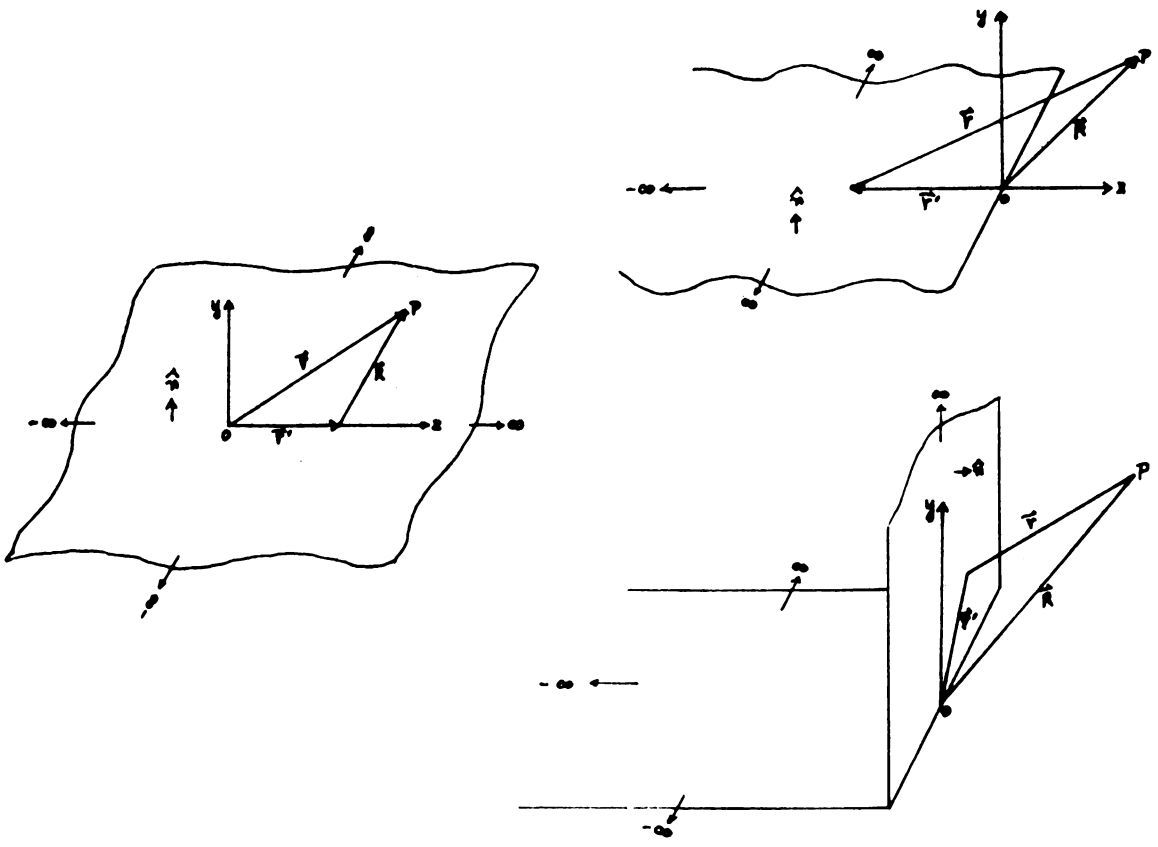

Figure A.1 Coordinates for Surface Wave Structure

APPENDIX B

A TAPERED ANECHOIC CHAMBER

APPENDIX B

A TAPERED ANECHOIC CHAMBER

For the design of a tapered anechoic chamber, a simple analysis was carried out based on the ground reflection approach (72). The surface of the chamber walls covered with the microwave absorbers was assumed to be electrically smooth in keeping with the Rayleigh creterion, so that it represents a finitely conducting mirror for the electromagnetic wave. A measure of roughness of a surface is given by the Rayleigh creterion (73) as

$$R = \frac{4\pi\sigma \sin\phi}{\lambda_0} \tag{B.1}$$

where R = a measure of roughness

σ = a standard deviation of the surface irregularities relative to the mean surface height.

ϕ = angle of incidence measured from the grazing angle

When $R < 0.1$, there is a well defined specular reflection, and the surface is considered to be electrically smooth. For $R > 10$, the surface is rough and there is no well defined specular reflection.

In the tapered chamber, it is not possible to eliminate all the reflected wave from the walls, even though the reflectivity of the walls covered with the microwave absorbers is very low. The direct path wave and the reflected wave from the walls are adjusted to add in phase at

the test area by adjusting the taper angle and the range distance, so that they create a slowly varying spatial interference pattern in the test area. However, there are two important effects (74) to limit the ultimate performance as an ideal antenna test range; One is the deviation from the 1/R dependence on the field amplitude. This deviation depends on the positions of the transmitting antenna at the throat of the chamber. The other is an apparent decrease or increase of signal strength as compared to the free space transmission.

With the consideration of these field limitations and the space limitation, the dimensions of the chamber were chosen to be the apex cone angle of 36°, the test region of 12x12x12 feet and the tapered section of 15 feet long as shown in Figure B.1.a. The walls of the chamber were covered with the microwave absorbers (ECCOSORB HPY-9). The rear wall was shaped to slightly angled wedge to reduce the possible back scattering from the wall (75).

To calculate the amplitude distribution in the test zone, only the first bounce reflection is considered on the basis of ray tracing technique. The assumption of only one first bounce reflection may be justified by the face that the higher order bounce have more nearer normal incidence reflection and may be attenuated significantly. From the geometry of the chamber shown in Figure B.1.b for the effect from the side walls, the direct path length from the transmitting antenna S to a observation point P, R_d, the reflected total path length from the side wall, R_{r1}, and the distance from the source S to the center of the horizontal cut through the observation point P, R_{r2}, are given by

$$R_d = (R_0 + x^2)^{1/2}$$

$$R_{r_1} = \{R_d^2 + 4h_t^2 + 4h_t (R_0 \sin \alpha - x \cos \alpha)\}^{1/2} \qquad \text{(B.2)}$$

$$R_{r_2} = \{R_d^2 + 4h_t^2 + 4h_t (R_0 \sin \alpha - x \cos \alpha)\}^{1/2}$$

For the reflections from the ceiling wall and the floor surface, the reflected path lengths R_1 and R_2 are given by

$$R_1 = [R_0^2 + 4h_t^2 + 4R_0 h_t \sin \alpha]^{1/2} \qquad \text{(B.3)}$$

$$R_2 = [R_d^2 + 4h_t^2 + 4R_0 h_t \sin \alpha]^{1/2}$$

Assuming that the field in the chamber is close to plane wave, the field strength at the point P in the horizontal plane may be expressed in terms of the direct path field amplitude E_d as

$$E_p = E_d[e^{-jkR_d} + \Gamma_1(\frac{R_d}{R_{r_1}} e^{-jkR_{r_1}} + \frac{R_d}{R_{r_2}} e^{-jkR_{r_2}}) + 2\Gamma_2 \frac{R_d}{R_2} e^{-jkR_2}] \qquad \text{(B.4)}$$

where Γ_1 is the reflection coefficient from the side walls of the chamber, and Γ_2 the reflection coefficient from the upper and bottom walls. The reflection coefficients from each side wall are assumed to be equal since the angles of incidence on the both walls are almost similar for both reflections. The reflection coefficients Γ_1 and Γ_2 are complex quantities, and either of the reflection coefficients corresponds to the horizontal or vertical polarization depending on the polarization of the transmitted

wave. The reflection coefficients for oblique incidence of both polarizations are given as follows:

For horizontal polarization

$$\Gamma_h = \frac{\sin\phi - \sqrt{(\varepsilon_r' - j\varepsilon_r'') - \cos^2\phi}}{\sin\phi + \sqrt{(\varepsilon_r' - j\varepsilon_r'') - \cos^2\phi}} \qquad (B.5)$$

For vertical polarization

$$\Gamma_v = \frac{(\varepsilon_r' - j\varepsilon_r'')\sin\phi - \sqrt{(\varepsilon_1' - j\varepsilon_r'') - \cos^2\varepsilon}}{(\varepsilon_r' - j\varepsilon_r'')\sin\phi + (\varepsilon_1' - j\varepsilon_r'') - \cos^2\phi} \qquad (B.6)$$

where $\varepsilon_r' = \frac{\varepsilon}{\varepsilon_0}$ $\varepsilon_r'' = \frac{\sigma}{\omega\varepsilon}$.

The value of the true dielectric constant of the microwave absorber used in the chamber is not available in the literature. From the information on the absorber material properties and the measured values (76-78), the approximate reflection coefficients Γ_1 and Γ_2 were calculated with $\varepsilon_r' = 1.1$ and $\varepsilon_1'' = 0.01$ to 2.0, and they are plotted in Figure B.2 and Figure B.3. Figure B.2 shows that the pseudo Brewster angle is about 45° with the half cone angle of 18°. With this tapered angle, the angle of incidence measured from the plane of absorber wall is about 22°. With this angle and the representative dielectric constant for the absorber $\varepsilon_r = 1.1 - j\ 0.12$, the relative field distribution with respect to the direct path wave strength was calculated in the test area of chamber. Figure B.4 shows the predicted relative field distributions in horizontal cut as a function of the distance from the chamber axis. Figure B.5 shows the field variation along the chamber axis which is an interference pattern as predicted. Reviewing these field variations,

±0.25 db along the excursion of ±4 feet from the center of the test area and ±0.05 db variation along the chamber axis, the designed chamber with the taper angle of 36° and the test range of 24 feet may be adequate for the evaluation of antennas in the operating frequency above 1000 Mhz.

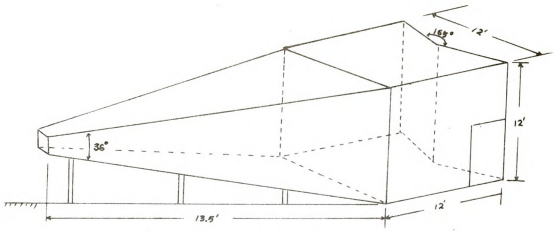

(a) 3-dimensional view

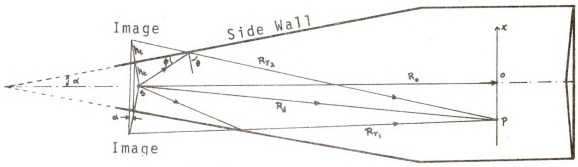

(b) Top view

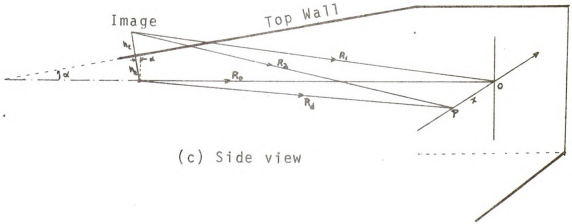

(c) Side view

Figure B.1 Tapered Anechoic Chamber

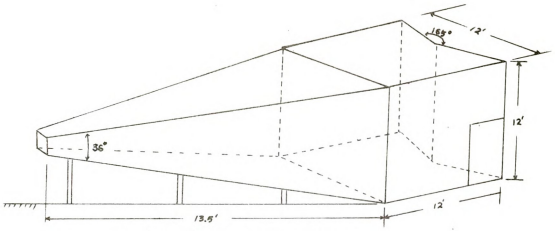

(a) 3-dimensional view

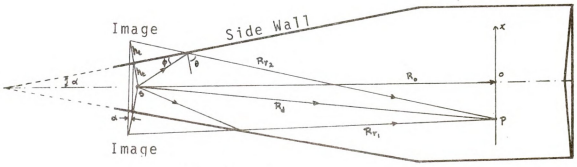

(b) Top view

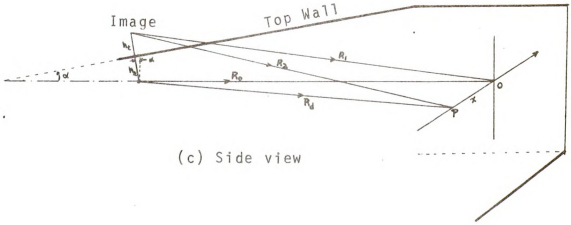

(c) Side view

Figure B.1 Tapered Anechoic Chamber

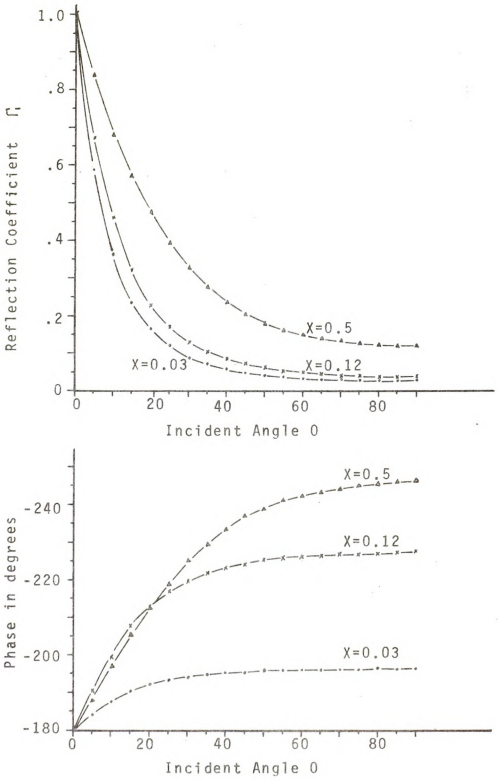

Figure B.2 Complex Reflection Coefficient for Horizontal Polarization with $\varepsilon = 1.1 - jx$.

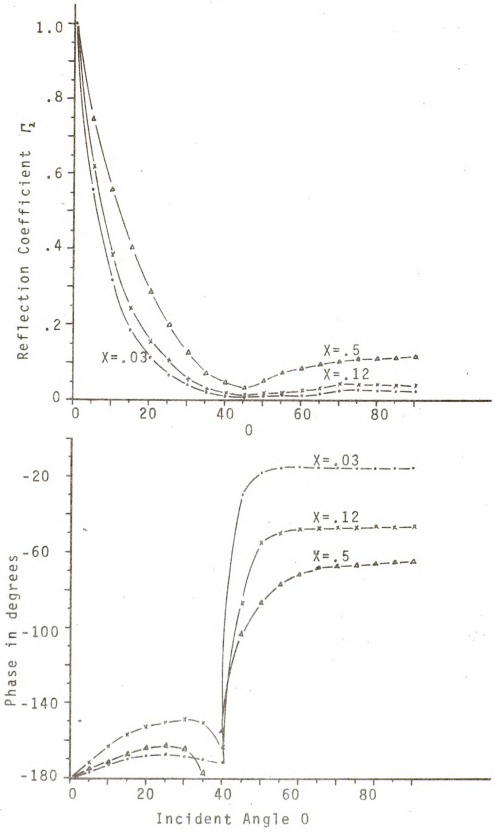

Figure B.3 Complex Reflection Coefficient for Vertical Polarization with $\varepsilon = 1.1 - jx$.

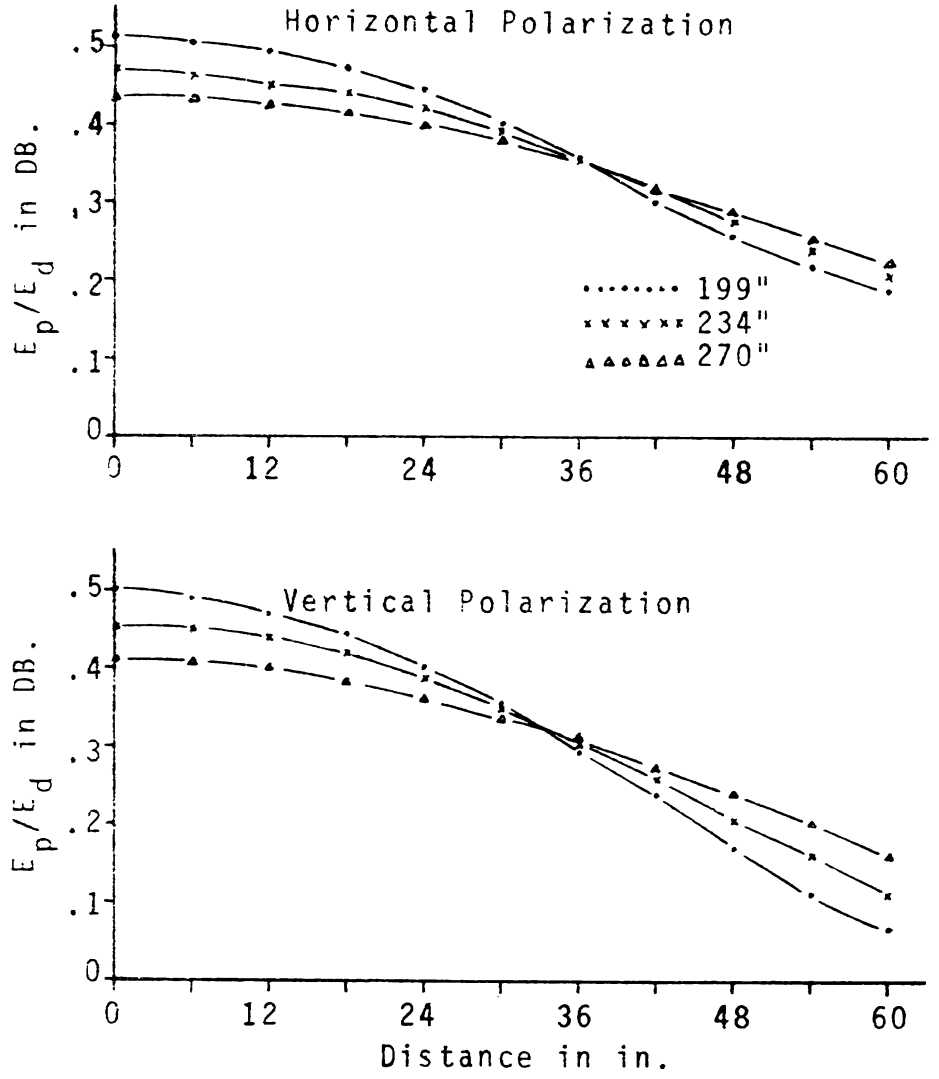

Figure B.4 Relative Electric Field Variation in Test Zone for 1 Ghz. (Horizontal Cut)

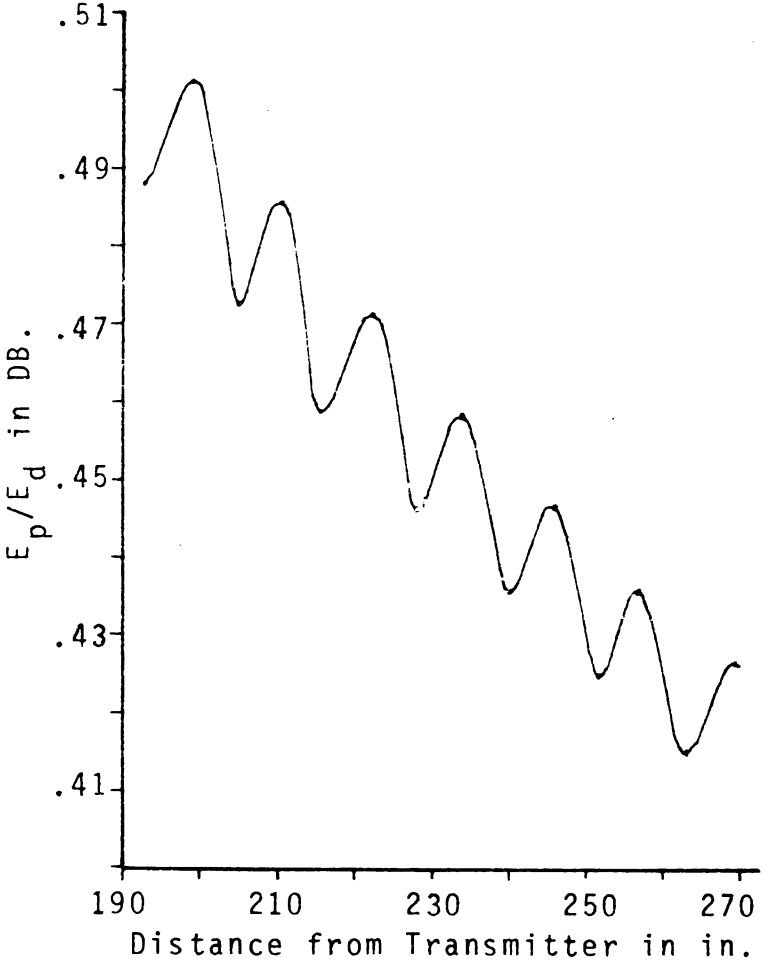

Figure B.5 Relative Electric Field Variation Along Chamber Axis in Test Zone for 1 Ghz.